General Disclaimer

One or more of the Following Statements may affect this Document

- This document has been reproduced from the best copy furnished by the organizational source. It is being released in the interest of making available as much information as possible.

- This document may contain data, which exceeds the sheet parameters. It was furnished in this condition by the organizational source and is the best copy available.

- This document may contain tone-on-tone or color graphs, charts and/or pictures, which have been reproduced in black and white.

- This document is paginated as submitted by the original source.

- Portions of this document are not fully legible due to the historical nature of some of the material. However, it is the best reproduction available from the original submission.

NASA CONTRACTOR REPORT 158917

(NASA-CR-158917) IMPROVED DETECTIVITY OF PYROELECTRIC DETECTORS Final Report (Honeywell Electro-Optics Center) 178 p HC A09/MF A01 CSCL 14B G3/35

N78-33406

Unclas 33792

IMPROVED DETECTIVITY OF PYROELECTRIC DETECTORS

D.E. Marshall, J.C. Gelpey, J.W. Marciniec, A.M. Chiang and R.B. Maciolek

HONEYWELL
Electro-Optics Center
Lexington, MA 02173

CONTRACT NAS1-14372

September 1978

NASA
National Aeronautics and Space Administration

Langley Research Center
Hampton, Virginia 23665

IMPROVED DETECTIVITY OF PYROELECTRIC DETECTORS

Final Technical Report

by

D.E. Marshall, J.C. Gelpey, J.W. Marciniec and A.M. Chiang
Honeywell Electro-Optics Center
Lexington, Massachusetts 02173

and

R.B. Maciolek
Honeywell Corporate Material Sciences Center
Bloomington, Minnesota 55420

NASA Contract NAS1-14372

Prepared for

NATIONAL AERONAUTICS AND SPACE ADMINISTRATION
Langley Research Center
Electronic Devices Research Branch
Hampton, Virginia 23365

June 1978

HONEYWELL
Electro-Optics Center
2 Forbes Road
Lexington, Massachusetts 02173

7808-11

ABSTRACT

High detectivity single-element SBN pyroelectric detectors have been fabricated. The theory and technology developments related to improved detector performance have been identified and formulated. Improved methods of material characterization, thinning, mounting, blackening and amplifier matching are discussed. Detectors with detectivities of 1.3×10^9 cm$\sqrt{\text{Hz}}$/watt at 1 Hz are reported. Factors limiting performance and recommendations for future work are discussed.

FOREWORD AND ACKNOWLEDGEMENTS

This final report summarizes work performed under NASA Contract NAS1-14372, "Improved Detectivity of Pyroelectric Detectors." This work was performed at the Honeywell Electro-Optics Center (EOC) in Lexington, Massachusetts and at the Honeywell Corporate Material Sciences Center (CMSC) in Bloomington, Minnesota. The period of performance was April, 1976 through December, 1977.

The NASA Technical Representatives for this program were James B. Robertson and Roger K. Crouch. The authors express appreciation to them, and to Roger Breckenridge, for their support and encouragement during this program.

The authors acknowledge the technical contributions which several of their colleagues at Honeywell provided during the course of this program, particularly S.T. Liu, N.R. Butler, R.J. Martineau and R.C. Leung. Detectors were fabricated by B.W. Denley and D. Smith, and measurements were performed by R.S. Healy and J.R. Monahan.

TABLE OF CONTENTS

LIST OF ILLUSTRATIONS

LIST OF ILLUSTRATIONS

LIST OF ILLUSTRATIONS

LIST OF ILLUSTRATIONS

LIST OF TABLES

SECTION 1
INTRODUCTION

Current state-of-the-art earth resources and thermal imaging systems use cryogenically cooled detectors and have mechanically scanned optical systems to obtain a full field of coverage. Lower power dissipation and longer life systems could be obtained by using large electronically scanned arrays of room temperature detectors to do the same infrared detection.

The optimum approach to solve this problem is the development of detectors and silicon CCD separately, maximizing the performance of each, and then integrating them with minimal degradation. Silicon CCDs are in development at Honeywell for many staring and scanning focal plane applications. They are being made with 1 to 2-mil unit cells, bump and thin film detector interconnect mechanisms, and being optimized for operation at room temperature and various cryogenic temperatures.

For room temperature operation, pyroelectric detectors are the logical selection. They are faster than the conventional bolometers and other types of detectors such as Golay cells. Also, they are ideally suited for coupling to a CCD without an amplifier because they generate an electronic charge in proportion to their differential temperature change.

A program of optimization was conducted to maximize the performance of SBN detectors. As a figure of merit goal, a detectivity of 5×10^9 cm $Hz^{1/2}/W$ was chosen. To achieve this goal, tasks in crystal growth, wafer selection and preparation, and detector fabrication (including thinning, blackening, and electroding), mounting for low thermal conduction, and optimum selection of a JFET readout preamp were conducted.

Analysis and testing were conducted to maximize the pyroelectric coefficient, minimize the tan δ and detector thickness, and minimize thermal mounting conductivity.

The results of the program show thermal frequency corners of the order of 1 Hz or less, black coating efficiency of $\geq$ 90%, a tan δ improvement of a factor of 15 and a D* of 1.3×10^9 cm $Hz^{1/2}/W$.

It is concluded that a good optimization of the various disciplines has been conducted, and that, based on this learning, array technology and CCD coupling should be investigated.

SECTION 2

THEORY OF PYROELECTRIC DETECTORS

In quantum (photon) detectors incident radiant energy is converted directly to mobile charge carriers, whereas thermal detectors function by the conversion of incident radiation to heat. The associated temperature change causes a change in some electrically measurable property of the detector. There are familiar examples of thermal detectors including the Golay cell and resistance and capacitance bolometers in which gas pressure resistance and capacitance are measured.

In pyroelectric detectors the electrical property sensed is the change in the spontaneous polarization of a dielectric material. The pyroelectric effect itself is very fast. However, pyroelectric detector response is subjected to the same laws of heat flow as are other thermal detectors. Due to the magnitude of the pyroelectric effect, higher detectivities at higher frequencies have been obtained with pyroelectrics than with any other thermal detector.

Since a temperature change is involved in the detection process, heat flow must be considered in an analysis of the detection process. High performance requires maximizing the temperature change for a given change in input radiance. Thus, thermal isolation and heat capacity are important aspects of practical pyroelectric detector design. In addition, temperature noise, negligible in quantum detectors, may be a significant noise process in pyroelectric detectors.

Thermal detectors offer the advantages of room temperature operation and wide spectral response. In the past decade, thermal imaging has been demonstrated with the pyroelectric vidicon.[1] Recent work, based on the development of new pyroelectric materials, is focused on making small, high performance discrete detectors, and an emerging technology area is the development of solid-state pyroelectric thermal imagers.

2.1 QUALITATIVE DESCRIPTION

The basic detector element, shown in Figure 1, is deceptively simple in structure, consisting of a capacitor in which the dielectric material has a pyroelectric response. As indicated in Figure 2, incident radiation is absorbed by the front surface and the resulting heat diffuses through a thin film electrode into the dielectric causing a temperature change. The front surface of the detector is "blackened" to provide a high emissivity η in the spectral region of interest. There are several electroplated coatings capable of providing a high emissivity from the visible out to 15 micrometers and beyond. These layers are generally rough, porous films on a micrometer scale with the surface characteristics controlled by the plating rates.

Since the front surface has a high emissivity, the detector radiates energy back to the environment. Radiative heat loss through the back surface is minimized by using a "shiny" electrode with low emissivity η_b. In addition to radiative heat exchange, there is a conducted heat loss between the detector and its environment through a number of paths.

The change in temperature of the pyroelectric material causes a change in its spontaneous polarization. This produces a change in the dielectric surface charge which can be sensed as an output current. The intrinsic loss mechanism in pyroelectrics is the capacitor dissipation factor D or dielectric loss tangent (tan δ). Bulk resistivity losses are negligibly small; however, output amplifier noise can exceed detector noise in many applications.

All pyroelectric materials are also piezoelectric, thus care must be taken in the mounting of the detector to avoid the microphonic noise.

2.2 THEORY OF OPERATION

Pyroelectric detection can be described by reference to the simplified lumped model in Figure 3. The temperature absorbed power P_a is equal to the incident power P_i times the front surface emissivity η_f. The temperature change

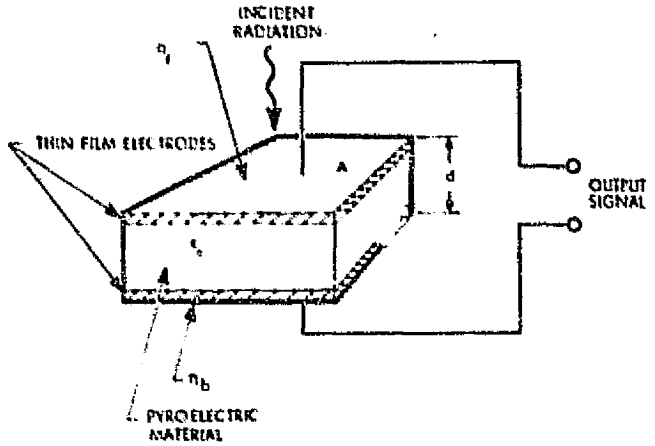

Figure 1. BASIC PYROELECTRIC DETECTOR ELEMENT

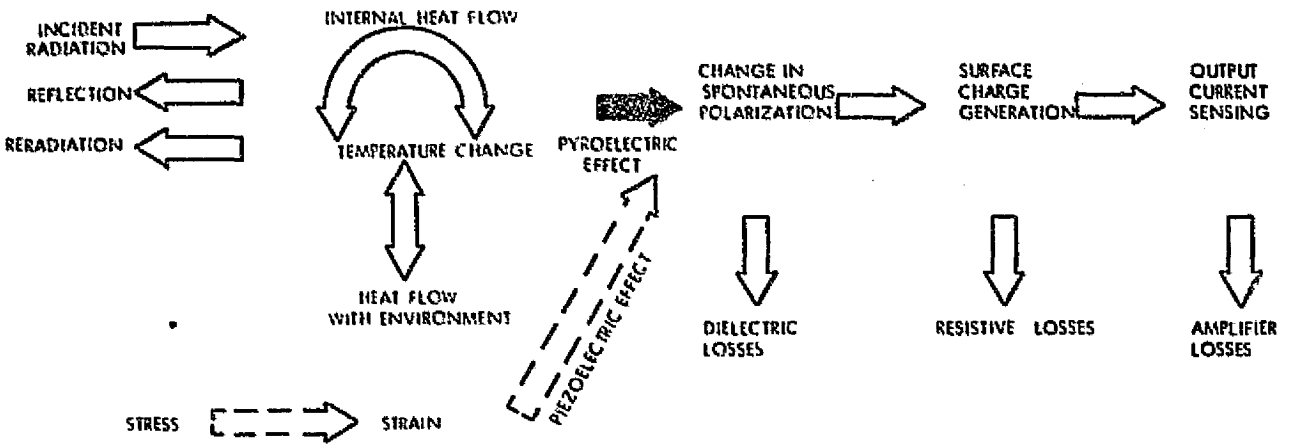

Figure 2 ENERGY CONVERSION AND FLOW IN PYROELECTRIC DETECTION

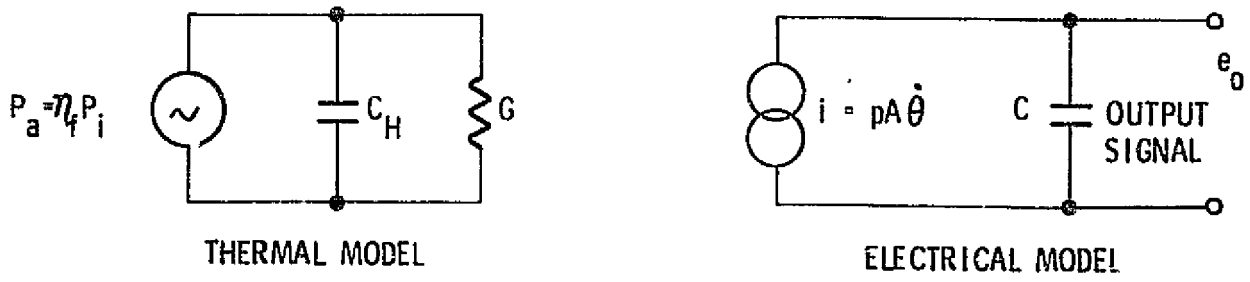

Figure 3 LUMPED PYROELECTRIC DETECTOR MODEL

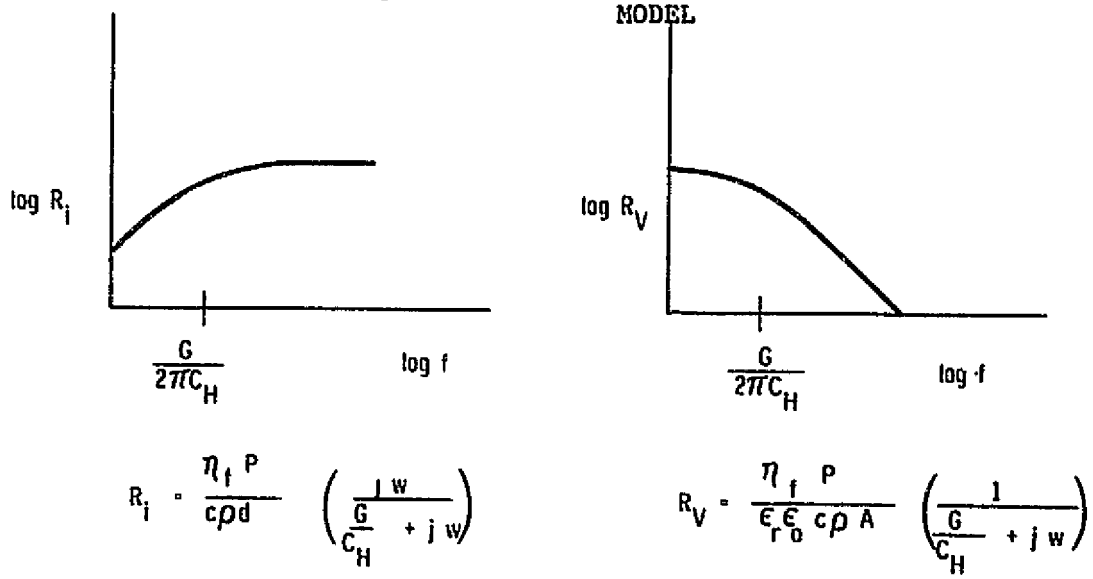

Figure 4 CURRENT AND VOLTAGE RESPONSIVITIES

θ of the detector is related to the absorbed power by the heat capacity of the detector C_H, and thermal losses between the detector and its surroundings are represented by a thermal conductance G. Thus, the temperature response for a sinusoidally varying input power of radian frequency ω is:

$$\theta = \frac{\eta_f P_i}{C_H (G/C_H + j\omega)} \qquad (1)$$

High thermal responsivity is obtained by making the detector heat capacity as small as possible and at low frequencies by making the thermal time constant (C_H/G) as high as possible. The heat capacity is equal to: $C_H = c\rho\, Ad$ where c is the material specific heat, ρ is the material density, and the detector area A times its thickness d is it volume. The $c\rho$ product is called the material volume specific heat.

The magnitude of the pyroelectric effect is described by the pyroelectric coefficient p of the detector and is equal to the change in the electric dipole moment per unit temperature and is also equal to the change in surface charge density per unit temperature. As shown in Figure 3, pyroelectric response can be described as a current generator with a magnitude equal to the pyroelectric coefficient p times the detector area A times the rate of changes in temperature $\dot{\theta}$. The detector impedance is dominated by its capacitance C and thus for a sinusoidally varying temperature change the output voltage is:

$$e_o = j\,\frac{pA\theta}{C} \;;\; \dot{\theta} = j\,\omega\,\theta \qquad (2)$$

Based on this model, idealized current and voltage responsivities R_i and R_v are as shown in Figure 4.

2.3 THERMAL EFFECTS

Thermal losses are illustrated in Figure 5. Conduction and convection losses through the air can be eliminated by operating the detector in a vacuum. It has also been observed that microphonics noise caused by airborne excitation of the detector is diminished when the detector is operated in a vacuum. Radiated loss is described by the blackbody equation:

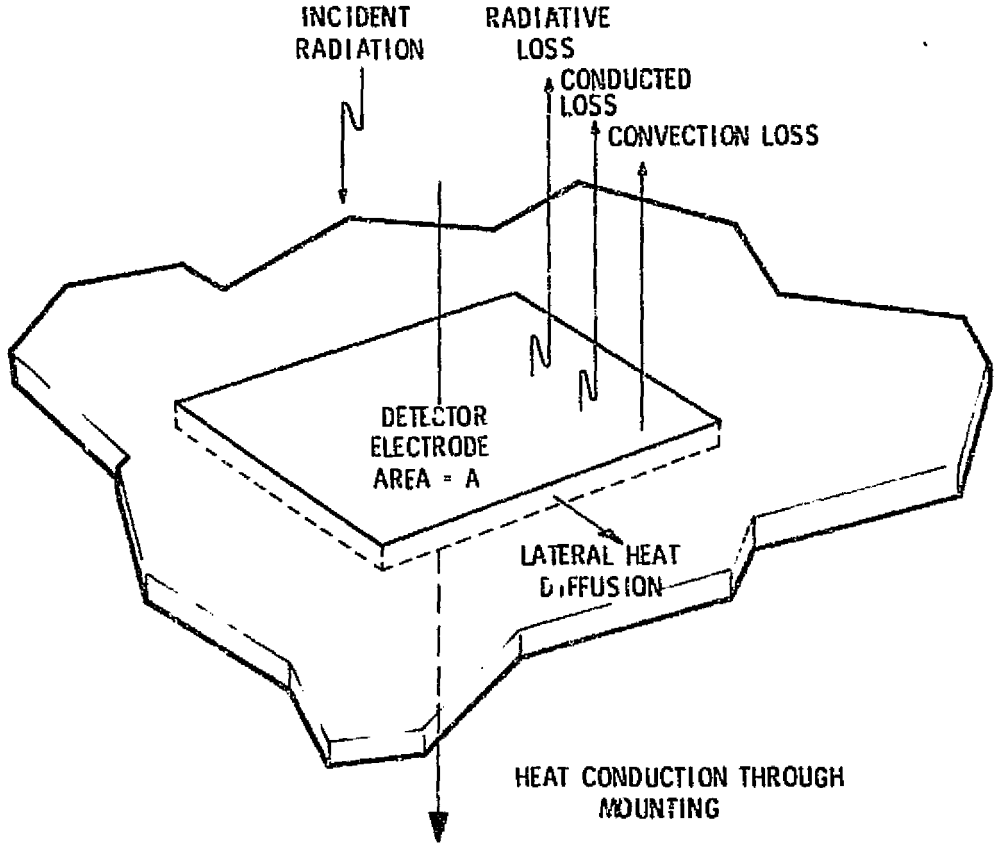

Figure 5 HEAT LOSSES

$$P_r = \eta\sigma T^4 \tag{3}$$

where P_r is the radiated power per unit area, η is the surface emissivity, and σ is the Stefan-Boltzmann constant. For small temperature changes, radiative loss can be described as thermal conductivity g_r by taking the derivative of the above expression with respect to temperature:

$$g_r = 4\eta\sigma T^3 \tag{4}$$

Heat flow in a body is described by the differential equation:

$$\dot{\theta} = D_t \nabla^2 \theta \tag{5}$$

where D_t is the thermal diffusivity of the body and is equal to its thermal conductivity g divided by its volume specific heat:

$$D_t = \frac{g}{c\rho} \tag{6}$$

One-dimensional solutions to the heat flow equation can be found in the literature for a variety of detector configurations[2,3]. A thermal diffusion depth L can also be defined:

$$L = \sqrt{\frac{2D_t}{\omega}} \tag{7}$$

L is the distance along a semi-infinite bar, thermally modulated sinusoidally at the end, at which the amplitude of the temperature change has decreased by 1/e. To obtain a high pyroelectric response, the detector thickness (electrodes and dielectric body) should be much less than the diffusion depth at the highest frequency of interest. If this is the case, the temperature change at the front surface will penetrate the electrode and cause an isothermal change in the detector temperature. Conversely the path length through mounting structure should be much larger than a diffusion depth to minimize heat loss. The thermal diffusivity of typical pyroelectric materials is on the order of 10^{-3} cm^2/s. Thus at 100 Hz, the diffusion depth is about 20 micrometers.

In the pyroelectric vidicon as well as in undelineated detector arrays, lateral heat diffusion through the pyroelectric material is an important performance factor since it causes crosstalk and a loss in resolution. If a discrete detector is mounted directly underneath its active area this path usually dominates heat losses. A preferred mounting approach is to cantilever the detector by mounting it outside the active area so that heat must flow laterally before it can flow through the mount.

2.4 NOISE

Heat flow has a noise associated with it. Temperature noise is similar in form to resistor Johnson-Nyquist noise and can be expressed as:

$$P_n = (4\ KT^2\ g\ A_c)^{1/2}\ \text{watts}/\sqrt{\text{Hz}} \tag{8}$$

where K is Boltzmann's constant and A_c is cross sectional area of the conductor. From the expression for radiative conductivity (Equation 4) the noise associated with radiation exchange is:

$$P_{n_r} = (16\ \eta\sigma\ KT^5\ A_r)^{1/2}\ \text{watts}/\sqrt{\text{Hz}} \tag{9}$$

The intrinsic noise mechanism in pyroelectrics is associated with dielectric losses, expressed by the ratio of the imaginary part to the real part of the dielectric constant, called the dissipation factor D or loss tangent. The ac parallel resistance of the dielectric is:

$$R = \frac{1}{\omega C \tan \delta} \tag{10}$$

which has a noise current in $i_n = (4\ KT/R)^{1/2}\ A/\sqrt{\text{Hz}}$.

2.5 DETECTIVITY

Two detectivities are used to describe pyroelectric detector performance. The first is detectivity limited by dielectric losses and from the current responsivity and the above noise expression is:

$$D^*_i = \frac{R_i \sqrt{A}}{i_n} = \frac{\eta_p}{c\rho\,(4\,KT\,\epsilon_r\epsilon_o\,d\,\tan\delta)^{1/2}} \left[\frac{\omega}{\omega^2 + \frac{G}{c\rho A_d}^2}\right]^{1/2} \qquad (11)$$

This equation contains a factor $p/c\rho\sqrt{\epsilon_r}$ containing well defined pyroelectric material properties and is used as a material figure-of-merit (M_1). Detectivity is inversely proportional to the square root of detector thickness d, providing an incentive to make the detectors as thin as possible. A $LiTaO_3$ detector thickness on the order of four micrometers has been reported using ion beam milling thinning techniques.

The second detectivity is the background limit, found by using the radiative heat transfer noise (Equation 9), as the significant noise source and is:

$$D^*_{BLIP} = \frac{\sqrt{A}}{P_{nr}} = \frac{\eta}{16\,\sigma\,KT^5}^{1/2} \qquad (12)$$

where it is assumed that the area contributing to radiative noise is equal to the active detector area. For $\eta = 1$, background limited detectivity is equal to 1.8×10^{10} cm $Hz^{1/2}/W$ at 300 K. This is sometimes considered to be a theoretical limit on thermal detector performance. However, it assumes a blackbody emissivity, and it should be possible to fabricate front electrode surface films with limited spectral responsivity and which are also isothermal. Such films would make D^*_{BLIP} for thermal detectors similar to the limit for photon detectors.

2.6 PREAMPLIFIER COUPLING

The signal amplifier is an important source of noise in pyroelectric detectors. The most common amplifier used is the JFET source follower shown in Figure 6a. The noise model in Figure 6b lumps all the noise sources associated with the detector into the current generator i_d. The other noise components are the load resistor noise i_R, gate current shot noise i_J, and JFET channel noise e_a. Figure 7 shows all the important noise sources in a typical JFET

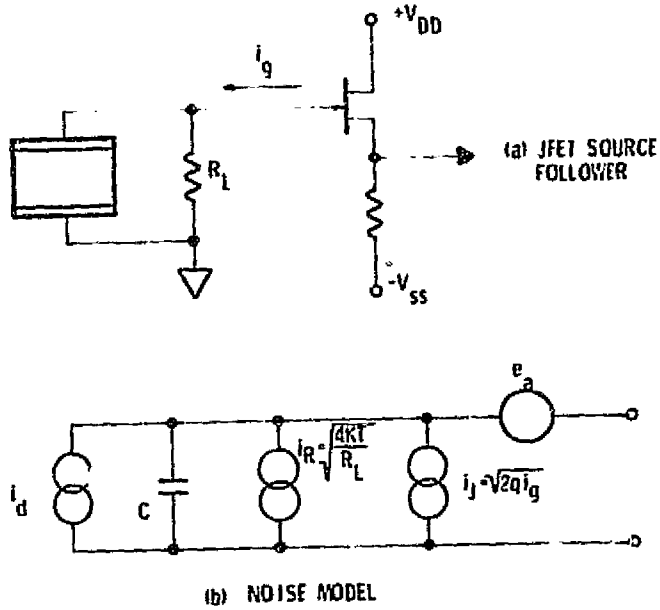

Figure 6 JFET COUPLING

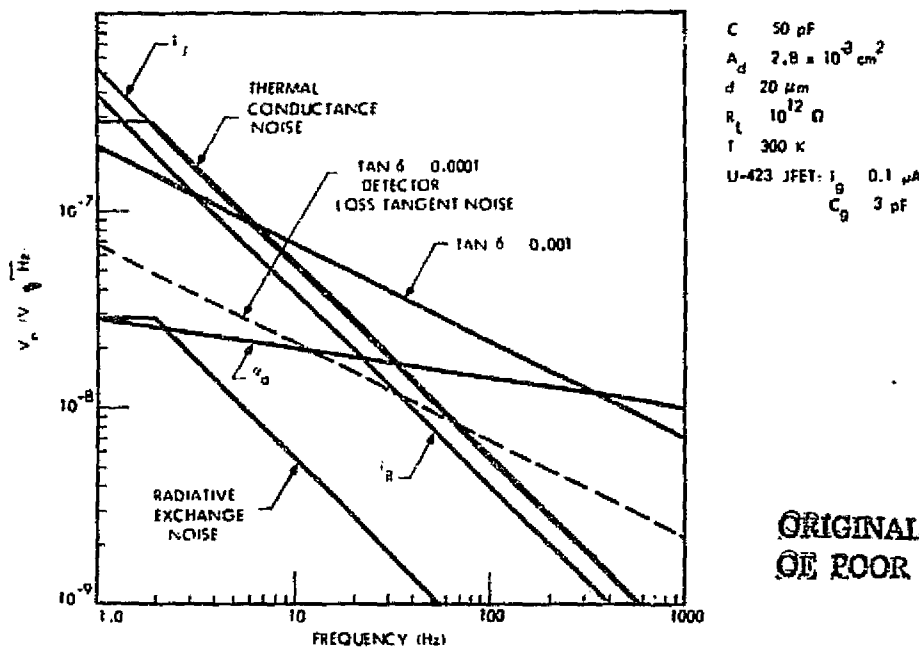

ORIGINAL PAGE IS
OF POOR QUALITY

Figure 7 NOISE SOURCES IN AN SBN PYROELECTRIC DETECTOR CIRCUIT

coupled strontium barium niobate (SBN) detector circuit as a function of frequency. Detector conducted temperature noise is calculated assuming a thermal time constant associated with the mounting structure of 2 Hz, and loss tangent noise is calculated for a loss tangent of 0.001 and 0.0001.

For a detector loss tangent of 0.001 the intrinsic detector noise dominates over a useful frequency range. As the loss tangent improves to 0.0001 other noise sources limit performance, principally the JFET current and voltage noise sources i_j and e_a. Conductive temperature noise, which also limits low frequency performance can be reduced by taking great care in thermally isolating the detector from its mounting structure.

SECTION 3

MATERIAL GROWTH AND CHARACTERIZATION

In order to achieve high detectivity in pyroelectric detectors it is important to select a pyroelectric material having optimum properties. The specific material properties shown in Equation 11 are pyroelectric coefficient (p), volume specific heat ($c\rho$), dielectric constant (ε) and dielectric loss factor ($\tan \delta$). The first three are combined as they appear in Equation 11 and called the "Figure of Merit" M_1. This factor and representative values of $\tan \delta$ for several materials is listed in Table 1. This shows SBN to be the material having the best potential for achieving high $\tan \delta$ noise limited D*.

Additional factors in selection of a detector are its manufacturability, stability, and susceptibility to microphonics. SBN is nonhygroscopic which simplifies fabrication processing and reduces potential effects of moisture in storage and handling. It also has the lowest piezoelectric coupling coefficient, thus minimizing the secondary unwanted polarization and electromechanical effects. Finally, SBN has a Curie temperature of 120°C, which is low enough for relative ease of poling and high enough that depoling would not be a problem in detector storage and operation.

3.1 SBN CRYSTAL GROWTH

A total of 30 $Sr_{0.5}Ba_{0.5}Nb_2O_6$ ingots were grown using the Czochralski method at the Honeywell Corporate Materials Science Center (CMSC) for this program. They were all approximately 8 mm in diameter and ranged in length from 2-1/2 to 10 cm long. Many were experimental crystals used to evaluate and optimize the growth procedures. Some were used for seed material for other crystals. Much of this work was funded by Honeywell.

3.2 CRYSTAL CHARACTERIZATION

Ten of the 30 crystals were selected to be used for detector fabrication. Before shipment to EOC wafers were selected and evaluated for dislocation

Table 1 PYROELECTRIC DETECTOR MATERIALS AND THEIR FIGURE OF MERIT AT ROOM TEMPERATURE

Material	T_c	c $J/g_r\text{-}°C$	ρ g_r/cm^3	p $Coul/cm^2\text{-}°C$	E	$M=\frac{p}{c_p\sqrt{\epsilon}}$	SOA Device tan δ	SOA Bulk tan δ	k_{33}
SBN	120	0.445	5.26	6×10^{-8}	400	1.28×10^{-9}	0.003	10^{-4}	0.16
$LiTaO_3$	618	0.45	7.45	1.9×10^{-8}	45	8.45×10^{-10}	0.003	10^{-4}	0.184
PLZT 1.5/90/10 La/Zr/Ti	100	0.4	7.98	3.5×10^{-8}	305	6.28×10^{-10}	0.02	--	0.22
PVF_2	--	1.3	1.76	3×10^{-9}	11	3.95×10^{-10}	--	--	--

density by polishing and measurement of their etch pit density. The results of this study are shown in Table 2.

Table 2

SBN CRYSTAL CHARACTERISTICS

SBN Crystal Number	Total Dislocation Count (counts/cm^2)	Curie Temp (°C)
061176	16	125
063076	32	---
070176	1	---
072976	17	---
080376	14	129
080576	1	128
081976	4	---
082076	13	130
082476	10	131
082576	1	128

Further evaluation of several of the crystals was done at EOC prior to detector evaluation. This included measurement of the Curie temperature and spontaneous polarization.

Knowledge of the Curie temperature would aid in determining if there were compositional variations from ingot to ingot, as the Curie temperature varies with the stoichiometry of the crystal. This could then be related to such parameters as the dielectric constant and pyroelectric coefficient. Poling the material at a temperature above the Curie temperature would be helpful in completely polarizing the sample. The Curie temperature (transition temperature) can be found experimentally by measuring the material's capacitance (dielectric constant) with respect to temperature. Then the relation $\varepsilon = K/(T-Tc)$ can be used.If the reciprocal of the capacitance (dielectric constant) is plotted versus temperature, we have $T = Tc$ when $1/\varepsilon = 0$; i.e., the "x-intercept" gives the Curie temperature. Since the ferroelectric phase transition in SBN is second order, the transition temperature and Curie temperature are equal.

A jig was made to carry out the Curie temperature tests, and the results are shown in Table 2. Graphs showing the capacitance data from a typical Curie temperature experimental run, and indicating the determination of the Curie temperature from the reciprocal of the capacitance, are given in Figures 8 and 9. The Curie temperature data suggests changes in stoichiometry of only a few percent, and this is within the accuracy of the Curie temperature measurements.

One property of ferroelectric crystals is that they exhibit a spontaneous polarization (P_s) when no field is applied to the plates of a capacitor using the ferroelectric as its dielectric. The magnitude of this spontaneous polarization can be determined very easily by observing the ferroelectric hysteresis loop of the material. To do so is quite simple, using the circuit shown in Figure 10.

When a ferroelectric crystal is placed in this circuit, a hysteresis loop resembling that shown in Figure 11 will result.

In order to determine P_s, the following procedure is used. C_x and C_1 are in series, and typically $C_1 = 1000\ C_x$. This assumes that all the voltage applied is dropped across C_x. This voltage applied is represented on the oscilloscope by the voltage across R_1; typically $R_2 = 10\ R_1$. The voltage is supplied from a variac, giving 0–120 volts at 60 Hz. Since C_x and C_1 are in series the charge Q generated on the plates of C_x due to V_{app} ($Q = C_x V_{app}$) will also appear on the plates of C_1. Therefore, the voltage across C_1 will be given by $V_1 = Q/C_1$. This voltage is used to drive the vertical amplifier of the oscilloscope. Thus, by measuring V_1 from the oscilloscope, we can determine Q; $Q = C_1 V_1$. Since P_s is defined as the $(\text{charge/area}|_{V_{app}=0})$ we measure $V_1|_{V_{app}=0}$ to obtain Q_0. This gives $P_s = (C_1 V_1|_{V_{app}=0})/A_d$, where A_d is the area of the plates of the ferroelectric crystal. $C_1 = 0.2\ \mu F$ in these tests.

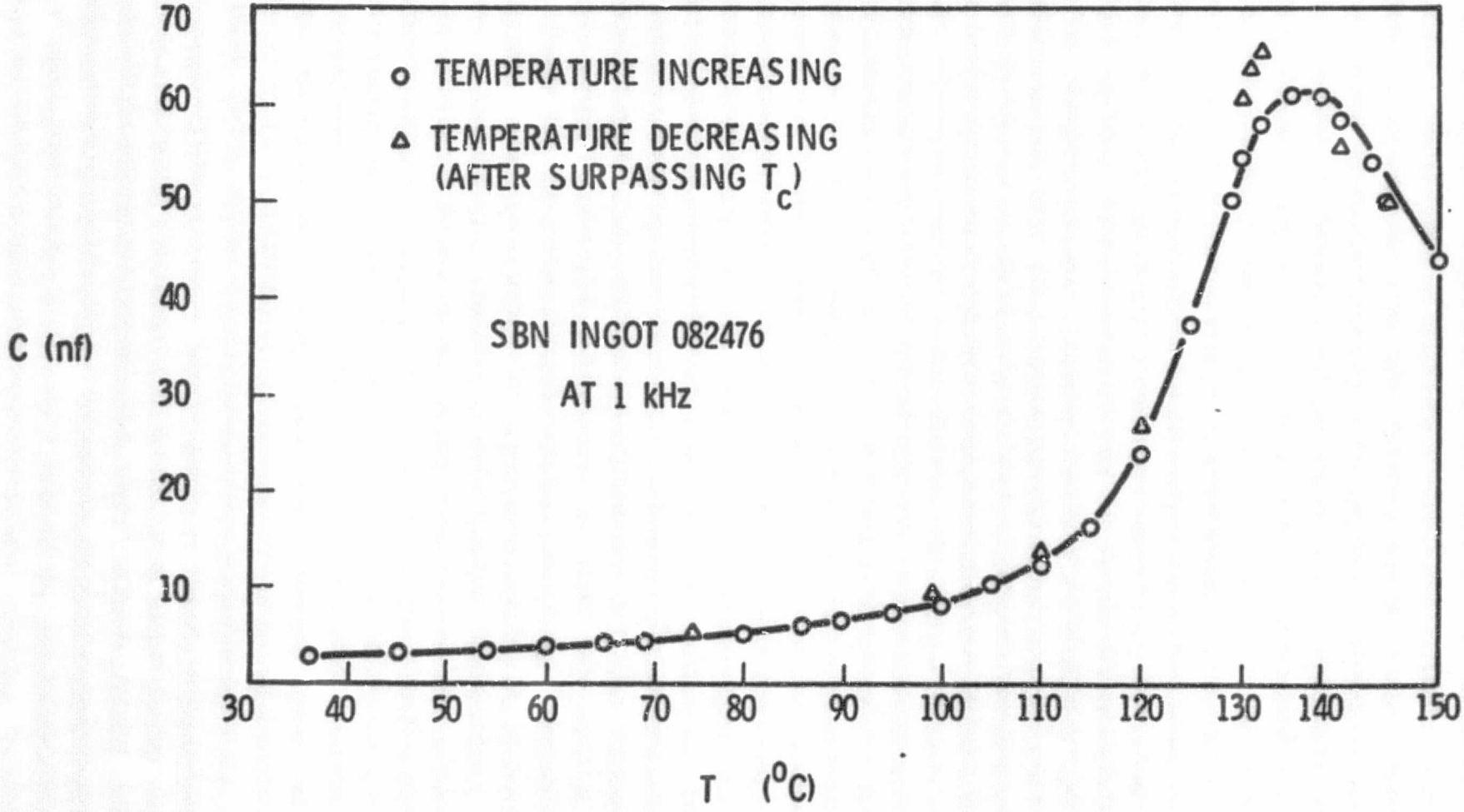

Figure 8 CAPACITANCE VS TEMPERATURE

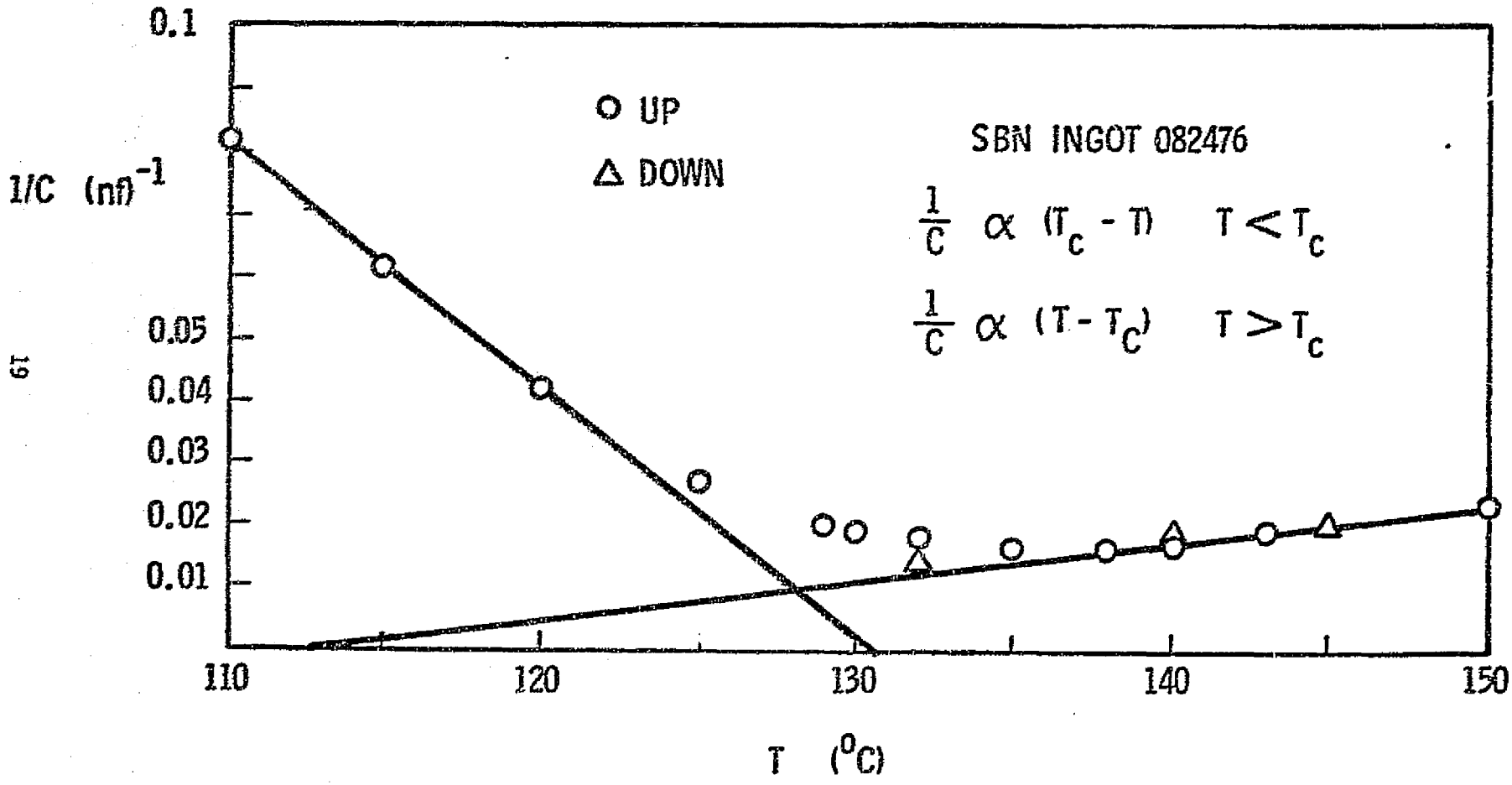

Figure 9 RECIPROCAL CAPACITANCE VS TEMPERATURE

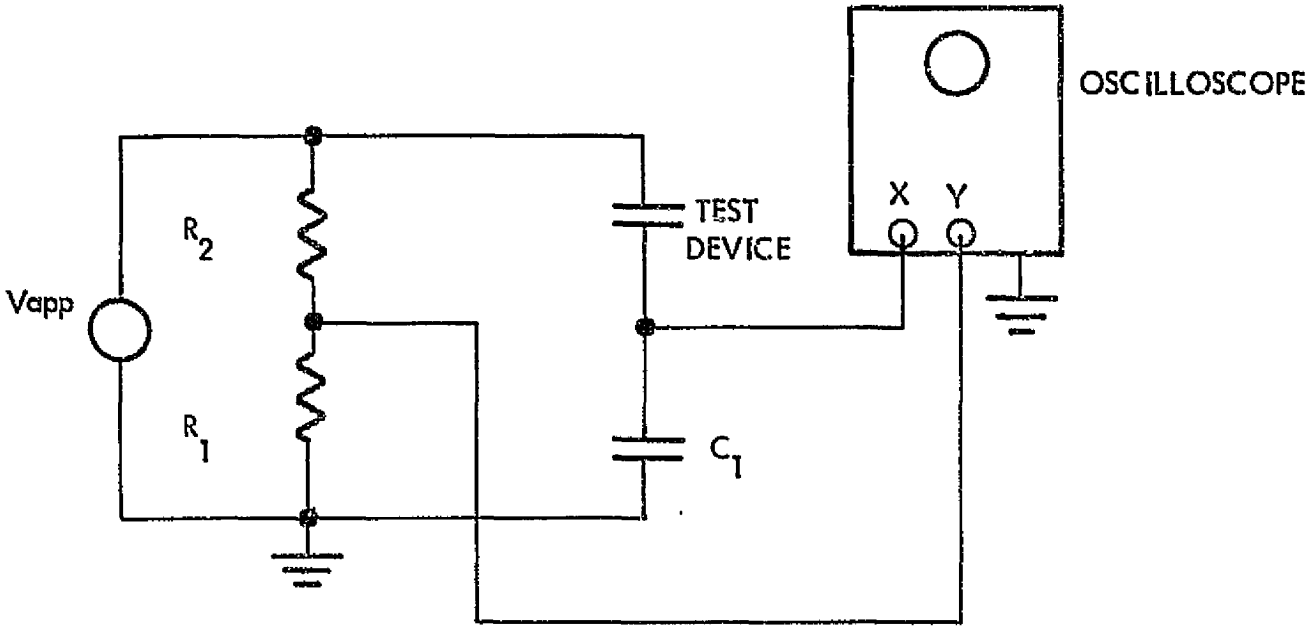

Figure 10 CIRCUIT USED TO MEASURE HYSTERESIS LOOP

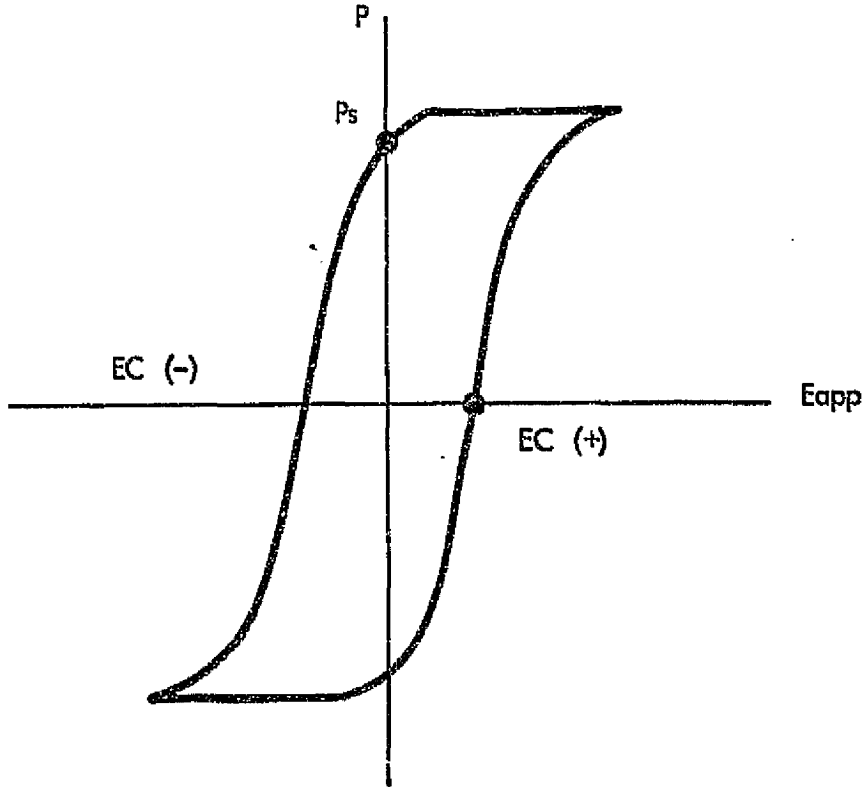

Figure 11 TYPICAL HYSTERESIS LOOP

Observation of the hysteresis loops of unpoled and poled SBN crystals has yielded interesting results. The SBN crystals used were grown from two different grades of starting material; called HP and HP2, with HP2 being the purer starting material. The hysteresis loop for unpoled material from 061176-H1(HP) is shown in Figure 12. Note that the loop is asymmetrical, with $F_c(-) > F_c(+1)$ (cf. Figure 11). Note also that the loop saturates at a lower magnitude of E_{app} in the (+) direction (Quadrant I) than in the (−) direction (Quadrant III). This indicates a favored direction of polarization in the material, namely in the (+) direction. This could be caused by an internal field set up by the impurities remaining from the originally less pure starting material. As the field remains applied, the loop degrades to that shown in Figure 13. It is difficult to saturate the polarization at all in the (−) direction, indicating strong internal fields in the (+) direction. P saturates very easily in the (+) direction, as would be expected from an internal field pointing in that direction. It seems as though poling is taking place in the ac field. This is possible if the material had a preference for aligning its dipoles in a particular direction.

After poling an 061176-HP sample, the same behavior was observed (degradation of hysteresis loop). However, this effect took place at a far faster rate. Typically, easily noticeable degradation took place in ~ 4 minutes for unpoled material, while only 10 seconds was required for poled material. After depoling (annealing at 150°C for 2 hours) the sample again behaved as outlined above for unpoled material. In both cases, after removing the applied field for a few minutes, the loop would recover somewhat (loss of orientation preference). However, reapplication of the field once again caused loop degradation.

A hysteresis loop from material of 081976-HP2 is shown in Figure 14. This loop is very symmetrical, and did not degrade with time. The value of P_s as computed from these data is $P_x = 6.7 \times 10^{-6}$ coul/cm^2. This value is a factor of 4.5 less than that reported elsewhere by Maciolek and Liu[5]. However, Maciolek and Liu obtained their value of P_s by cycling the sample through only one loop. They noted that the value of P_s decreases on subsequent loopings. Since the sample shown in Figure 14 was looped at 60 Hz, this could

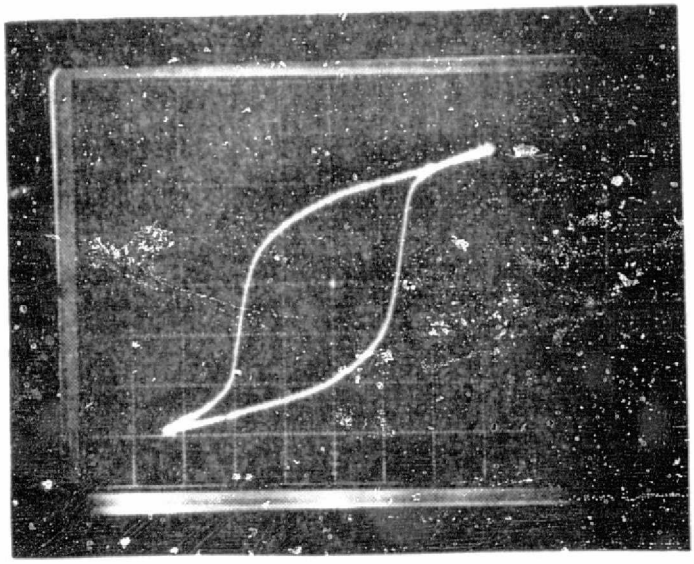

Figure 12 061176-H1 (HP)
Unpoled, Area = 8.9×10^{-3} cm^2
Vertical deflection = 0.1 volt/div.
Horizontal deflection = 2 volt/div.
Initial Curve

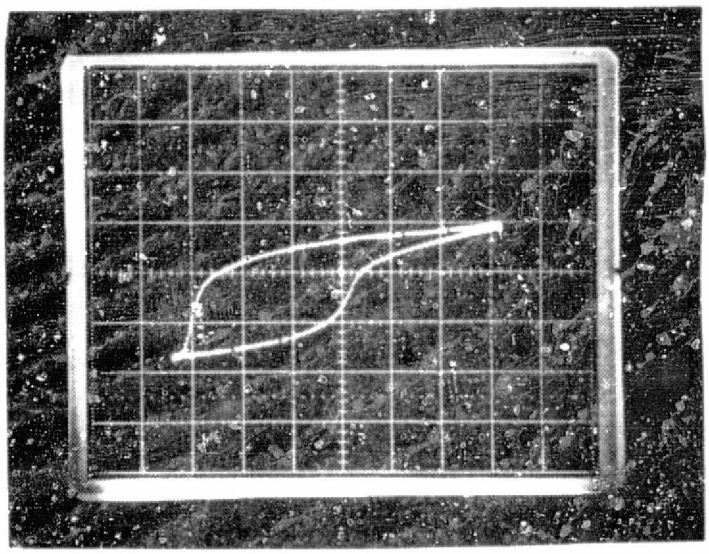

Figure 13 061176-H1 (HP)
Unpoled, Area = 8.9×10^{-3} cm^2
Vertical deflection = 0.2 volt/div.
Horizontal deflection = 2 volt/div.
after application of ac field

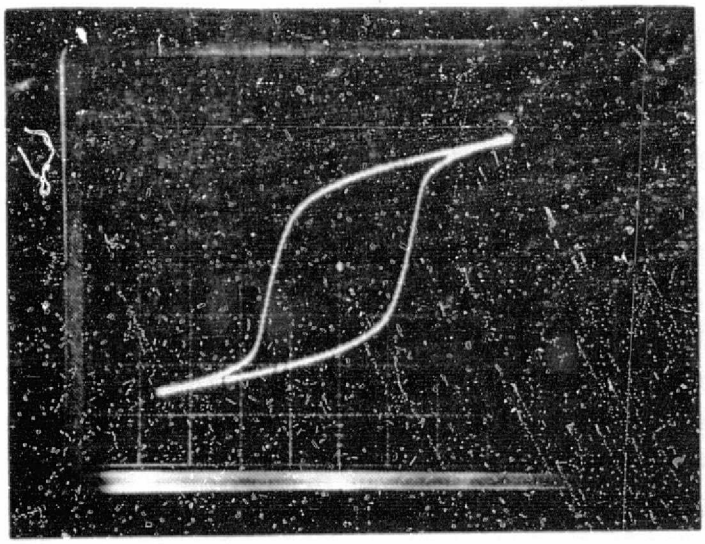

Figure 14 081976-02a (HP2)
Unpoled, Area = 2.4×10^{-2} cm^2
Vertical deflection = 0.5 volt/div.
Horizontal deflection = 1 volt/div.

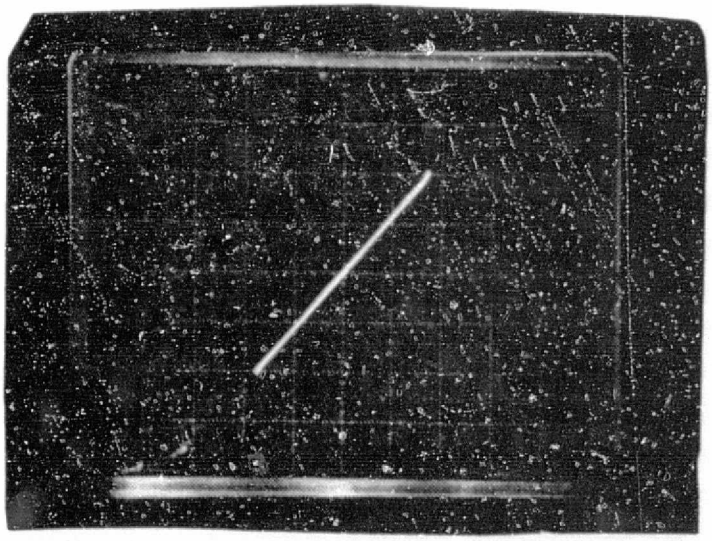

Figure 15 987 pF capacitor, nonferroelectric
Vertical deflection = 0.1 volt/div.
Horizontal deflection = 2 volt/div.

account for the discrepancy. This would also show that P_s approaches some final value, and does not decrease to zero due to continuous looping.

Table 3 summarizes the effect of the hysteresis looping of the capacitance and tan δ of the sample.

Table 3

EFFECTS OF HYSTERESIS LOOPING ON 061176-H1 (HP)

		120 Hz		1 KHz		
	Condition	C(pF)	tan δ	C(pF)	tan δ	
1)	Unpoled, unlooped	148	0.07	135	0.087	
2)	Unpoled, looped	182	0.82	72	0.25	
3)	Poled, unlooped	66	0.01	66	0.009	
4)	Poled, Looped	65	0.018	65	0.012	(10 min. after looping)
5)	Poled, looped	65	0.005	65	0.009	(+ overnight rest)
6)	Depoled, unlooped	144	0.08	130	0.095	
7)	Depoled, looped	192	0.65	77	0.3	

Conditions (1) and (6) show that the data for unpoled material are repeatable, even if hysteresis looping and poling has been performed. Conditions (2) and (7) also show that the data are repeatable. Note that, in conditions (1) and (6), the values of capacitance at 120 Hz and 1 kHz are only a few percent different. This is generally the case for this material. After looping, however, the 120 Hz value of capacitance increases, while the 1 kHz value of capacitance decreases by almost a factor of 2. It is interesting to note that generally for this material, the value of capacitance at both frequencies drops by a factor of 2 after poling.

After poling, and the definite establishment of a preferred dipole orientation, the capacitance and tan δ at both frequencies are not affected by the looping, if allowed to "rest" for a few hours. The effect of the looping is seen slightly only if the measurements are taken with 10 minutes of the looping procedure (Conditions 3, 4, 5).

The drastic effect of the looping on the tan δ of the unpoled samples could be explained by gross disordering of the domains within the material. One contribution to tan δ is thought to be large numbers of domain walls. Poling is thought to cause the material to become a single domain, lowering the tan δ. The disordering of domain walls caused by the alternating field could then cause this increase in tan δ.

In order to verify that the circuit itself was not causing the hysteresis loops, a capacitor made from a nonferroelectric material was inserted. The resulting curve is shown in Figure 15, showing the expected straight line from a nonferroelectric material.

SECTION 4

THIN DEVICE FABRICATION DEVELOPMENT

A major portion of this program was the development and optimization of the various facets of detector processing and fabrication. High detectivity pyroelectric detectors require completely different design and fabrication techniques than do moderate performance devices. The detectors must be very thin, well isolated from their thermal environment, have a good absorbing coating, etc. This section will discuss each of these areas of development in some detail.

4.1 THINNING

Equation 11 shows that D* can be maximized by making the detector as thin as possible, i.e., $D^* \alpha (d)^{-1/2}$ for frequencies greater than the thermal cutoff frequency ($f_o \approx 1$ Hz in this case). Since the detector must also have as small a path of thermal conduction as possible, this thin flake of detector material must be essentially free-hanging. These two factors (free-hanging, and extreme thinness) lead to certain fabrication requirements. SBN is a very brittle but fairly soft material. Therefore, mechanical thinning often leads to breakage. This is compounded by the stresses remaining in the SBN crystal from the growth process.

Several types of mechanical lapping procedures were attempted using various types of lapping surfaces and grits before a suitable procedure was developed. Automatic (machine) lapping was tried without success so a manual lapping technique was chosen. First the as-grown wafer is mounted on a lapping plug with wax. The sample is then lapped with 600 grit Silicon Carbide on a cast iron lap followed by 8 μm garnet on glass and 0.3 μm Al_2O_3 on silk. The wafer is then polished with 3 μm and 1 μm diamond on a rotating Texmet[6] pad. This provides a shiny mirror-like surface with little pitting. To bring the wafer to final thickness the process is repeated on the reverse side with the SiC used to do the bulk of the thinning. This method has given fairly high yields to thickness of 20 μm and greater. Some detectors as thin as 15 μm have been produced with this manual lapping technique. A major problem is

handling a wafer once it is thinned. Often a wafer will crack and break into several pieces while removing it from the lapping plug. Although this reduces the processing efficiency, the pieces are generally large enough to continue processing.

The final thinning and polishing steps are the most critical in the process. Several other techniques were used before the present diamond polishing was adopted. The main criteria for a good final polish are 1) only enough material should be removed so that the damage resulting from previous lapping steps is removed, and 2) a relatively damage-free and mirror-like polish is achieved, i.e., the polishing step produces less damage than it removes. The diamond polish on Texmet procedure fulfills these criteria. The amount of surface damage remaining after a polish is determined by etching the sample in warm (55°C) HF for 20 minutes. This etch attacks scratches and damaged areas faster than undamaged areas leaving distinct pits and scratches. Figure 16 shows an etched sample which was polished with Linde A (0.3 μm Al_2O_3) on glass. Note the numerous pits and sharp V shaped scratches. This shows much surface damage, probably leading to a poor tan δ in the final device. Figure 17 shows a sample prepared in the same manner except that 3 μm diamond on Texmet was used as the final polish. Note the almost complete lack of etch pits and the more rounded ("U" shaped) appearance of the scratches. There are more scratches in this sample due either to scratches remaining from the lapping procedure or a contaminated wheel. In either case, further polishing (on a clean wheel) does remove most of the remaining scratches. Also, further polishing with a finer grit (1 μm diamond) further improves the surface quality. The diamond produces less damage because the process is a cutting rather than grinding technique. The diamond particles are imbedded in the Texmet surface and act as multiple knives to shave away the surface of the SBN cleanly. The alumina and other abrasive powders remove material by rolling between the lap and the surface to be polished thereby grinding away material and introducing damage as a by-product.

Although this manual, mechanical lapping and polishing procedure works well for relatively thick samples (20 to 25 μm), optimized detectors should be thinner. It is felt that no mechanical means can produce very thin

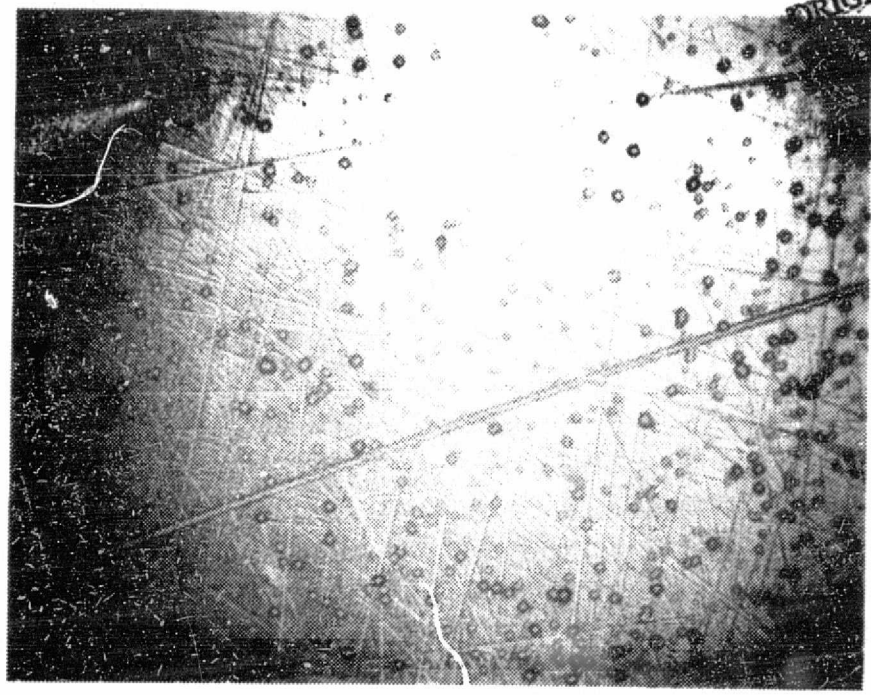

Figure 16 SBN WAFER POLISHED WITH LINDE A AND ETCHED

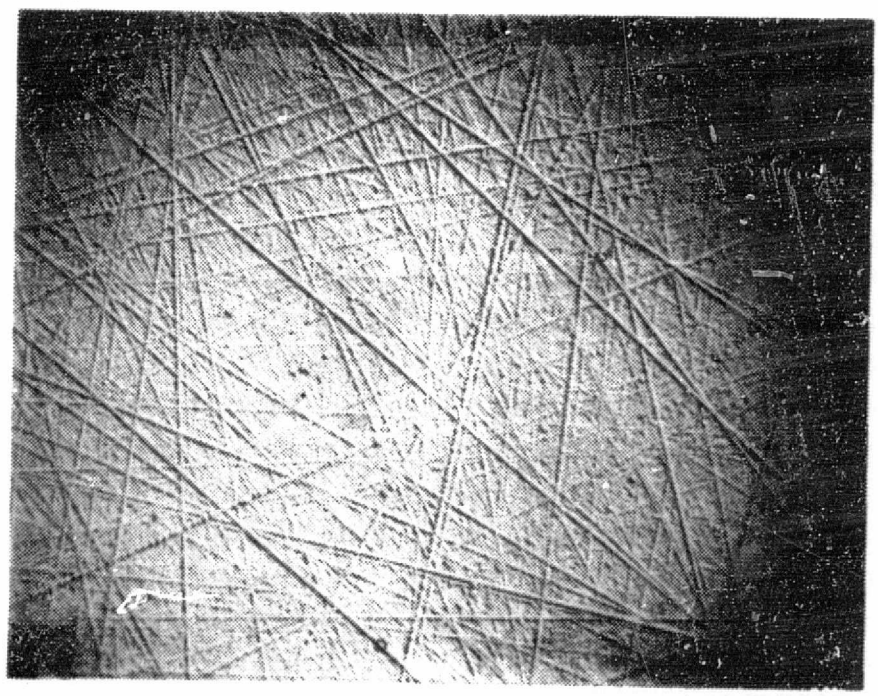

Figure 17 SBN WAFER POLISHED WITH 3 μm DIAMOND AND ETCHED

(< 10 μm) SBN. Therefore, ion beam milling was evaluated as an alternative thinning technique. Ion beam milling removes a layer of material by bombarding the material with inert gas ions (usually argon). These ions are energetic enough to knock molecules from the surface of the material to be milled but not of high enough energy to cause bulk damage (generally energies of 100 to 2000 eV are used). The ion beam is collimated and its direction, energy and current can be controlled. The target material generally sits on a water cooled rotating stage for temperature control and to achieve uniform removal.

Most of the ion beam milling experiments conducted during the program were done at Honeywell Corporate Material Science Center in Bloomington, Minnesota. The ion miller used was a Honeywell designed and built unit, however a commercial unit has since been set up and is in operation at EOC in Lexington. The first experiments determined the optimum milling angles and rates. Figure 18 shows the experimental angular dependence obtained. The optimum rate is obtained when the surface is 60° from the beam axis.

This dependence is fairly typical of many dielectric materials. The rate decreases at higher angles because much of the milled material redeposits on the surface. At shallower angles the cross section is reduced which slows the milling. The rates obtained with this miller on SBN at 60° were about 1 μm per hour.

Several milling experiments were conducted to determine if flatness of a lapped sample of SBN is preserved (or improved) during milling and if thin wafers can be produced. The third quarterly report discusses the flatness aspects. Basically, the milled surface is quite flat; actually improving the topology of the lapped surface. This is to be expected from the geometry of the experimental runs. Several problems developed whenever a sample was thinned below about 20 μm. Often the sample would crack severely and fall apart when demounted from its substrate. It was determined that the probable cause for the behavior was the thermal stresses built up during the milling operation. Even though the table is water cooled, the sample temperature does rise to approximately $100^{\circ}C$. Even with this small temperature rise, the differences in thermal expansion of the SBN, the substrate and the wax holding

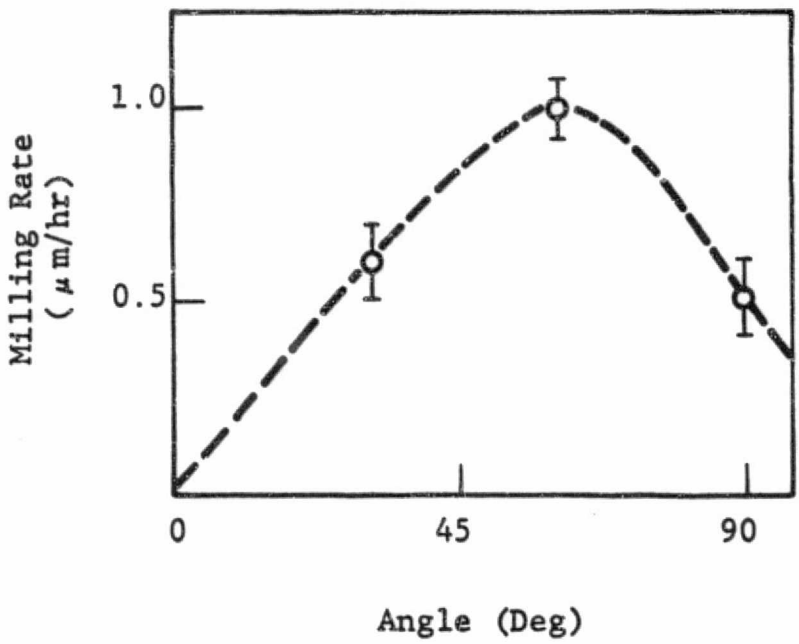

Figure 18 ANGULAR DEPENDENCE OF MILLING RATE FOR SBN

them together is enough to fracture the sample on sharp scratches. The bulk of the experiments were done with samples which were not diamond polished so there was a high degree of damage present in the material. There were also many sharp scratches present. Therefore, a small stress by a thermal expansion is concentrated in the scratches and causes a fracture. A substrate must be used because the wafer becomes too thin to handle without a substrate (often Corning Photoform was used as a substrate due to further processing consideration but almost any material would lead to the same problems).

One partial solution to this problem is the milling of both sides to provide a smooth (scratch-free) surface on the backside before the frontside (final thinning) is accomplished. This method allowed for thinner samples but eventually the thermal mismatch fractured the samples. A better mounting method is needed but these must wait for future work.

In conclusion, the ion beam milling provides a method for thinning beyond the point achievable with manual lapping. Some additional work is required to optimize the technique however.

4.2 MOUNTING

The mounting structure for a high performance pyroelectric detector must fulfill two criteria: hold the detector rigidly enough to keep microphonics very low and keep the detector in good thermal isolation from its environment. Often both of these requirements are mutually exclusive so a tradeoff between the two goals must be reached. The thermal requirement would be fulfilled by suspending the detector chip from its thin lead wires but microphonics would be very high and the detector would be quite fragile. Several mounting schemes were investigated during the program. Most of these were rejected after certain difficult technological problems were found. This section describes the mounting methods used.

The first mounting scheme which was attempted was the so-called "flip-over" technique. A schematic of this procedure is shown in Figure 19. Basically, this scheme involves the polishing, electroding and blackening of one surface

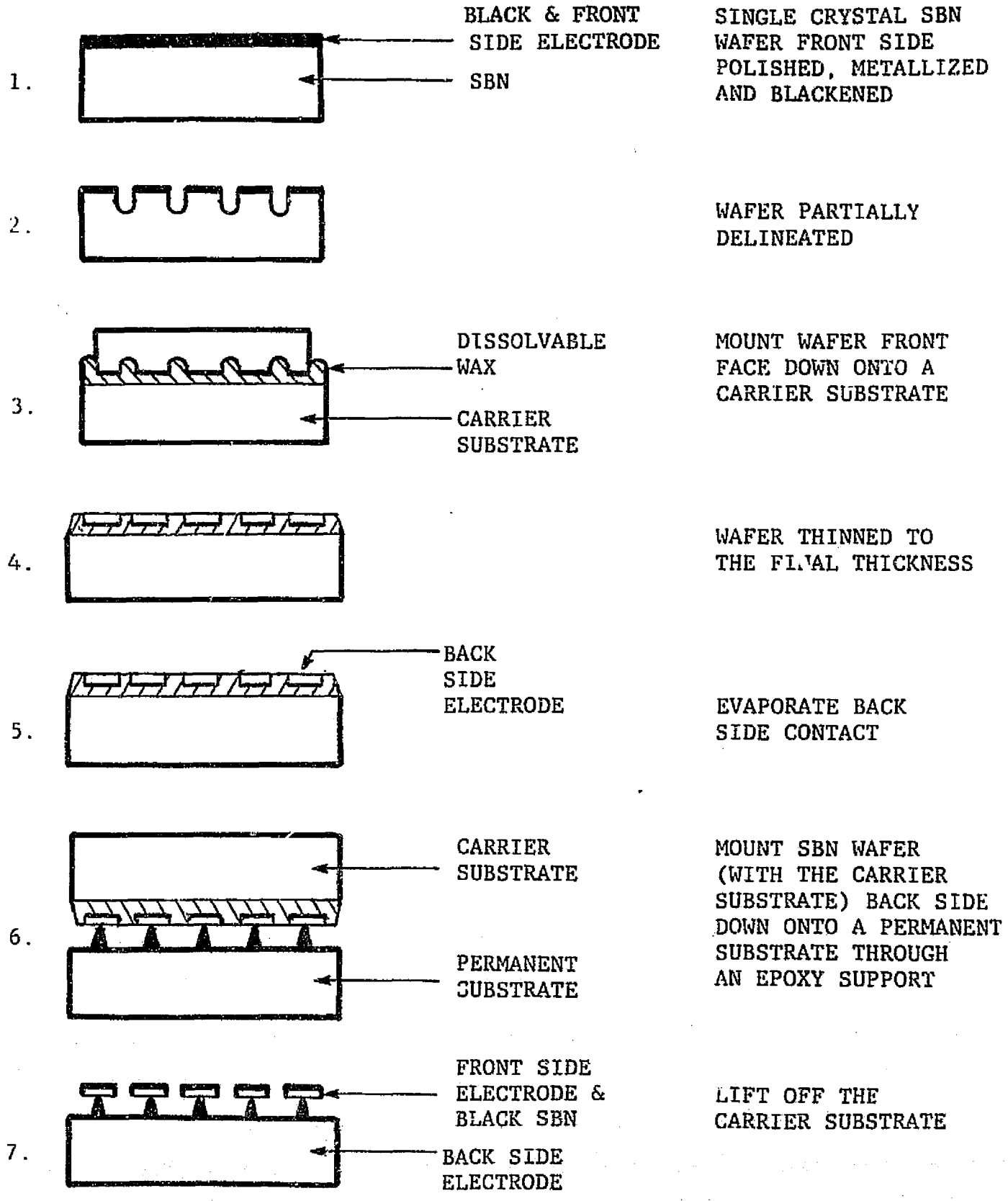

Figure 19 "FLIP-OVER" FABRICATION PROCESS

7808-11

(to be the front side) and subsequent delineation of this surface by partially sawing through the wafer. This side of the wafer is then bonded with wax to an intermediate substrate and the back side is lapped, polished and electroded. The fully delineated chips are then flipped onto a permanent substrate and the wax is dissolved, freeing the carrier substrate. Problems with this procedure were primarily with the back side thinning. Thermal and mechanical properties of the wax caused cracking of the SBN. For detectors less than 20 μm thick the yield was very low.

The second mounting technique used a wax-filled glass substrate to hold the wafer during thinning after which the wax was dissolved leaving the detector mounted only by its edges. A schematic representation of the steps in this mounting procedure is shown in Figure 20. Several problems with this technique became evident early in its use. First, the glycol phthalate wax used to fill the holes shrinks slightly during cooling. Therefore, a small void occurs under the SBN at the holes and therefore the SBN dimples at these locations. Even if this problem is solved the physical hardness of the wax is quite different from that of the glass. This causes excessive stresses during thinning and cracks around the glass-wax interface to develop. Therefore, this technique was abandoned.

A third mounting scheme is shown in Figure 21. It is quite similar in structure to the previous technique except that Corning Foto-Form glass is used. This is a chemically altered, photo-sensitized glass which is selectively etchable. This technique removes the major problems of the wax-filled glass by using a solid glass substrate during the thinning and polishing operations. Only after these critical steps are accomplished is the glass under the SBN removed by etching in HF. Wherever the glass has been sensitized by ultraviolet radiation the etch rate is much faster than the bulk. Unfortunately, several problems developed with this technique also. The etching in a still bath of HF is not uniform. The hole enlarges radially faster than it etches through. This causes a failure of the detector (because there is no mounting surface left). If agitation is used the etching is more uniform but as soon as the glass is etched through, the agitation bursts through the detector. Because of these and other technological problems this technique was also abandoned.

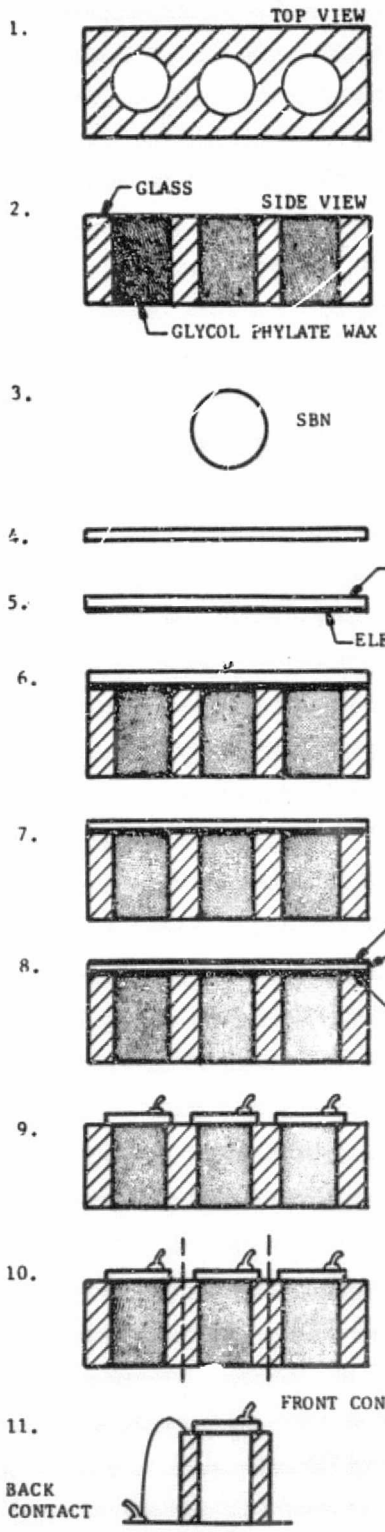

Use 0.5 mm thick glass substrate with 1 mm holes.

Back fill the holes with glycol phylate wax which hardens at room temperature and is dissolvable in acetone.

Select low loss tan δ SBN wafer which is cut parallel to the polarization axis (wafer diameter ~ 1 cm, wafer thickness 0.5 mm).

Mechanically polish the wafer to about 40 μm and chemically etch to eliminate surface damage.

Put on back side contact

Mount back side down on the prepared (back filled) substrate and mechanically polish the SBN to about 20 μm.

Chemically etch to final desired device thickness.

Apply front side contact, electroplate gold black and pole

Thermal compression bond (front contact)

Dice the substrate.

Remove glycol phylate and mount the device on header with contacting paste.

Figure 20 SCHEMATIC OUTLINE OF WAX FILLED FABRICATION PROCEDURES

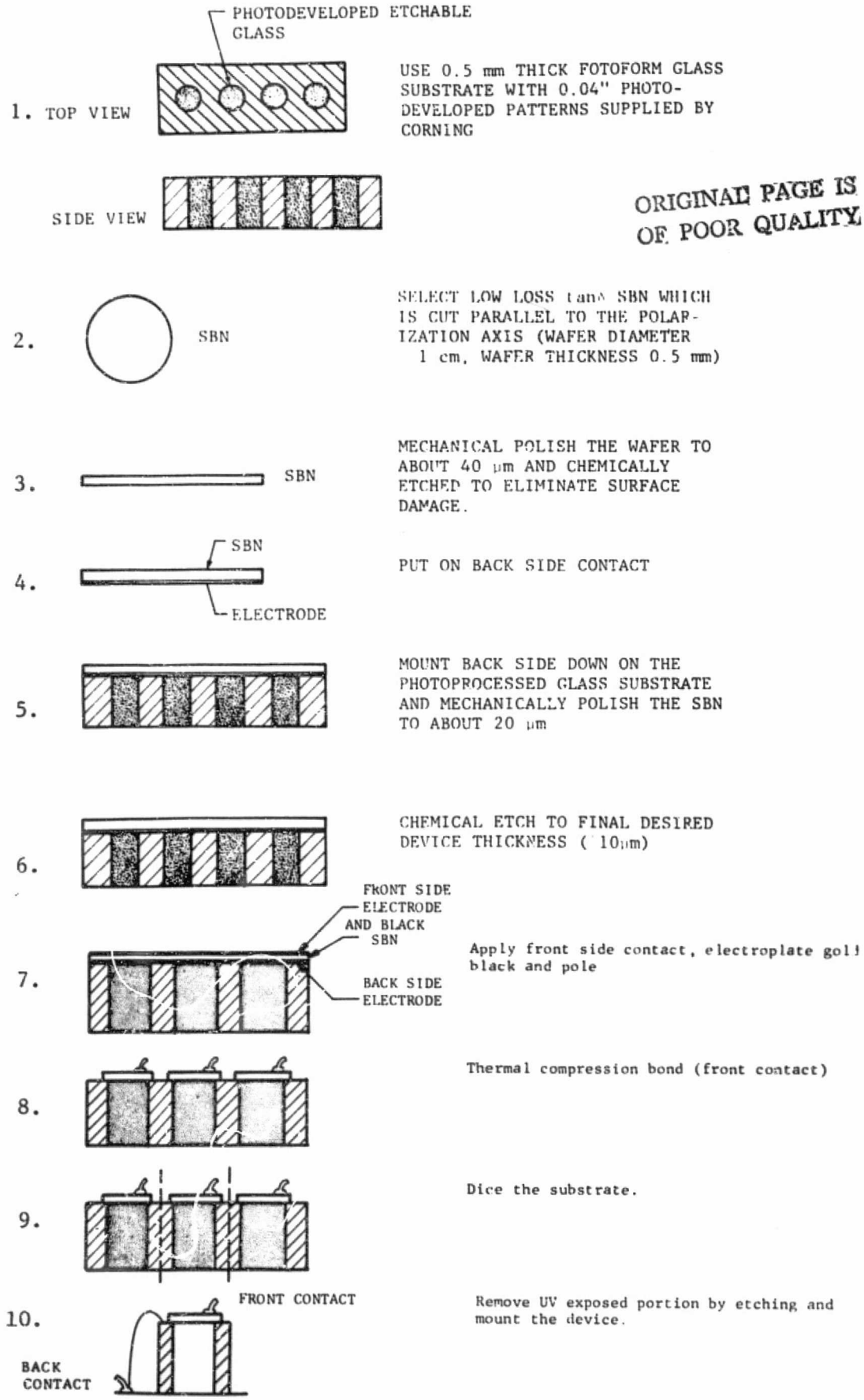

ORIGINAL PAGE IS OF POOR QUALITY

Figure 21 SCHEMATIC OUTLINE OF PHOTOFORM GLASS PROCEDURES

A modification of the photoform scheme was attempted using ion beam milling as discussed in the previous section. Problems with thermal expansion coefficient mismatches plagued this technique.

The mounting technique which gave the best results and which is used for the deliverable detectors is a single point suspension technique. The detector is mounted on a small gold wire (0.001" diameter) with conducting epoxy. This lead is brought up through a hole in a thin mylar sheet which is mounted on a thin-walled glass capillary. A diagram of the mounting structure is shown in Figure 22. The consistency of thermal properties from one device to another is difficult to control due to the difference in the size of the epoxy dot holding the detector. Generally, however, the devices showed good thermal properties (thermal rolloff frequency < 5 Hz) and fairly low microphonics.

Other techniques such as mounting the chip with several (3 or 4) small epoxy dots onto the circuit board or by directly epoxying a thinned chip onto a glass capillary may also work and should be investigated in the future.

4.3 ELECTRODES

The electroding for the devices consists of a platinum-filled liquid which is painted onto the front and back surfaces of the samples. After air-drying in a 60°C oven, the sample is then sintered at 650°C for 10 minutes. Together with the heat-up and cooldown cycles, the whole sintering processing takes 30 minutes. This process yields a Pt electrode 500 Å thick, thus preventing excessive heat loss to the electrodes. Since the blackening solution is a Pt black, the use of Pt as electrodes was a logical choice.

Another electrode which was tried was evaporated nickel. However, this metal was attacked by the blackening solution, and thus required extra safeguards to prevent destruction of the electrode. With the Pt electrodes, no such precautions were necessary.

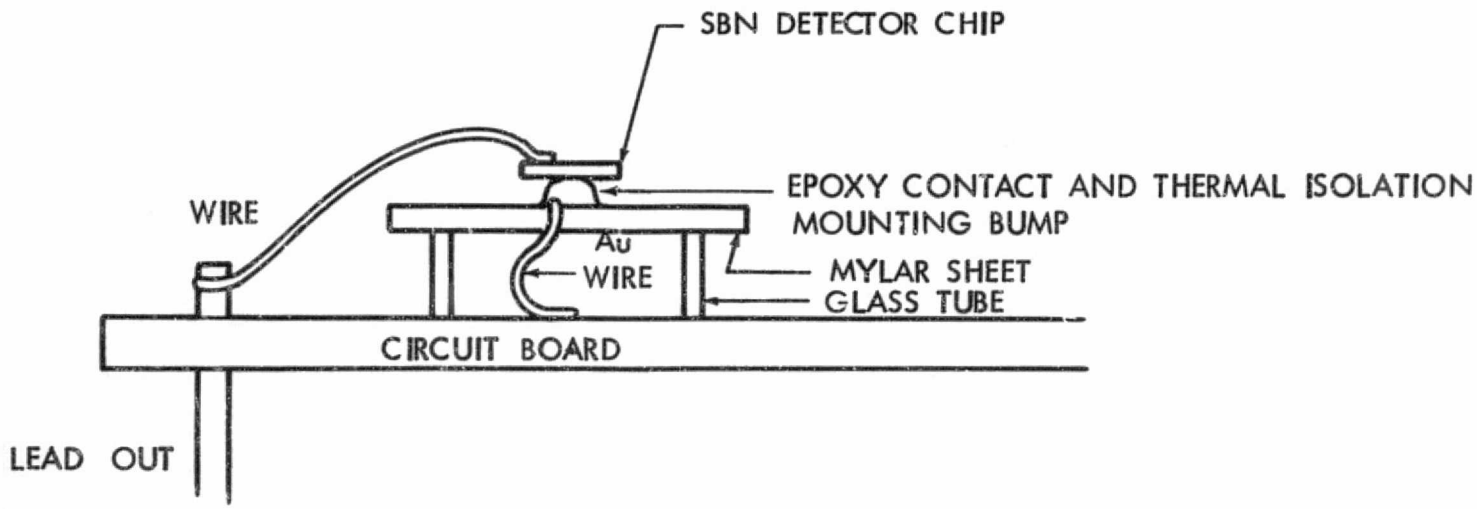

Figure 22 SINGLE POINT MOUNT USED TO OBTAIN MAXIMUM THERMAL ISOLATION

4.4 FRONT-SURFACE BLACKENING

To cause the front-surface emissivity (η) to approach unity, thus optimizing the device performance, the front-surface electrode was blackened. This black is formed by electroplating Pt from an ionic Pt solution at a rapid rate. The Pt atoms are deposited on the detector front electrode surface in the disordered fashion which, when viewed under an electron microscope, has the appearance of the top of a pine forest. It is these many angular protrusions which cause the incident energy to be absorbed by multiple internal reflections, resulting in a "black" surface.

Experiments were conducted to determine the optimum plating current and time. When the plating current is too small, the Pt atoms are deposited in an ordered fashion, resulting in a smooth, reflecting Pt film. If, however, the plating current is too high, bubbles are formed on the surface of the plated electrode, and these result in a splotchy black. Also, when the deposition rate is high, it is difficult to regulate the mass of Pt deposited. Too large a mass of the black will cause a degradation in device performance.

The optimum plating current density was found to be ~ 0.3 amp/cm^2, being plated for ≈ 50 seconds. These resulted in uniform, reproducible black coatings. Figure 23 shows reflectance data of various black coatings, deposited on a Cr-Au electrode on a glass slide. This shows a value for $\eta \sim 0.95$ for a good Pt black.

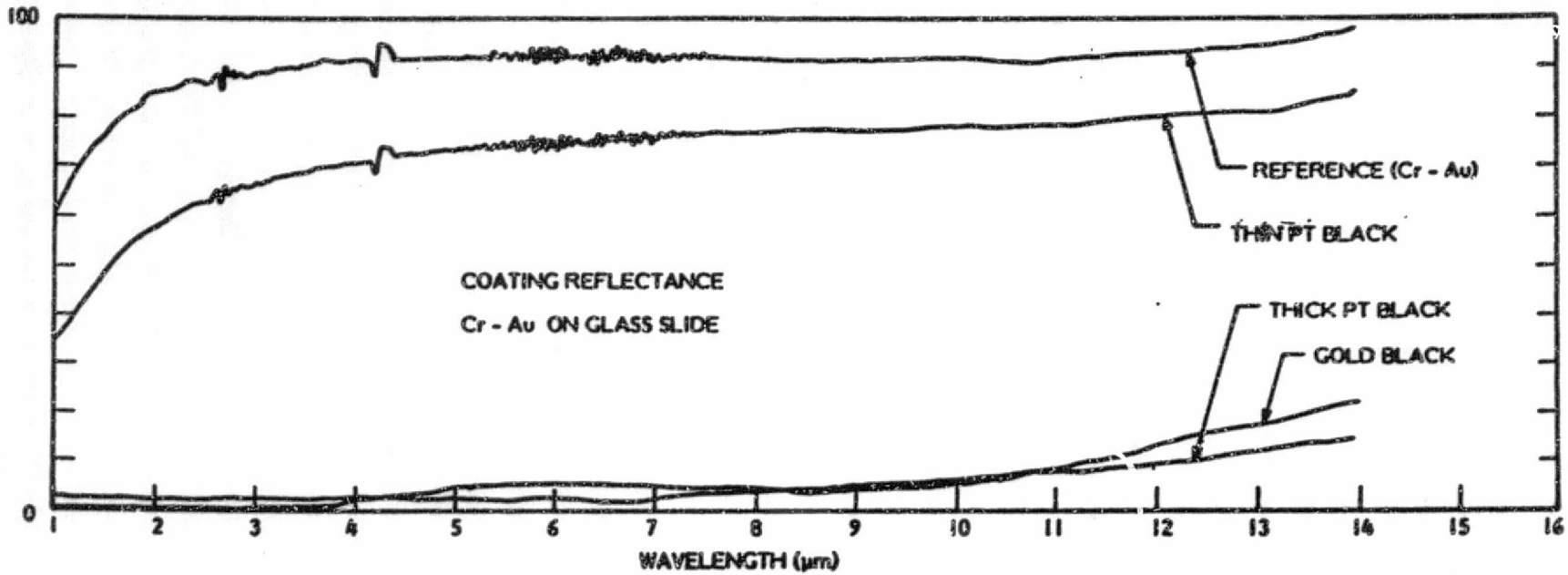

Figure 23 REFLECTANCE VS WAVELENGTH SHOWING PLATINUM BLACK EXCEEDS 90% EMISSIVITY FOR ALL WAVELENGTHS LESS THAN 12 μm

SECTION 5
SBN DETECTOR POLING

It has been observed that the loss factor, tan δ, depends on poling. The poling technique has been continuously improved at Honeywell. Prior to this contract SBN detectors with tan of 0.003 have been achieved. During poling, the device is held at an elevated temperature (close to the Curie temperature of the material). A high field (>20 kV/cm) is applied to the device for a few hours and then the device is allowed to slowly cool down to room temperature under the high field.

The goals were to maximize the pyroelectric coefficient (for high responsivity), to minimize the tan δ (for low noise), and to minimize the dielectric constant (for high responsivity).

5.1 THE POLING TECHNIQUE

Detectors are poled using an apparatus shown in Figure 24. At the beginning of an experimental run, the capacitance and tan δ were measured and the SBN flake temperature recorded. To permit a high degree of freedom of movement of the dipoles and any impurities in the material, the samples were heated to a temperature above the Curie temperature. A high field is then applied, and current measured at various times during the poling process.

After a prescribed poling time, the oven was turned off and allowed to cool slowly with the field still applied. (Rapid cooling tended to crack the SBN sample when very thin (~10 μm)). When the temperature was $T \leq 50^{\circ}C$, the field would be removed. After a stabilization period, the capacitance and tan δ were again measured. These final measurements must be taken at the same temperature as the initial measurements, since both capacitance and tan δ are functions of temperature.

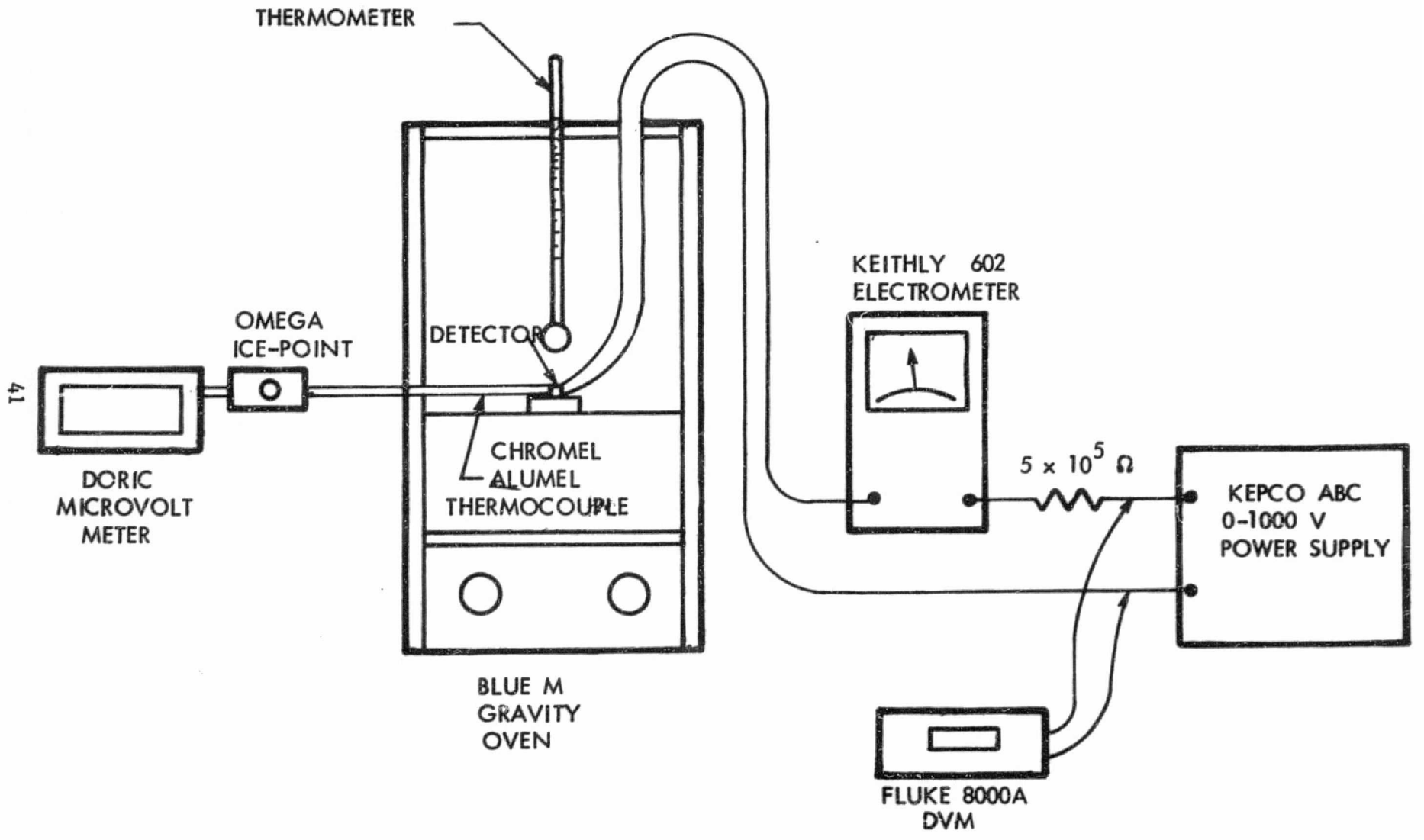

Figure 24 POLING APPARATUS FOR SBN DETECTORS

5.2 TAN δ RESULTS

The Tan δ (loss tangent, dissipation factor) is a measure of the dielectric loss in a capacitor. It is represented by an ac shunt resistivity and defined by $\tan\delta = \frac{1}{\omega RC}$, where $R = \frac{\rho d}{A}$ and ρ is the ac resistivity, d the sample thickness, and A the sample area. Thus, the tan δ would decrease if ρ(ac) was to increase. It must be noted that C decreases with poling and this, too, will affect the value of tan δ. This will be discussed further on.

During poling, the dc current was monitored. From that current, the applied voltage, and the sample dimensions ρ(dc) could be obtained. Although ρ(dc) ≠ ρ(ac) (they often differ by a factor of 1000, ρ(dc) > ρ(ac)), the dc resistivity gives an indication of the ac resistivity.

Samples of experimental values of poling current versus time are plotted in Figures 25 and 26. These show a continued increase of the dc resistivity with time, until some final value is achieved. Presumably at that point the maximum value of ρ(dc) has been attained.

If the Δρ (ac) = Δρ (dc), we should be able to calculate the expected final tan δ after poling. We would also need to know the ΔC after poling. The $\tan\delta\,(\text{final}) = \tan\delta\,(\text{initial}) \times \frac{1}{\Delta\rho\Delta C}$. Here $\Delta\rho = \frac{\rho(\text{final})}{\rho(\text{initial})}$, $\Delta C = \frac{C\ (\text{final})}{C\ (\text{initial})}$. The required values for this calculation for three samples are listed in Table 4.

Table 4 TAN δ IMPROVEMENT BY POLING FOR SAMPLES FROM 3 INGOTS

Ingot	$\Delta\rho$	ΔC(1KHz)	Tan δ (Initial) (1KHz)	Tan δ (Final) (1KHz)	Tan δ Calculated
080376-02	2100	0.54	0.078	0.0007	0.00007
082076-01	414	0.5	0.077	0.0002	0.0004
082576-01	118	0.38	0.099	0.0017	0.002

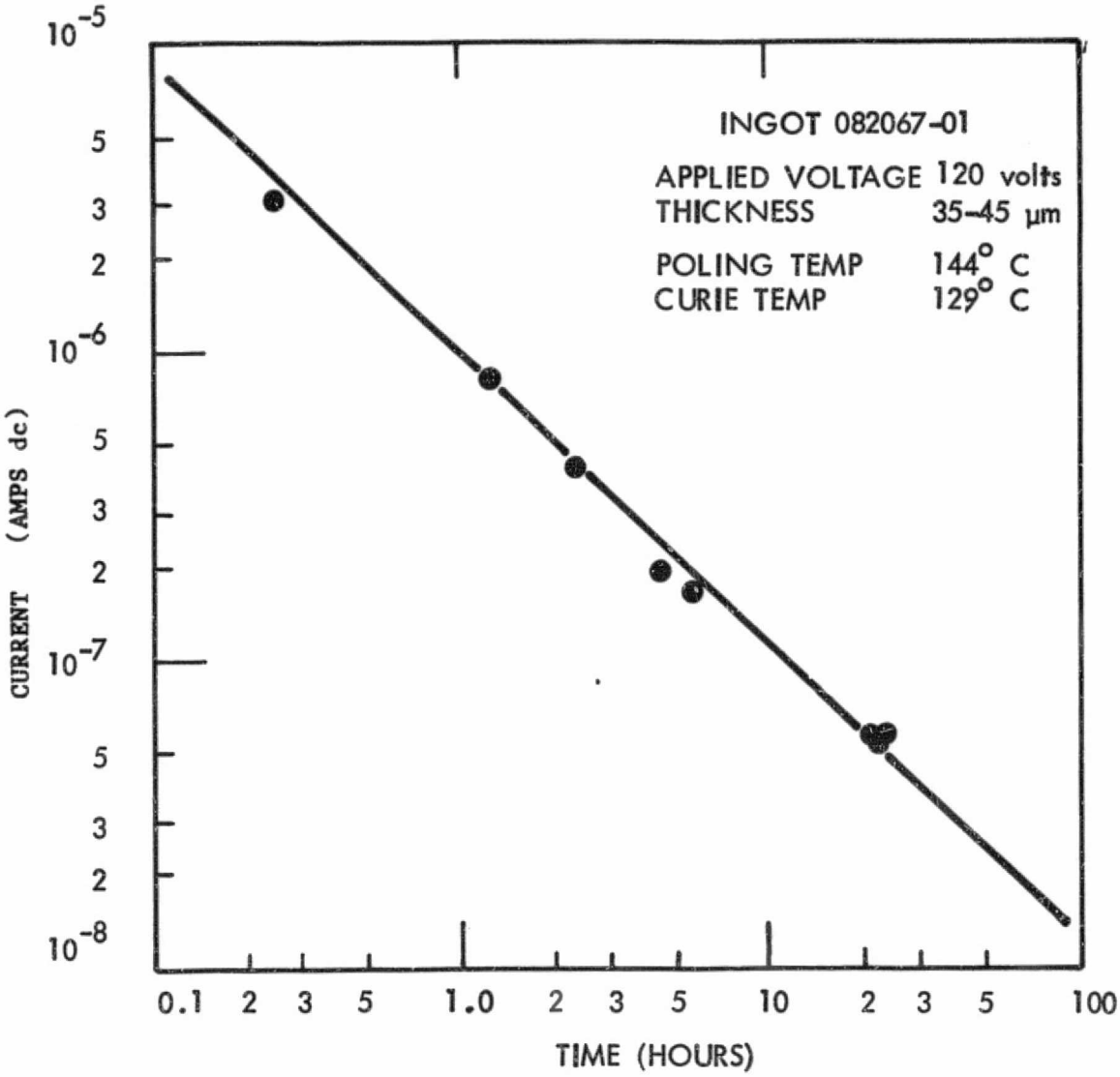

Figure 25 POLING CURRENT VERSUS TIME

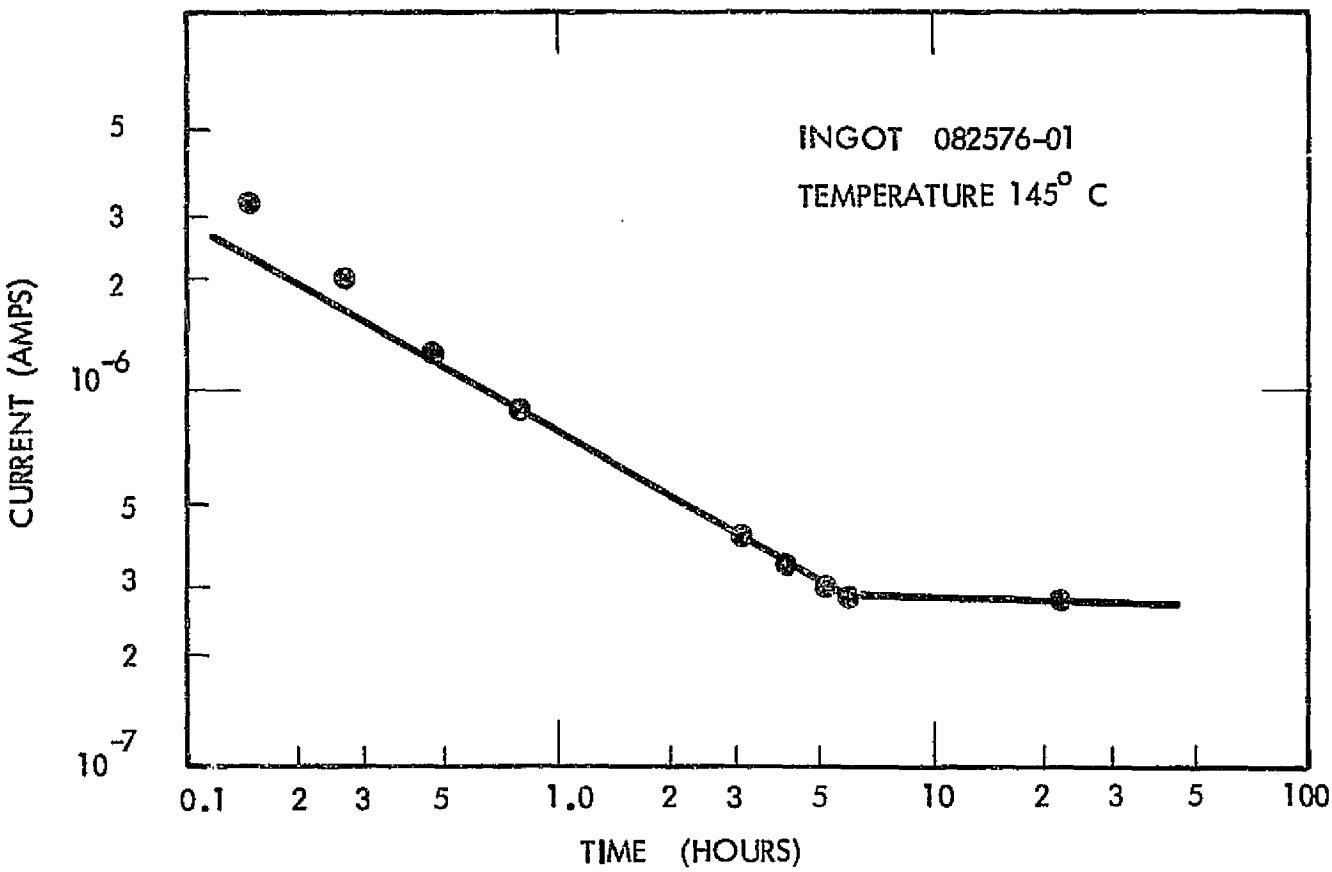

Figure 26 SBN POLING CURRENT VERSUS TIME SHOWING IMPROVEMENT UP TO SIX (6) HOURS

There is fair agreement between the calculated final tan δ and the experimental final tan δ. It should be noted that, for the observed tan δ values, the capacitance bridge which was used (GR 1657 Digibridge) had an accuracy of $\pm$100%. Final values of tan δ (1 kHz) for various samples are shown in Table 3, along with poling conditions.

Flake 080576 shows the behavior of tan δ with respect to poling time, temperature and field very well. The samples 080576-01 thru 04 were all from the same slab. With the same field applied (1.4 V/μm) on flakes 080576-01, 02, 03 the tan δ decreases as the poling time increases. However, when 080576-04 was poled at room temperature, with a higher field and longer time than the first three samples, the tan δ was very poor. These data are summarized in Figure 27. This same result was observed for 080476. One half of this flake was poled at room temperature and the other half at 145°C, above the Curie temperatures. Table 5 shows the substantial difference in final tan δ, and indicates that a high temperature does indeed aid in the reduction of the tan δ. It has been suggested that the tan δ is in part caused by impurities in the bulk material, and that the reduction of the tan δ is partly caused by the migration of the impurities to the electrodes under the influence of the applied field. This suggestion is supported by two observations: 1) the change in ρ(ac) is very similar to that of ρ(dc). This is indicated by the calculated values given in Table 4. Since ρ(dc) is influenced (largely) by impurities, it seems that in this case ρ(ac) is influenced by impurities, 2) the tan δ decreases far more rapidly, and to lower values, when the field is applied to a heated sample. The higher lattice temperature would allow the impurities to migrate much more easily than would a cold lattice. It was noted that not all samples showed good correlation between Δ ρ(ac) and tan δ reduction.

5.3 PYROELECTRIC COEFFICIENT

The pyroelectric coefficient is defined as being: $p = \frac{-dPs}{dT}$ the change in the spontaneous polarization (P_s) with temperature. The larger the change in P_s with temperature, the more sensitive the device will be to a given temperature change. It is known that having a sample's dipoles completely aligned would maximize this value of p, and this alignment can be brought about by

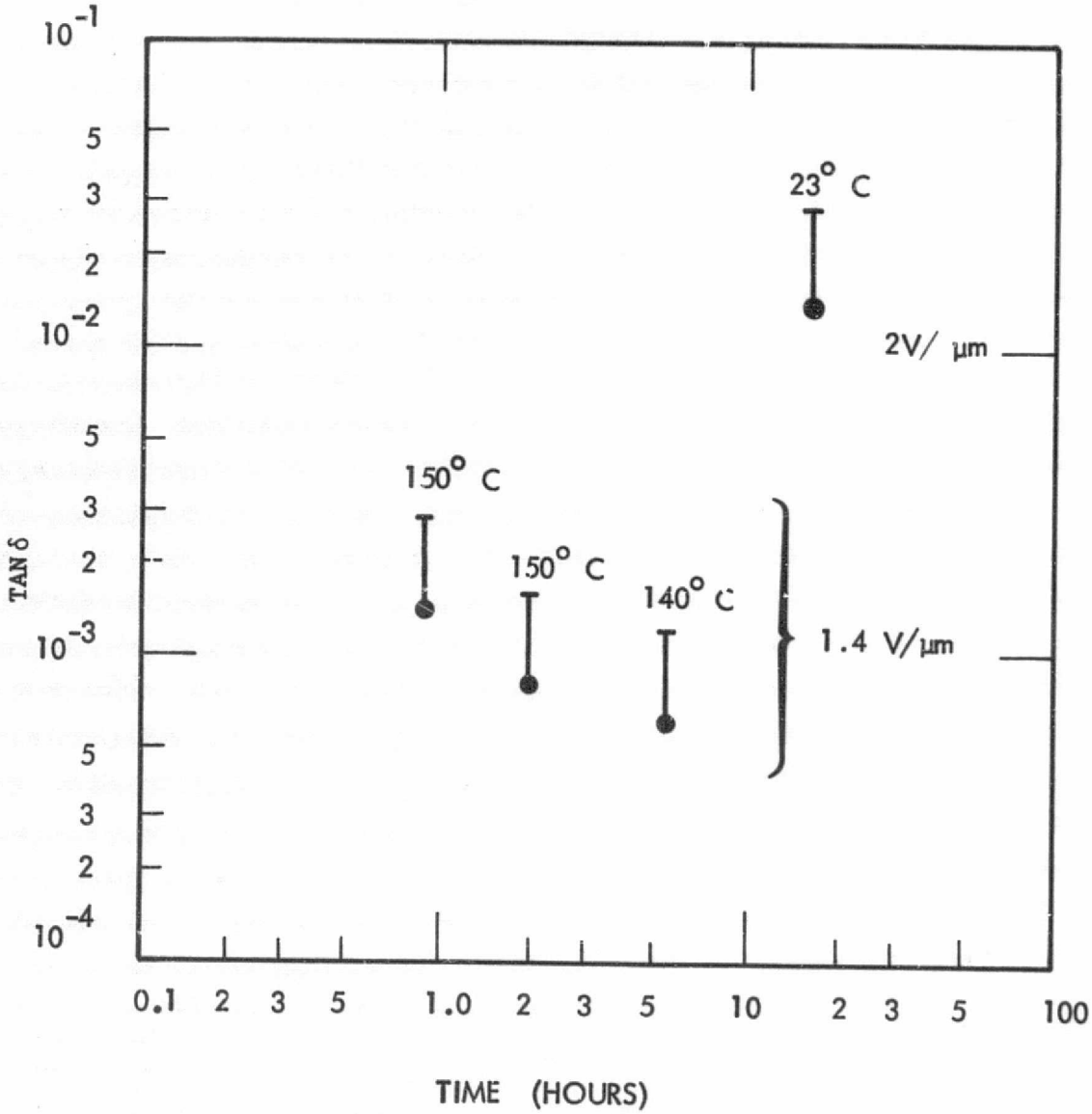

Figure 27 TAN δ AS A FUNCTION OF TIME SHOWING IMPROVEMENT OUT TO SIX (6) HOURS AT ELEVATED TEMPERATURE

Table 5

TAN δ SUMMARY

Ingot	Poling Conditions Time (hrs)	Temp. (°C)	Field (V/μm)	tan δ (1KHz) (±100%)
061176-H1	6	145	2.3	0.009
061176-01	65	154	2.3	0.0024
080376-01	113	144	3	0.0035*
080376-02	30	150	2	0.0007
080576-01	0.88	150	1.4	0.0014
080576-02	5.5	140	1.4	0.0006
080576-03	2	150	1.4	0.0008
080576-04	16.2	23	2	0.0140
080576-05	4	150	2	0.0250 +
082076-00	0.66	150	5	0.0150 +
082076-01	26.5	145	3	0.0002
082076-02				lost in power failure
082476-01	0.66	145	2.4	0.0007
082476-02	0.05	22	0.3	0.0120
082576-01	24.6	146	3	0.0017
082076-S1-02	49	141	3	0.0015
082076-S1-04		lost in process		

* Power supply switched off during poling.

+ Very thin (10-13 μm) samples.

poling the material. The application of an electric field parallel to the polar axis of the crystal will orient the dipoles. In a sample at room temperature, there will naturally be forces which tend to counteract the aligning effect of the applied field. These forces can be overcome by heating the sample. In particular, heating above the Curie temperature would completely disorient all the dipoles, preventing the field from having to work against some previous alignment.

The pyroelectric coefficients were measured in a thermoelectric cooler assembly as follows using the apparatus shown in Figure 28. A chromel-alumel thermocouple was used to monitor the detector (air) temperature. A $1^{o}C$ temperature change was effected and the resultant charge on the detector, given by $\Delta q = pA\Delta T$, was integrated using the Keithley 602 electrometer. From this value of q, and the detector area, the pyroelectric coefficient, p , could easily be computed. This procedure was repeated several times, with both a positive and negative ΔT. Some of the ΔT values were $2^{o}C$. It is important, however, that not too large a value of ΔT be used, because the pyroelectric coefficient is a function of temperature.

The resultant pyroelectric coefficients obtained for different poling conditions are summarized in Table 6. There is a maximum variation of approximately 43% that occurs when a sample was poled at room temperature, for a short time, and with a low field. A comparison of Figures 27 and 29 would be useful to illustrate the effect of the poling conditions on the two parameters $\tan\delta$ and p. There is a substantial (factor of 20) variation in $\tan\delta$ for the different poling conditions, but the variation of p for those same poling conditions is not very great (factor of 1.3). In fact, the samples poled above T_c (08576-01, 02, 03) and at the same field are equal to within experimental accuracy. These data clearly show that the poling with regard to the pyroelectric coefficient can take place fairly well at low temperatures and fields, although high temperatures and fields give a definite advantage. This is contrasted to the $\tan\delta$, which must have high temperature and fields to give optimum results.

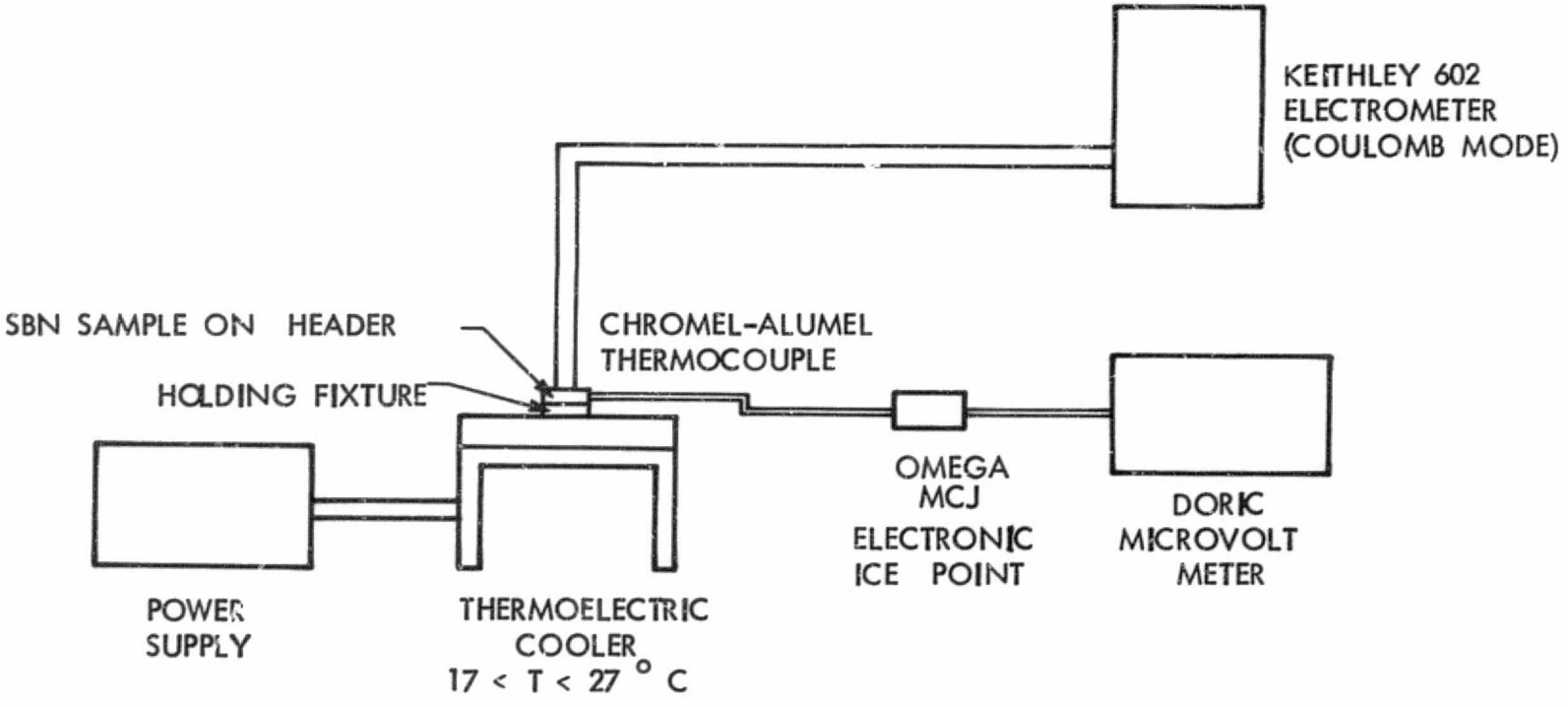

Figure 28 PYROELECTRIC COEFFICIENT MEASUREMENT APPARATUS

Table 6

PYROELECTRIC COEFFICIENT SUMMARY

Ingot	Time (hrs)	Temp. (°C)	Field (V/μm)	$p(\frac{coul}{cm^2\ °C})$
061176-H1	6	145	2.3	3.5×10^{-8}
080576-01	0.88	150	1.4	3.2×10^{-8}
080576-02	5.5	140	1.4	3.1×10^{-8}
080576-03	2	150	1.4	2.8×10^{-8}
080576-04	16.2	23	2	2.5×10^{-8}
082476-01	0.66	145	2.4	3.3×10^{-8}
082476-02	0.05	22	0.3	2×10^{-8}
080376-02	30	150	2	$\sim 5 \times 10^{-8}$

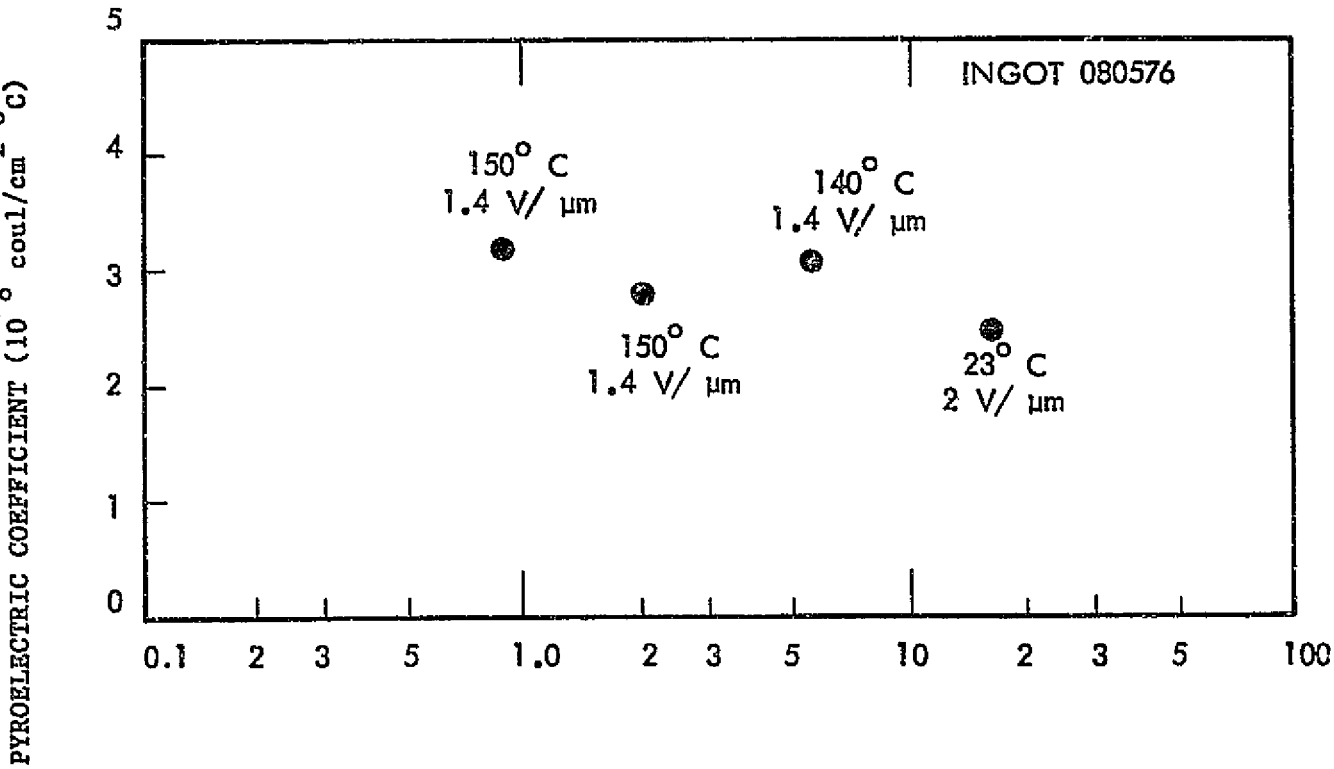

Figure 29 PYROELECTRIC COEFFICIENT VERSUS POLING TIME

5.4 DIELECTRIC PROPERTIES

The D* of a pyroelectric detector is directly proportional to $1/\sqrt{\epsilon_r}$, where ϵ_r is the real part of the dielectric constant. Therefore, a reduction in ϵ_r will produce an increase in D*. When SBN is poled, the ϵ_r is reduced. A reduction factor, given by $R = \frac{\epsilon_r \text{ (Final)}}{\epsilon_r \text{ (Initial)}}$ will be defined. Generally, R = 0.5. This reduction is an indication of the degree of poling. From recent poling experiments, the values of R were in the range $0.35 < R < 0.55$, at 1 kHz measuring frequency. Some representative data are summarized in Table 7.

This reduction in dielectric constant was seen to occur very quickly, at low field, and at room temperature. Specifically, when 0.3 V/ μm was applied to a sample, the capacitance was observed as the poling was taking place. A reduction of R = 0.57 occured in approximately 3 minutes. This value was approached asymptotically, and continued application of the field resulted in no noticeable change in ϵ_r. The smaller values of R occurred for higher fields, higher temperatures, and longer times. These conditions help to completely align all the dipoles in the sample. This, again, is the objective of the poling procedure.

Table 7

VALUES OF R FOR VARIOUS INGOTS & POLING CONDITIONS

$$R = \frac{\epsilon \text{ (Final)}}{\epsilon \text{ (Initial)}}$$

Ingot	Time (hours)	Temperature (°C)	Field (V/μm)	R (1 KHz)
061176-H1	6	145	2.3	0.49
061176-01	65	154	2.3	0.48
080376-01	113	144	3	0.49
080376-02	30	150	2	0.54
080576-01	0.88	150	1.4	0.47
080576-02 ,	5.5	140	1.4	0.41
080576-03	2	150	1.4	0.50
080576-04	16.2	23	2	0.54
080576-05	4	150	2	0.39 +
082076-00	0.66	150	5	0.58 +
082076-01	26.5	145	3	0.50
082076-02				Lost in Power Failure
082476-01	0.66	145	2.4	0.55
082476-02	0.05	22	0.3	0.57
082576-01	24.6	146	3	0.38

SECTION 6
DEVICE PERFORMANCE

In this section the equations which give an approximation to the performance of a pyroelectric detector are presented. The experimental behavior of some detectors are then compared to the theory, and deviations analyzed.

The detector limited D* of the pyroelectric detector is given by:

$$D^* = \frac{\eta\ p}{C\rho\ (8\pi\ KT\ \varepsilon_r \varepsilon_o\ \tan\delta_{fd})^{1/2}}\ T_r \qquad (13)$$

Here:

p = pyroelectric coefficient $\left(\frac{coul}{cm^2\ ^oC}\right)$

η = front surface emissivity

$C\rho$ = detector volume specific heat ($J/cm^3\ ^oC$)

ε = detector relative permittivity

$\tan\delta$ = detector dielectric loss tangent

k = Boltzmann's constant ($1.38 \times 10^{-23}\ J/^oK$)

T = absolute temperature (K)

ε_o = permittivity of free space (8.854×10^{-14} frad/cm)

d = detector thickness (cm)

f = modulation frequency (Hz)

T_r = thermal degradation factor

Equation 13 describes a special case, valid only when the detector noise is greater than the other noise sources.

The voltage responsivity of a pyroelectric detector is given by:

$$R_v = \frac{\eta p}{c\rho d\omega C_d} = \frac{\eta p}{2\pi c \rho \varepsilon_o \varepsilon_r A f} \qquad (14)$$

The noise sources in a pyroelectric detector circuit can be grouped into two classes: 1) noise due to the detector and its mounting, and 2) noise due to the associate matching and amplifying circuitry.

6.1 NOISE SOURCES

Noises of a pyroelectric detector/preamplifier assembly arise from a number of sources. These sources can be represented by the following equation:

$$I_N^2 = i_T^2 + i_d^2 + i_c^2 + i_a^2 + i_{R_n}^2 \qquad (15)$$

where

i_T = temperature fluctuation noise

i_d = detector thermal noise

i_c = amplifier load resistance noise

i_a = amplifier current noise

i_{R_n} = amplifier voltage noise

6.1.1 Temperature Fluctuation Noise

The temperature fluctuation noise represents the ultimate limit to performance of a pyroelectric detector. When a small body is in thermal equilibrium of its surroundings at a temperature T, via a thermal conductance g, the main power flow between the body and its surroundings is zero. However, it will have a fluctuation spectrum with a rms value.[3]

$$\Delta W_T = (4\ KT^2\ g\ A)^{1/2} \tag{16}$$

where g A is the thermal conductance away from the detector by all mechanisms.

The noise due to the thermal fluctuations are:

$$i_T^{\ 2} = R_i^{\ 2}\ 4\ KT^2\ g\ A \tag{17}$$

where R_i is the current responsivity of the detector. The minimum temperature fluctuation noise occurs when g is dominated by radiative exchange alone; heat transfer by conduction to the detector mount or through any gas used for backfill would increase the temperature fluctuation noise by increasing g. The thermal fluctuation noise due to radiation and conduction will be calculated separately and be denoted i_r and i_t respectively.

6.1.2 Detector Thermal Noise

There will be Johnson noise associated with any element with resistance given by:

$$i_d^{\ 2} = \frac{4KT}{R} = 4\ KT\ \ g_d \tag{18}$$

There are two sources of conductance in a pyroelectric (a) the dielectric loss with conductance $g_d = \omega C_d \tan\delta$, and (b) any leakage conductance around the device. In present devices the leakage conductance is sufficiently low that it may be neglected in comparison with the dielectric loss. The

dielectric loss is due to a number of factors, some associated with material defects and some with device fabrication.

6.1.3 Input Circuit Thermal Noise

The input circuit utilizes a load resistor R_L in order to operate the JFET amplifier in a stable configuration. The load resistor is normally chosen to be sufficiently high ($10^{12}\Omega$) that it does not contribute excess noise. The noise is given by the Johnson noise of the load resistor R_L.

$$i_c^2 = 4\ KT/R_L \tag{19}$$

6.1.4 Amplifier Current Noise

Any circuit can be represented by a combination of a voltage generator in series with the input and a current generator in parallel of the input. Either of these noise sources may dominate the total noise depending on the impedance of the detector and amplifier.

The preamplifier usually consists of a low-noise JFET and associated biasing circuitry. All FET's have gate leakage current I_g associated with them; this leakage current is a source of shot noise i_a where:

$$i_a^2 = 2\ q\ I_g \tag{20}$$

where q is the electronic charge. Different types of JFETs show wide variations in I_g; values for the present state-of-the-art is about 0.2 pA.

6.1.5 Amplifier Voltage Noise

The amplifier voltage noise is specified either in terms of v_n or an equivalent noise resistance R_n. The noise is given by:

$$i_{n}^{2} = 4\,KT\,R_{n}\left[(g_c + g_d)^2 + \omega^2(C_d + C_a)^2\right] = v_n^2\,Y^2 \qquad (21)$$

where v_n is the amplifier noise voltage and $g_c + g_d$ and $C_d + C_a$ are the total conductance and capacitance of the input circuit, respectively. Typical JFETs have $v_n = 10\ nV/\sqrt{Hz}$.

6.2 DEVICE ANALYSIS

In this section the six noise sources for each detector will be computed and compared to the experimentally observed noise. The experimentally observed responsivity will then be used with the theoretical noise to determine a quasitheoretical value for the D*, and this will be compared to experimentally determined values.

6.3 NOISE ANALYSIS

SBN-3

The calculation parameters for the noise sources are shown in Table 8. In this and all other cases in this section, the value for the pyroelectric coefficient was determined from the observed voltage responsivity at a point well above the thermal rolloff frequency. The value for average front surface emissivity (η) was taken to be $\eta_c = 0.95$, as determined from spectral reflectance data (Figure 23). Using the noise values determined from Table 8, the plot of the theoretical and experimental noise versus frequency is shown in Figure 30. In an attempt to determine a best-fit condition, the theoretical noise was calculated for $f_o = 3$ Hz and $\tan\delta = 0.028$. These results are plotted in Figure 31, and show that an effective $\tan\delta = 0.028$ gives good agreement with the experimentally observed data. The D* values obtained from the Figure 30 and Figure 31 noise data are shown in Figures 32 and 33, respectively.

SBN-6

The noise calculation parameters for SBN-6 are shown in Table 9, and the resulting theoretical-experimental noise is plotted in Figure 34.

Table 8

NOISE CALCULATION PARAMETERS, CALCULATED AND EXPERIMENTAL NOISE FOR SBN-3

SBN-3

$A = 3.8 \times 10^{-3} cm^2$	$C = 67pF$	$R_L = 1 \times 10^{11}$ ohms
$d = 15 \mu m$	$\tan \delta = 0.013$	$i_g = 0.1$ pA
$f_o = 0.9$ Hz	$p = 3.5 \times 10^{-8} \frac{coul}{cm^2 °C}$	$T = 293K$

	Theoretical Noise ($V/\sqrt{Hz}$)		Experimental Noise
Freq (Hz)	$V_n(f_o=0.9Hz, \tan\delta=0.013)$	$V_n(f_o=3Hz, \tan\delta=0.028)$	$V_n(V/\sqrt{Hz})$
1.2	1.1×10^{-6}	1.25×10^{-6}	1.4×10^{-6}
2.4	6.3×10^{-7}	7.1×10^{-7}	1.2×10^{-6}
6	3.3×10^{-7}	4.6×10^{-7}	6.2×10^{-7}
12	2.2×10^{-7}	3.05×10^{-7}	3.5×10^{-7}
24	1.5×10^{-7}	2.1×10^{-7}	2.1×10^{-7}
60	9.1×10^{-8}	1.3×10^{-7}	1.1×10^{-7}
120	6.4×10^{-8}	9.2×10^{-8}	9×10^{-8}
240	4.6×10^{-8}	6.5×10^{-8}	4.3×10^{-8}

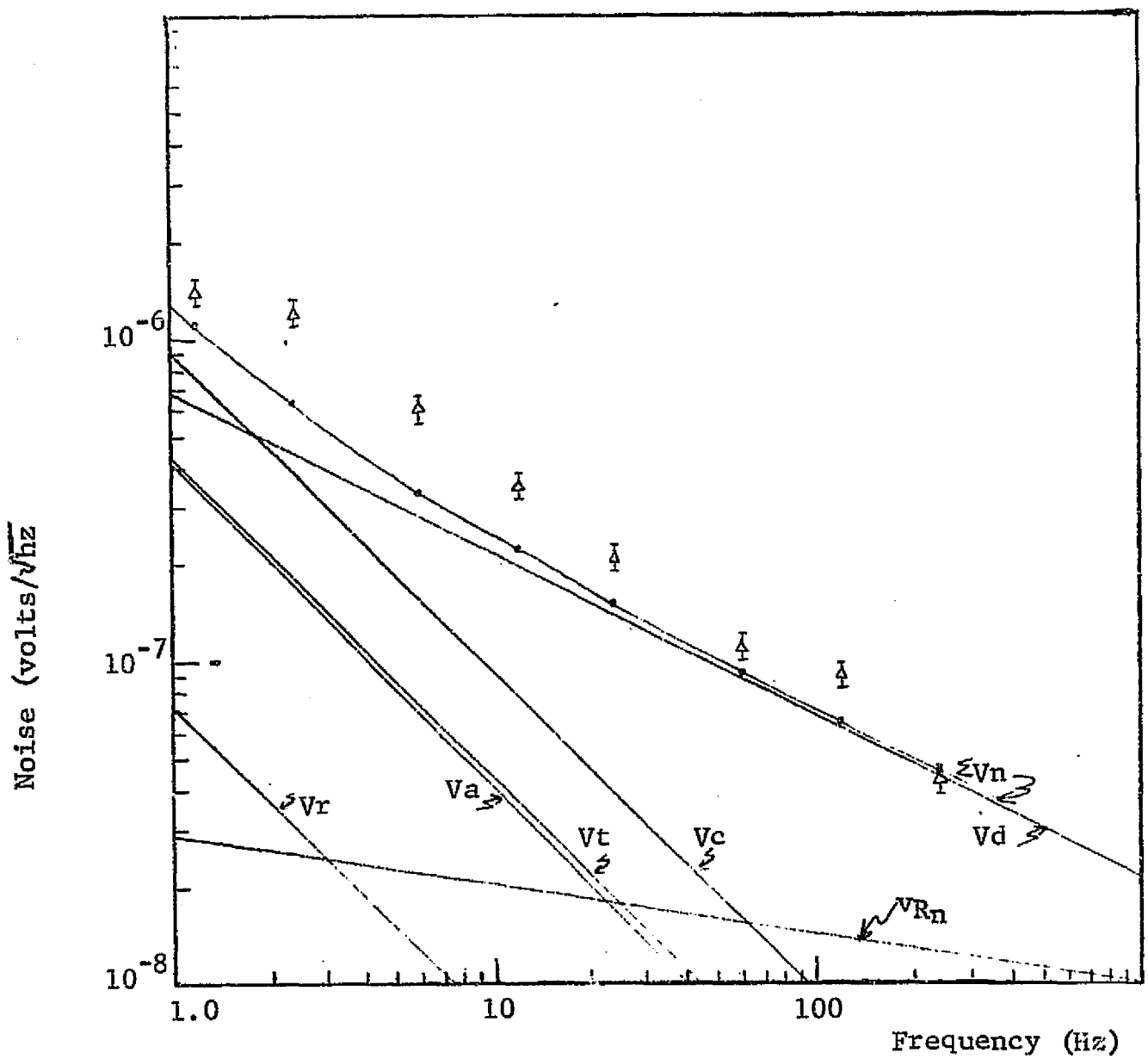

Figure 30 COMPARISON OF THEORETICAL AND EXPERIMENTAL NOISE OF SBN-3
f_o = 0.9 Hz, $\tan\delta$ = 0.013.

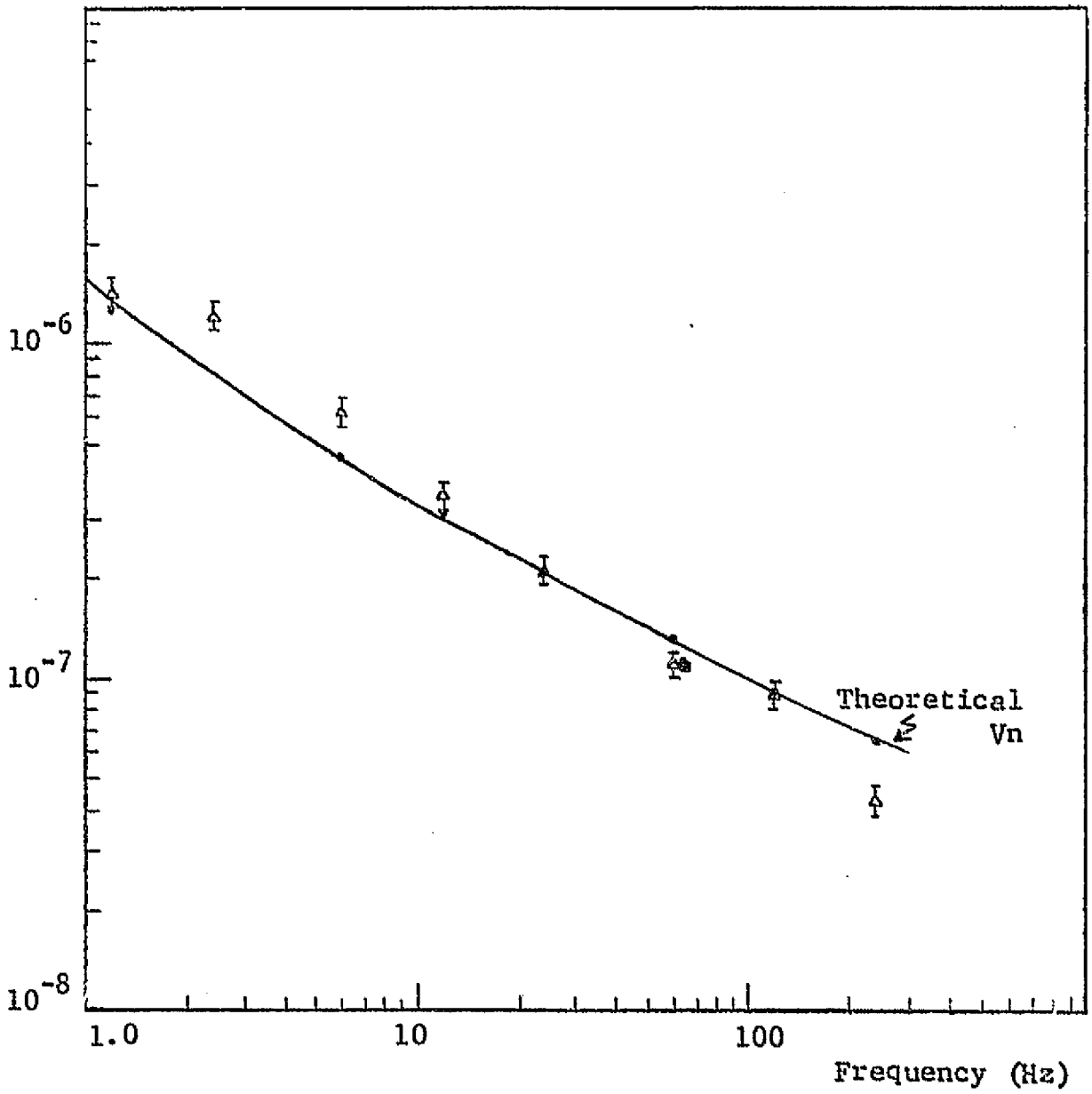

Figure 31 COMPARISON OF THEORETICAL AND EXPERIMENTAL NOISE OF SBN-3; f_o = 3 Hz, $\tan\delta$ = 0.028

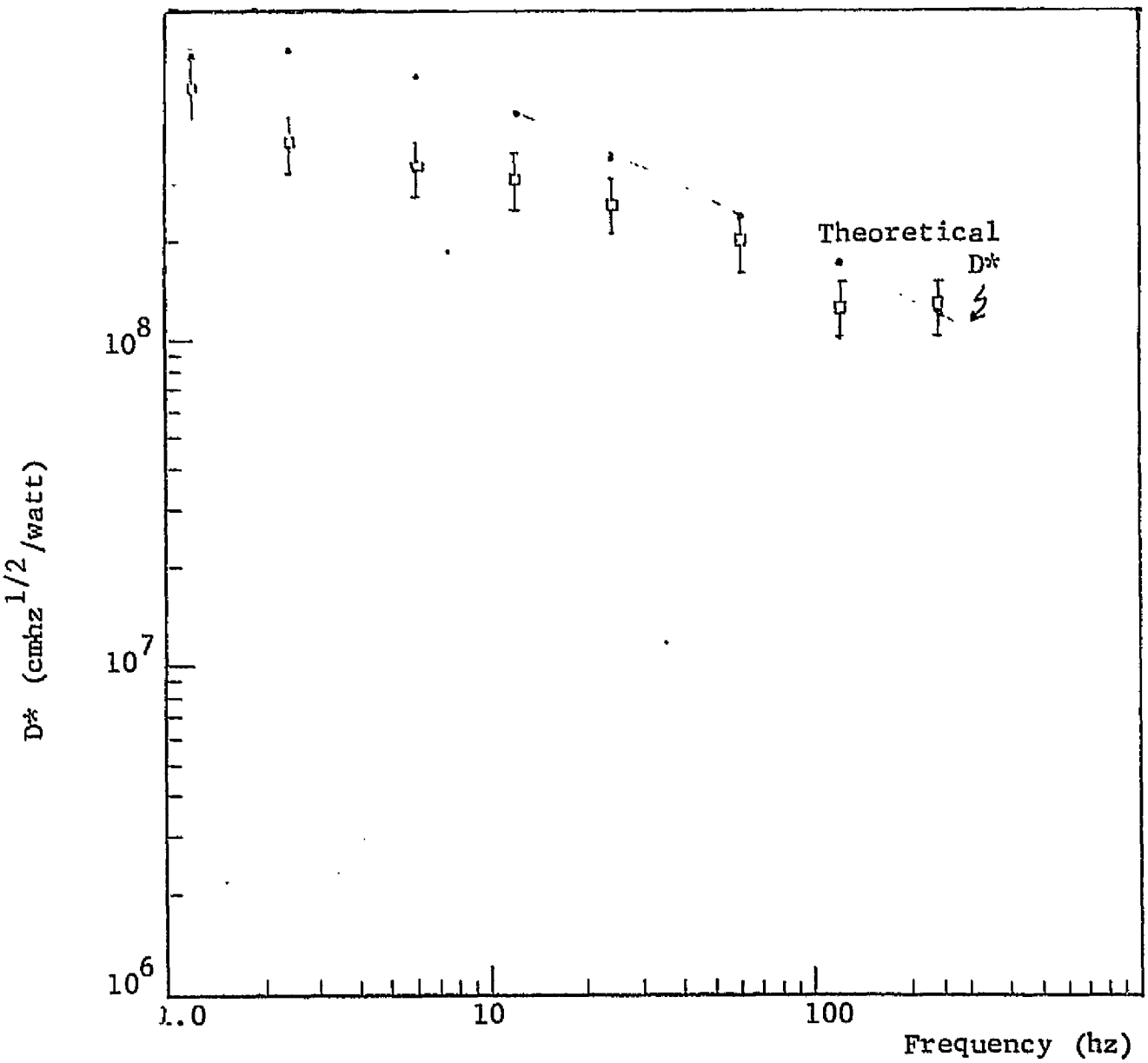

Figure 32 COMPARISON OF THEORETICAL AND EXPERIMENTAL D* OF SBN-3, f_o - 0.9 Hz, $\tan\delta$ = 0.13 IN NOISE CALCULATIONS.

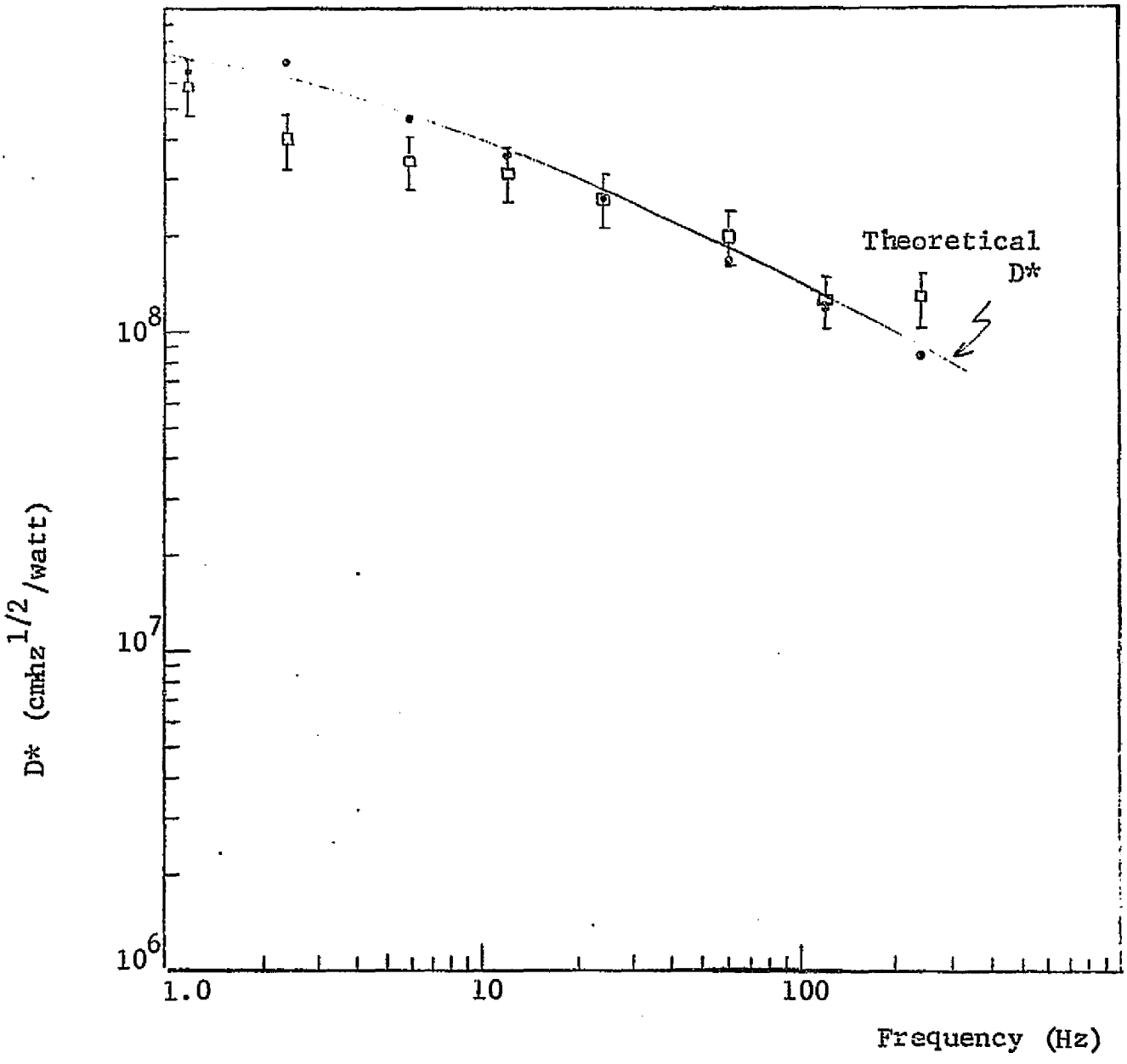

Figure 33 COMPARISON OF THEORETICAL AND EXPERIMENTAL D* OF SBN-3; f_o = 3 Hz, $\tan\delta$ = 0.028 IN NOISE CALCULATIONS.

Table 9

NOISE CALCULATION PARAMETERS, CALCULATED AND EXPERIMENTAL NOISE FOR SBN-6

SBN-6

$A = 2.88 \times 10^{-3} cm^2$	$C = 36pF$	$R_L = 1 \times 10^{11} r\Omega$
$d = 25 \mu m$	$\tan\delta = 0.003$	$i_g = 0.1$ pA
$f_o = 1.4$ Hz	$p = 4.3 \times 10^{-8} \frac{coul}{cm^2 °C}$	$T = 293K$

	Theoretical Noise ($V/\sqrt{Hz}$)		Experimental Noise
Freq (Hz)	$V_n(f_o=1.4Hz, \tan\delta=0.003)$	$V_n(f_o=6Hz, \tan\delta=0.011)$	V_n ($V/\sqrt{Hz}$)
1.2	1.6×10^{-6}	1.7×10^{-6}	1.5×10^{-6}
2.4	8.4×10^{-7}	9.5×10^{-7}	1.2×10^{-6}
6	3.6×10^{-7}	4.9×10^{-7}	4.9×10^{-7}
12	2×10^{-7}	3×10^{-7}	2.9×10^{-7}
24	1.2×10^{-7}	1.9×10^{-7}	1.7×10^{-7}
60	6.5×10^{-8}	1.14×10^{-7}	1.1×10^{-7}
120	4.4×10^{-8}	7.9×10^{-8}	6.1×10^{-8}
240	3.1×10^{-8}	5.6×10^{-8}	4.3×10^{-8}

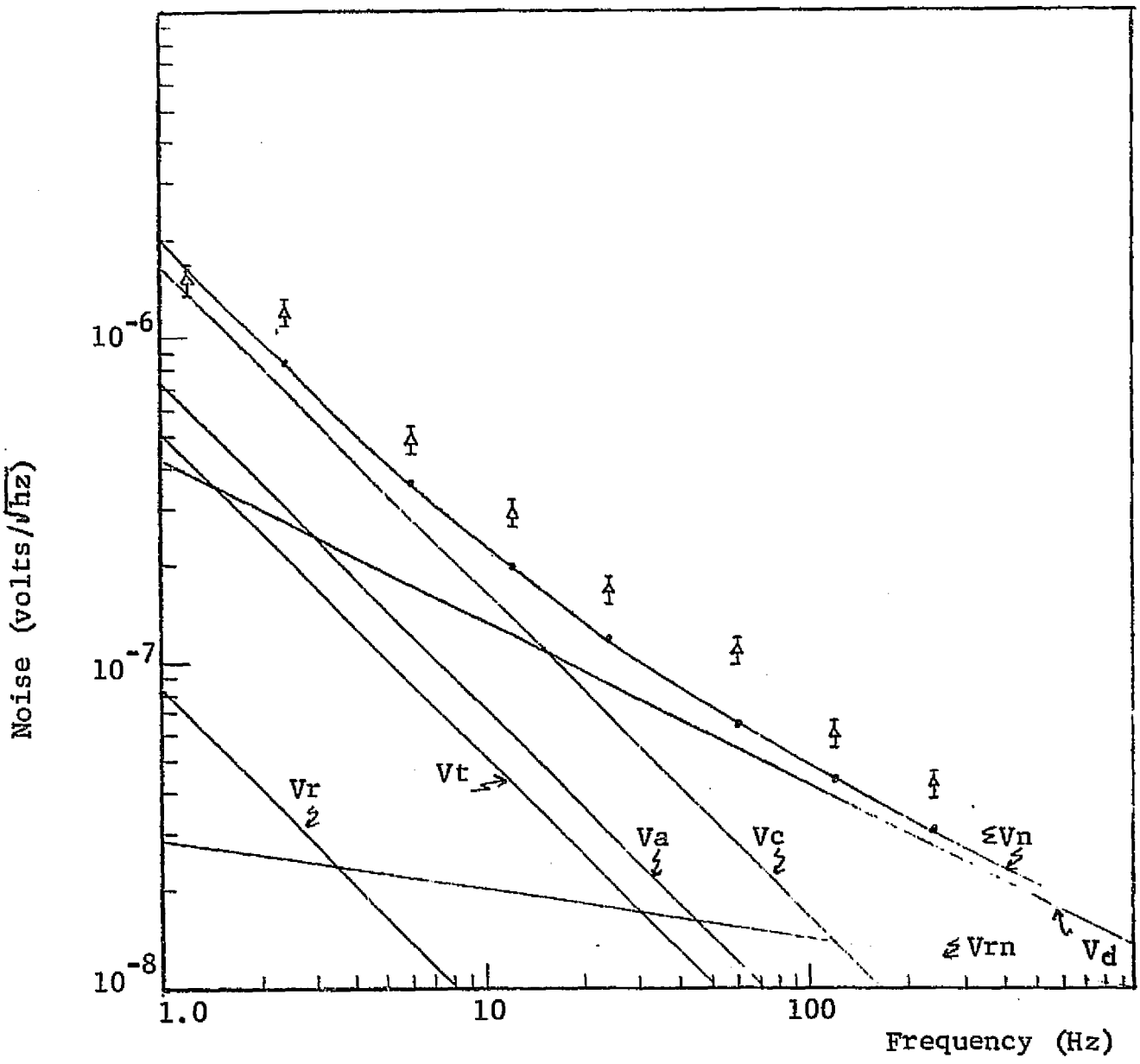

Figure 34 COMPARISON OF THEORETICAL AND EXPERIMENTAL NOISE OF SBN-6; f_o = 1.4 Hz, $\tan\delta$ = 0.003.

A best-fit case plotted in Figure 35 is arrived at by using an effective of $\tan \delta = 0.011$, with $f_o = 6$ Hz. The D* values corresponding to the theoretical noise in Figures 34 and 35 are shown in Figures 36 and 37, respectively.

SBN-8

The calculation parameters for the noise of SBN-8 are shown in Table 10. The individual noise sources, the total theoretical noise and the experimental noise are plotted in Figure 38. Figure 39 shows the agreement when $f_o = 6$ Hz and $\tan\delta = 0.003$. The D*'s computed from the theoretical noise in Figures 38 and 39 are shown in Figures 40 and 41, respectively.

SBN-12

Table 11 lists the calculation parameters for the theoretical noise of SBN-12, and the theoretical and experimental noise are plotted in Figure 42. A better theoretical fit to the experimental data is obtained if values of $\tan \delta = 0.0063$ and the thermal rolloff frequency $f_o = 6$ Hz are used. The effect of these adjustments is plotted in Figure 43, along with the experimental noise. The D* data corresponding to the noise plotted in Figures 42 and 43 are plotted in Figures 44 and 45, respectively.

SBN-13

SBN-13 was not enclosed in a vacuum dewar, and hence was subject to airborne microphonics. This resulted in much excess noise over the frequency range from 1 Hz - 60 Hz. The calculation parameters for SBN-13 are listed in Table 12, and the results of the calculations are plotted in Figure 46, along with the experimental noise. The D*'s from the experimental and theoretical noise are plotted in Figure 47.

080376-02-1

Shown in Table 13 are the noise calculation parameters for 080376-02-1. The theory versus experiment is plotted in Figure 48 and by using $f_o =$

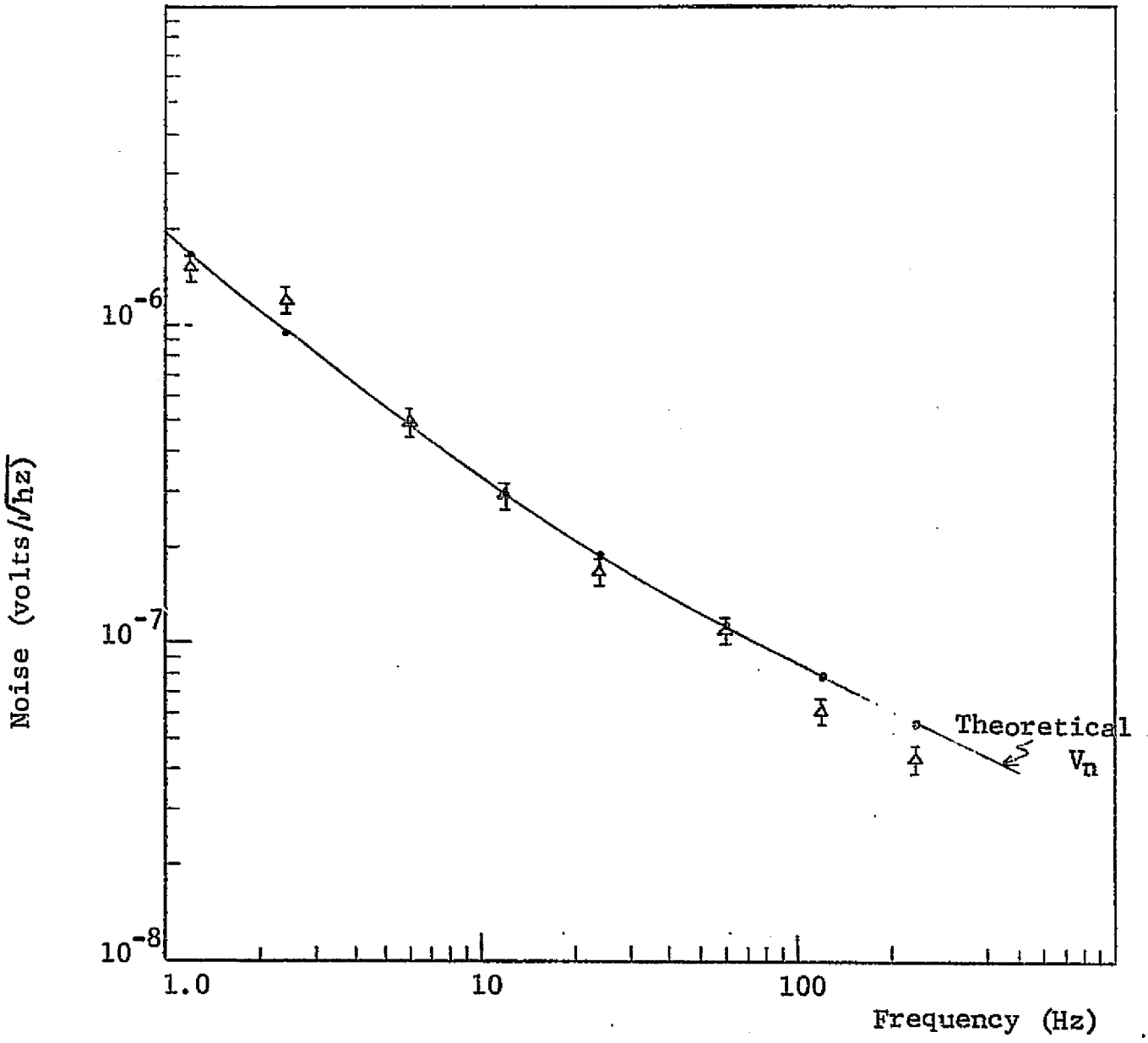

Figure 35 COMPARISON OF THEORETICAL AND EXPERIMENTAL NOISE OF SBN-6; f_o = 6 Hz, $\tan\delta$ = 0.011.

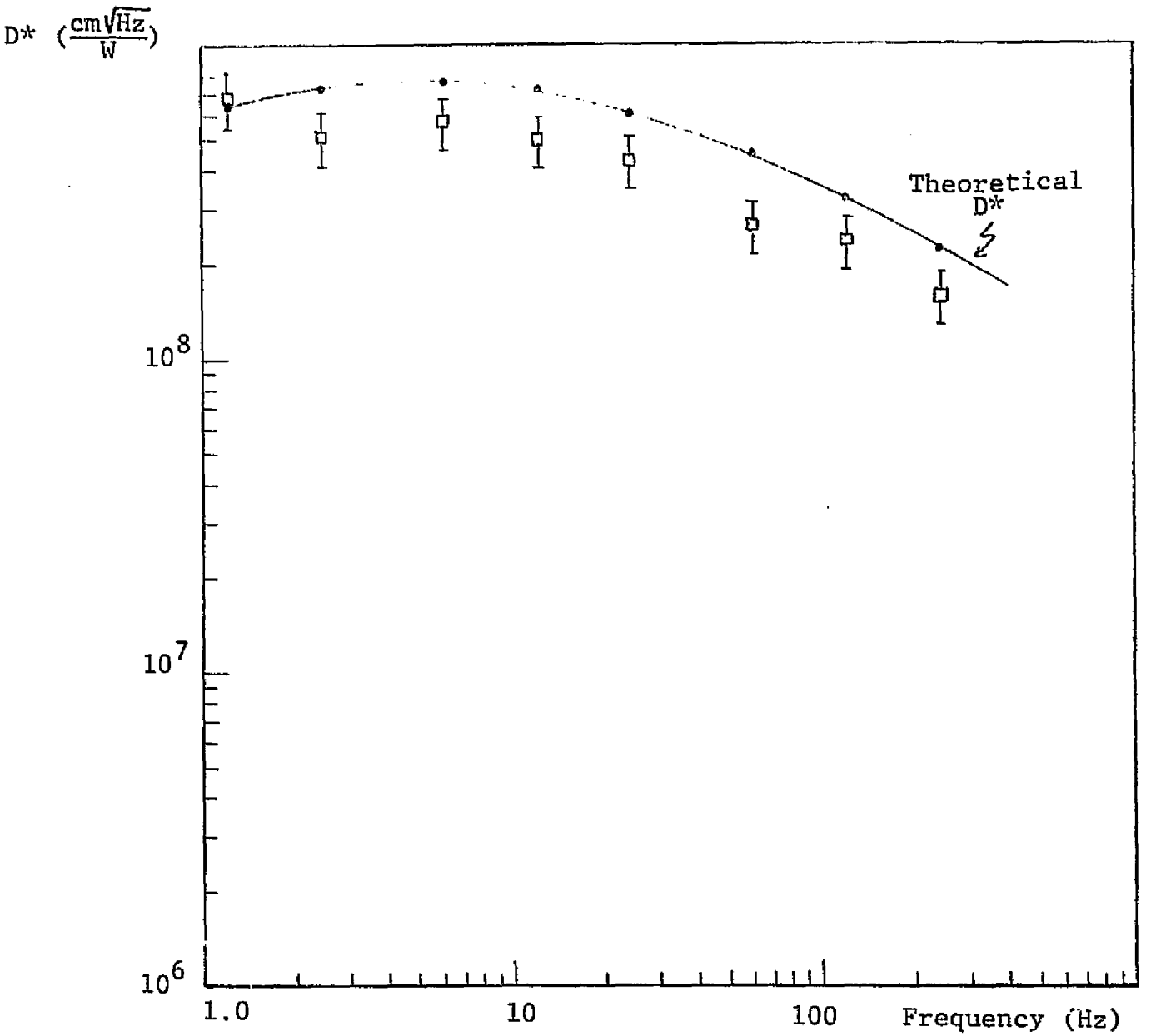

Figure 36 COMPARISON OF THEORETICAL AND EXPERIMENTAL D* OF SBN-6; f_o = 1.4 Hz, tan δ = 0.003 IN NOISE CALCULATIONS.

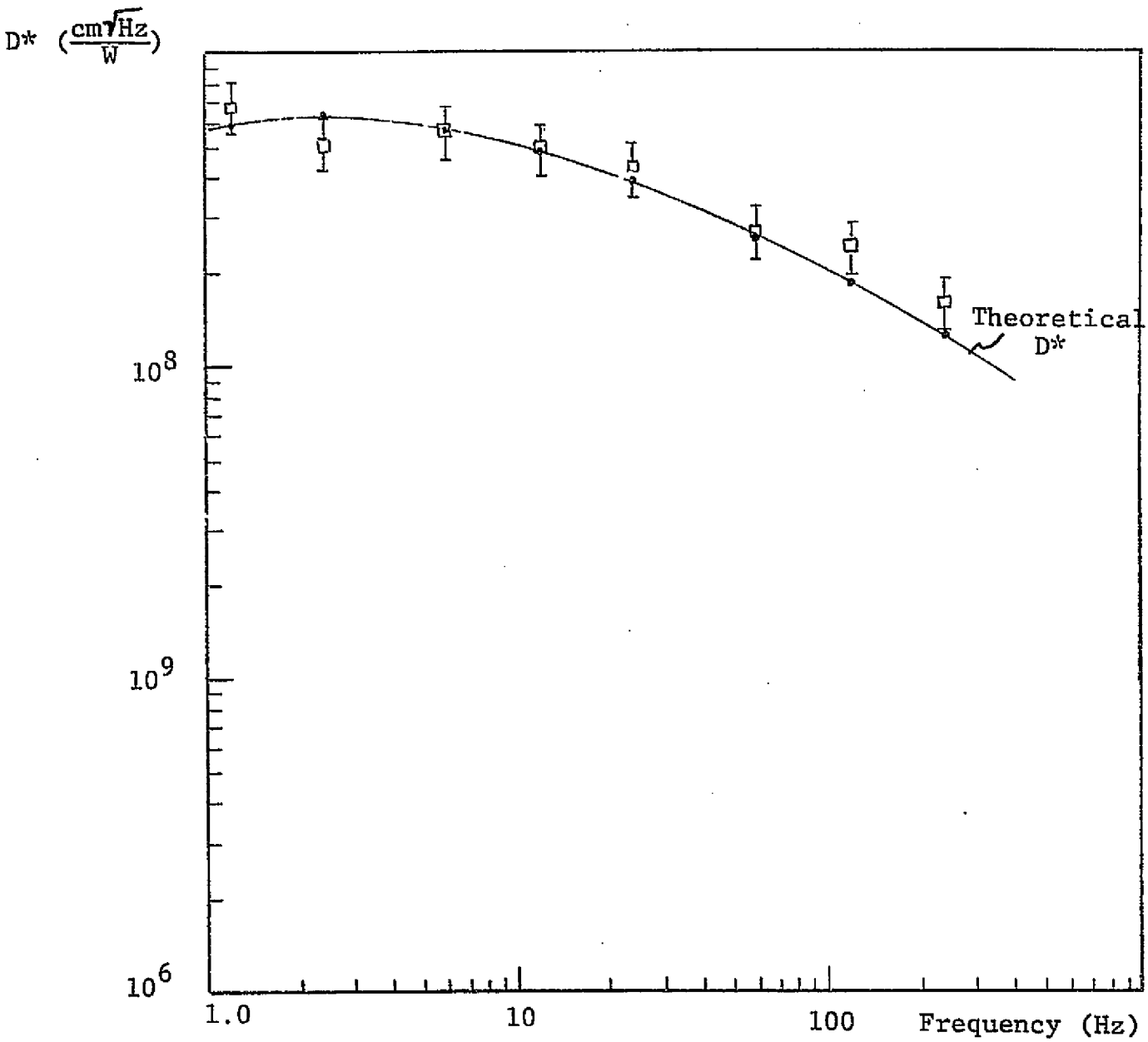

Figure 37 COMPARISON OF THEORETICAL AND EXPERIMENTAL D* OF SBN-6; f_o = 6 Hz, $\tan\delta$ = 0.011 IN NOISE CALCULATIONS.

Table 10

NOISE CALCULATION PARAMETERS, CALCULATED AND EXPERIMENTAL NOISE FOR SBN-8

SBN-8

$A = 4.52 \times 10^{-3} cm^2$	$C = 71 pF$	$R_L = 1 \times 10^{11}$
$d = 25 \mu m$	$\tan\delta = 0.003$	$i_g = 0.1$ pA
$f_o = 0.7$ Hz	$p = 3.3 \times 10^{-8} \frac{coul}{cm^2 °C}$	$T = 293K$

	Theoretical Noise ($V/\sqrt{Hz}$)		Experimental Noise
Freq (Hz)	$V_n(f_o=0.7Hz, \tan\delta = 0.003)$	$V_n(f_o=6Hz, \tan\delta = 0.003)$	$V_n (V/\sqrt{Hz})$
1.2	8.7×10^{-7}	8.5×10^{-7}	7.7×10^{-7}
2.4	4.6×10^{-7}	4.7×10^{-7}	5.4×10^{-7}
6	2.1×10^{-7}	2.46×10^{-7}	2.6×10^{-7}
12	1.2×10^{-7}	1.4×10^{-7}	1.5×10^{-7}
24	7.9×10^{-8}	8.6×10^{-8}	9×10^{-8}
60	4.7×10^{-8}	4.9×10^{-8}	7.4×10^{-8}
120	3.3×10^{-8}	3.4×10^{-8}	4.4×10^{-8}
240	2.4×10^{-8}	2.45×10^{-8}	2.5×10^{-8}

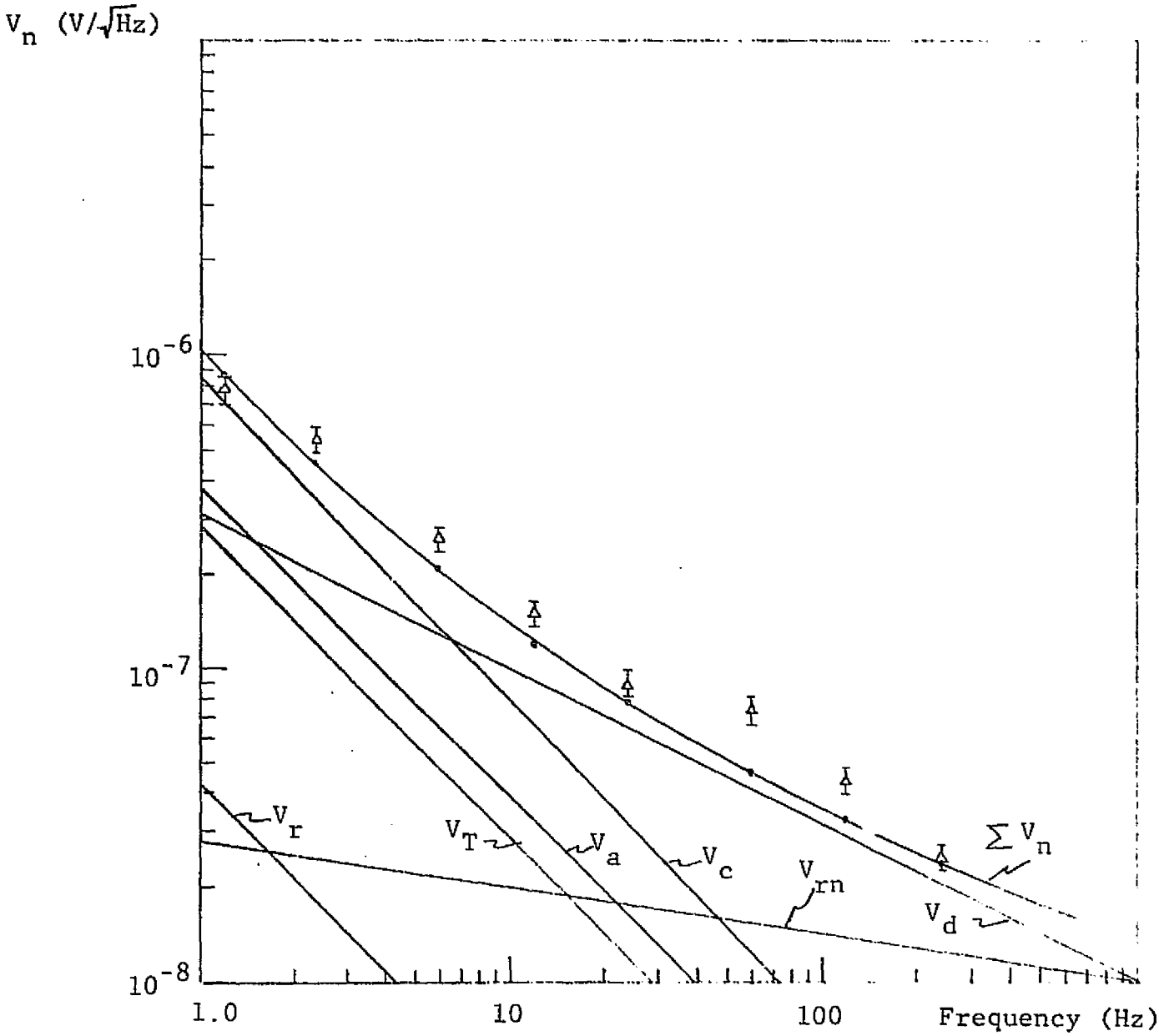

Figure 38 COMPARISON OF THEORETICAL AND EXPERIMENTAL NOISE OF SBN-8; f_o = 0.7 Hz, $\tan\delta$ = 0.003.

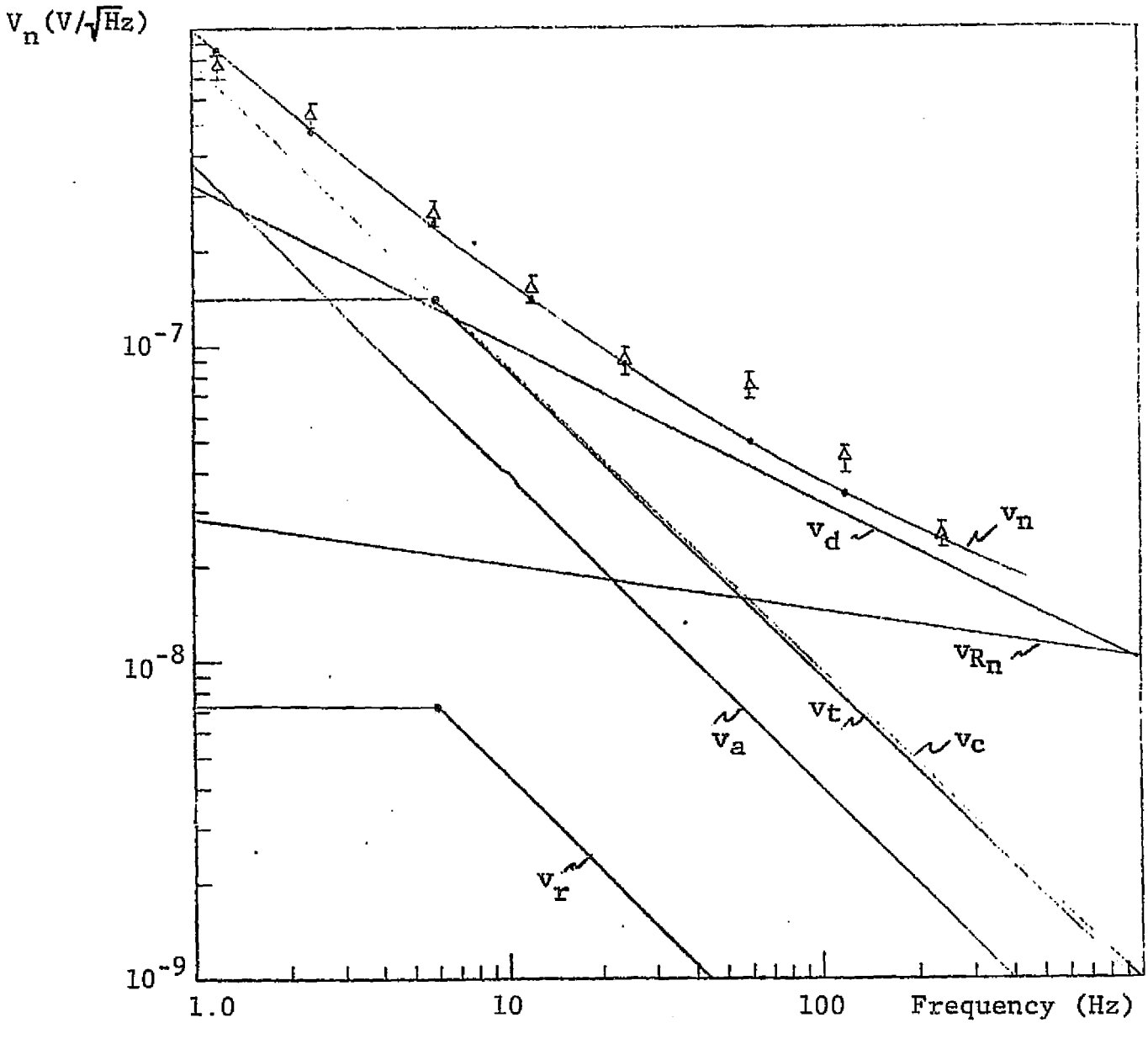

Figure 39 COMPARISON OF THEORETICAL AND EXPERIMENTAL NOISE OF SBN-8; f_o = 6 Hz, $\tan\delta$ = 0.003.

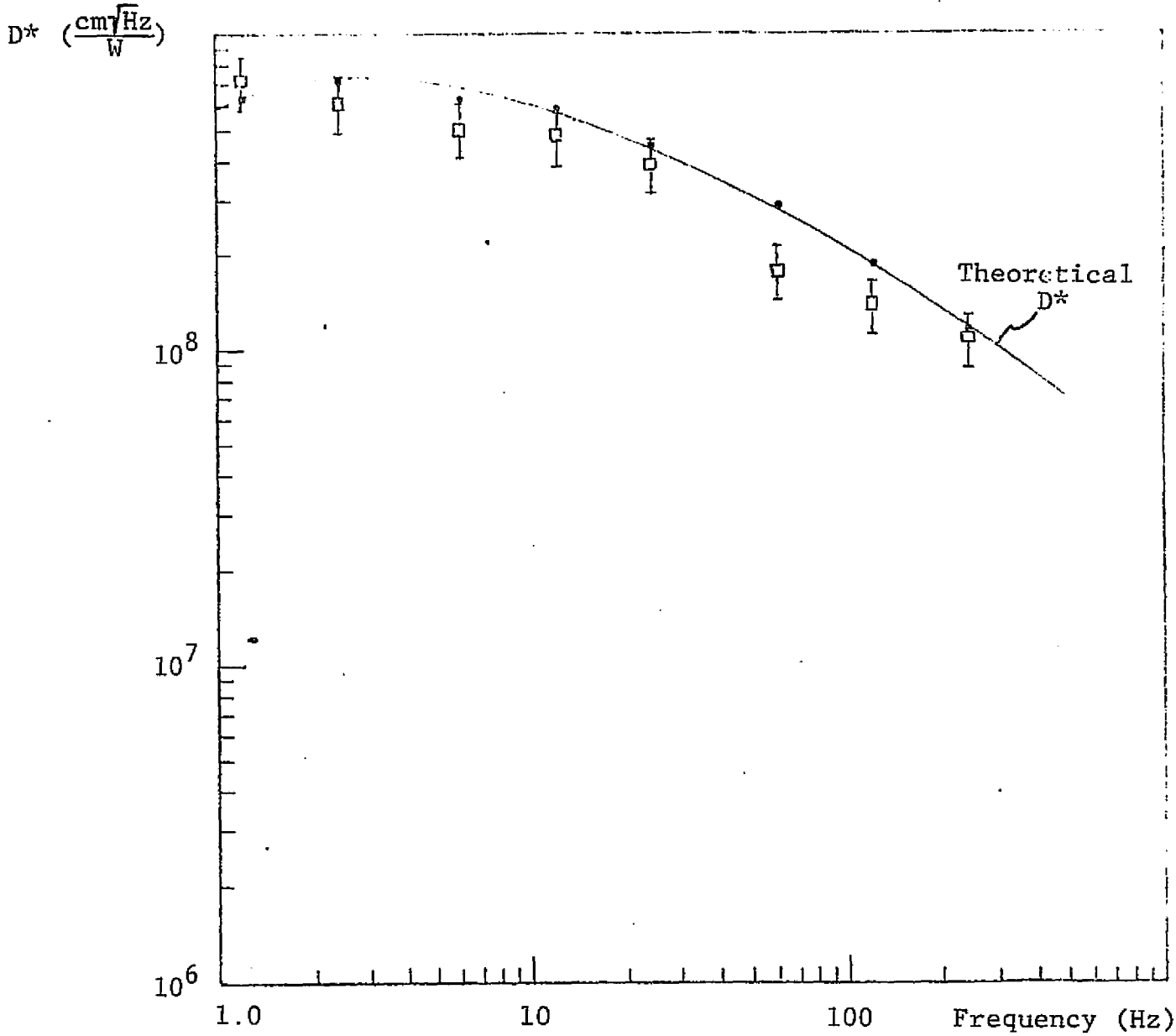

Figure 40 COMPARISON OF THEORETICAL AND EXPERIMENTAL D* OF SBN-8; $f_o = 0.7$, $\tan\delta = 0.003$ IN NOISE CALCULATIONS.

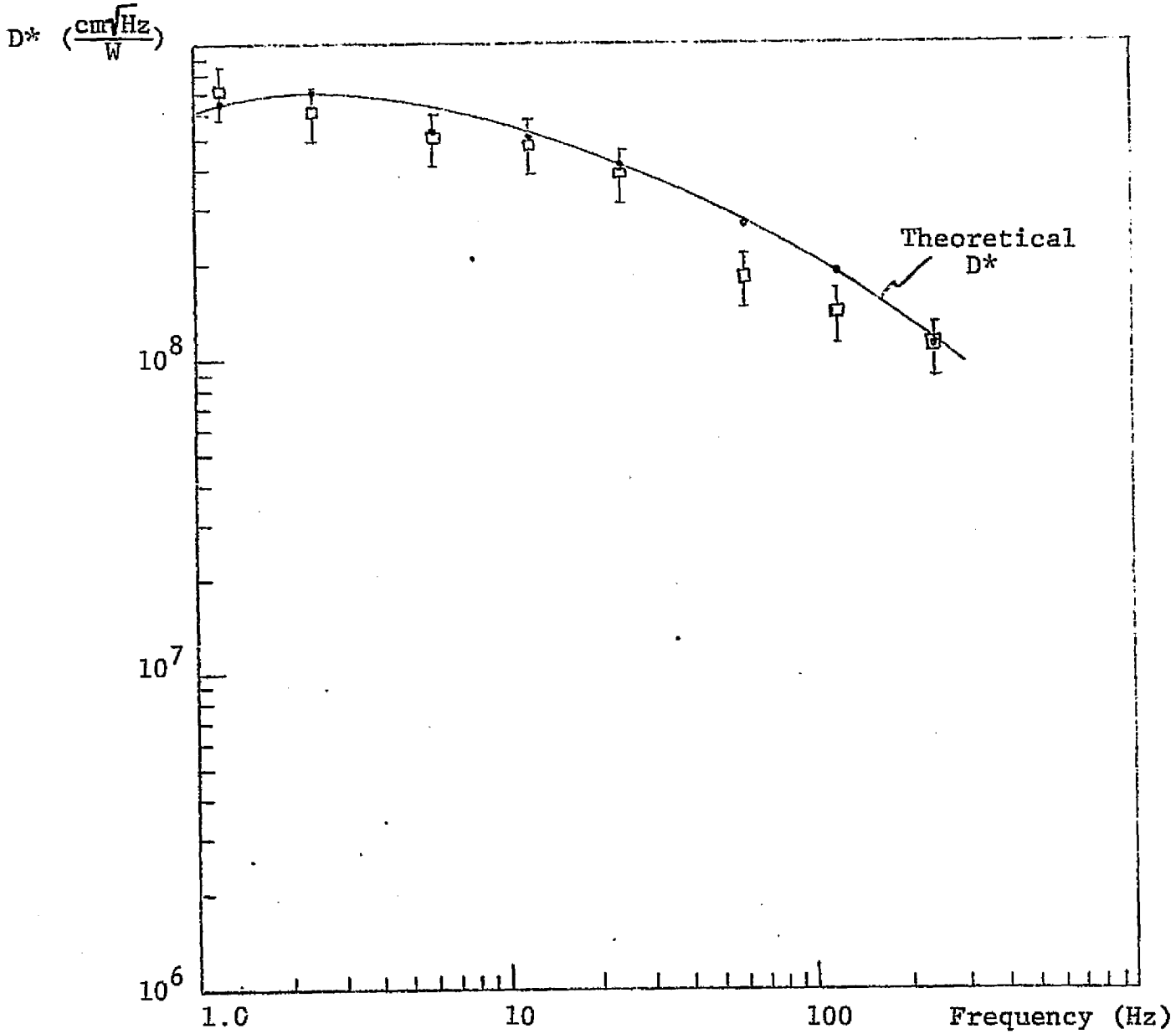

Figure 41 COMPARISON OF THEORETICAL AND EXPERIMENTAL D* OF SBN-8; f_o = 6 Hz, tan δ = 0.003 IN NOISE CALCULATIONS.

Table 11

NOISE CALCULATION PARAMETERS, CALCULATED AND EXPERIMENTAL NOISE FOR SBN-12

SBN-12

$A = 4.13 \times 10^{-3} cm^2$ $C = 50pF$ $R_L = 1 \times 10^{11} \Omega$

$d = 22 \mu m$ $\tan\delta = 0.001$ $i_g = 0.1$ pA

$f_o = 1.2$ Hz $p = 3.9 \times 10^{-8} \frac{coul}{cm^2 °C}$ $T = 293K$

	Theoretical Noise $(V/\sqrt{Hz})$		Experimental Noise
Freq (Hz)	$V_n(f_o=1.2Hz \tan\delta=0.001)$	$Vn(f_o=6Hz, \tan\delta = 0.0063)$	$V_n (V/\sqrt{Hz})$
1.2	1.2×10^{-6}	1.2×10^{-6}	1.1×10^{-6}
2.4	6.2×10^{-7}	6.7×10^{-7}	8.5×10^{-7}
6	2.6×10^{-7}	3.5×10^{-7}	4.1×10^{-7}
12	1.37×10^{-7}	2.1×10^{-7}	2.3×10^{-7}
24	7.7×10^{-8}	1.3×10^{-7}	1.3×10^{-7}
60	4×10^{-8}	7.7×10^{-8}	8.5×10^{-8}
120	2.7×10^{-8}	5.3×10^{-8}	4.3×10^{-8}
240	1.96×10^{-8}	3.8×10^{-8}	1.8×10^{-8}

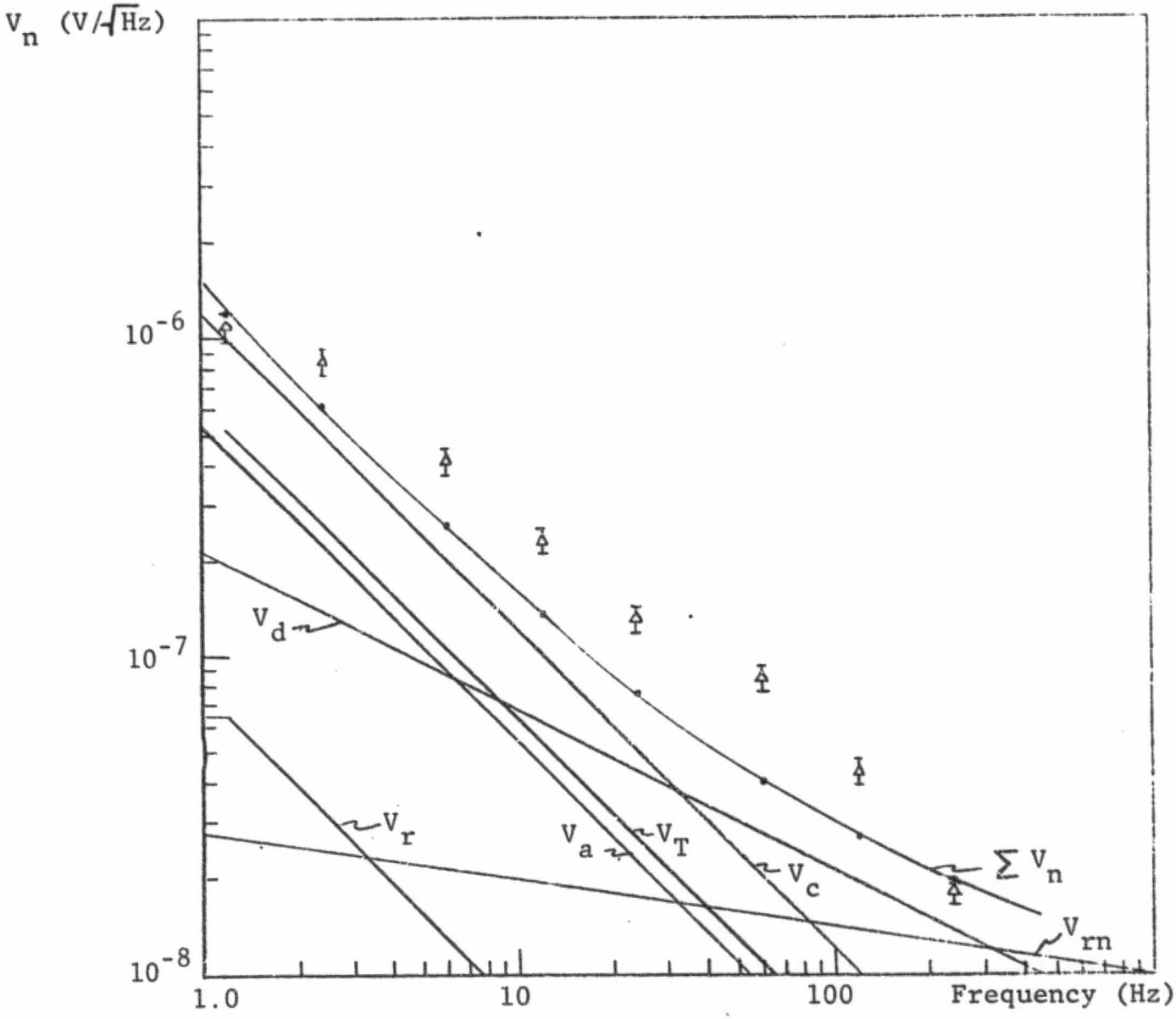

Figure 42 COMPARISON OF THEORETICAL AND EXPERIMENTAL NOISE OF SBN-12, f_o = 1.2 Hz, $\tan\delta$ = 0.001.

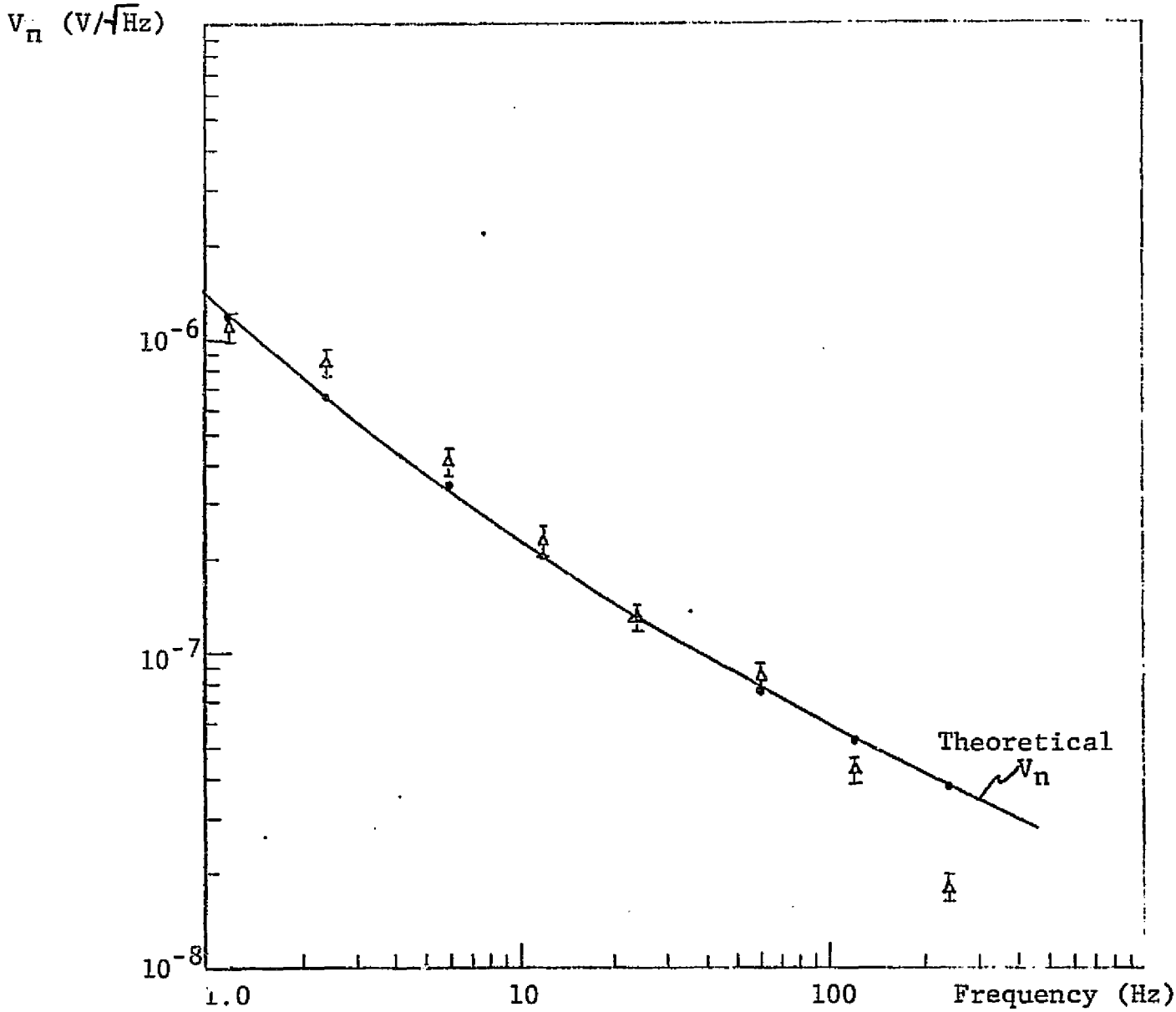

Figure 4: COMPARISON OF THEORETICAL AND EXPERIMENTAL NOISE OF SBN-12; f_c = 6 Hz, $\tan\delta$ = 0.0063.

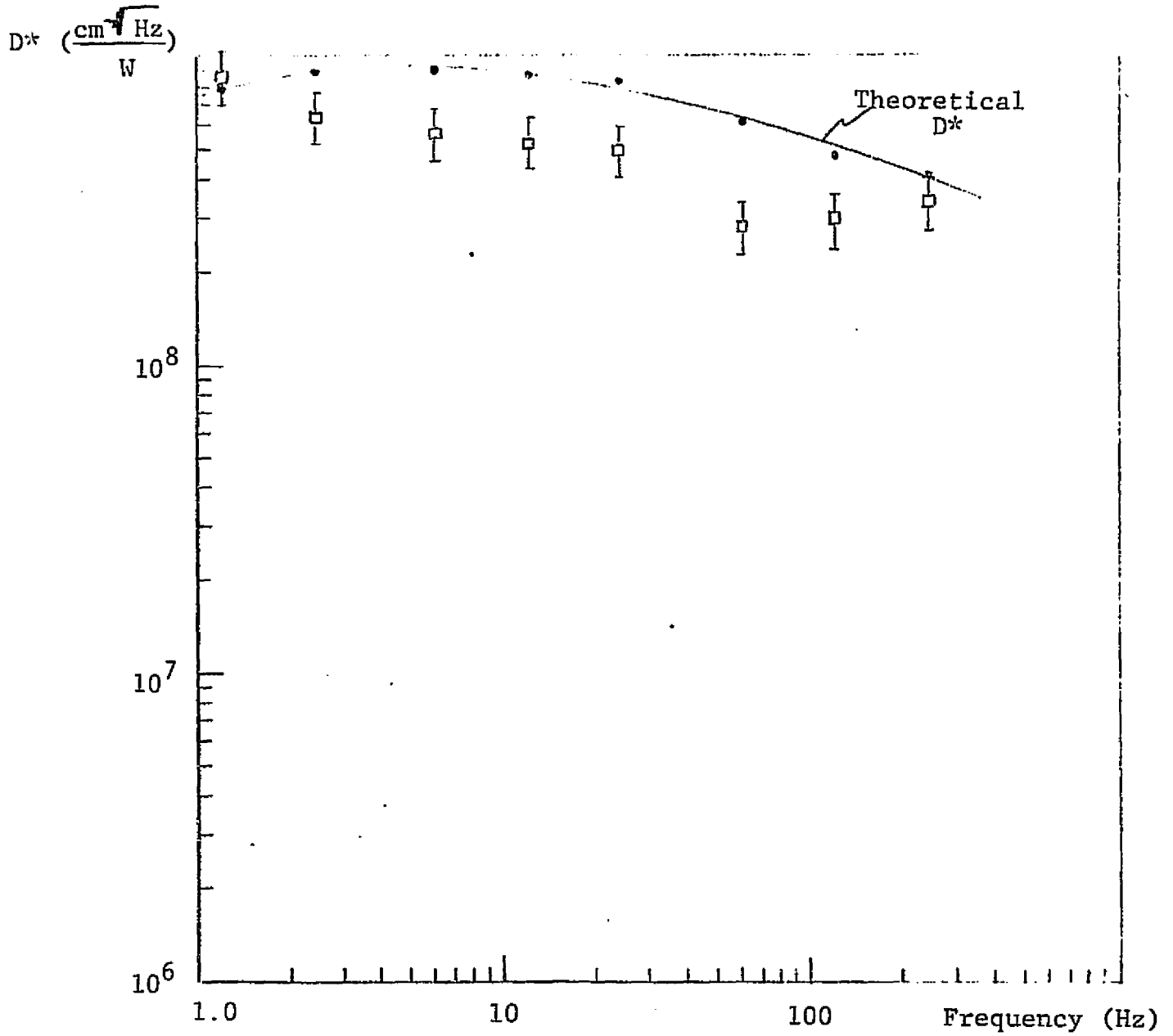

Figure 44 COMPARISON OF THEORETICAL AND EXPERIMENTAL D* OF SBN-12; f_o = 1.2 Hz, $\tan\delta$ = 0.001 IN NOISE CALCULATIONS

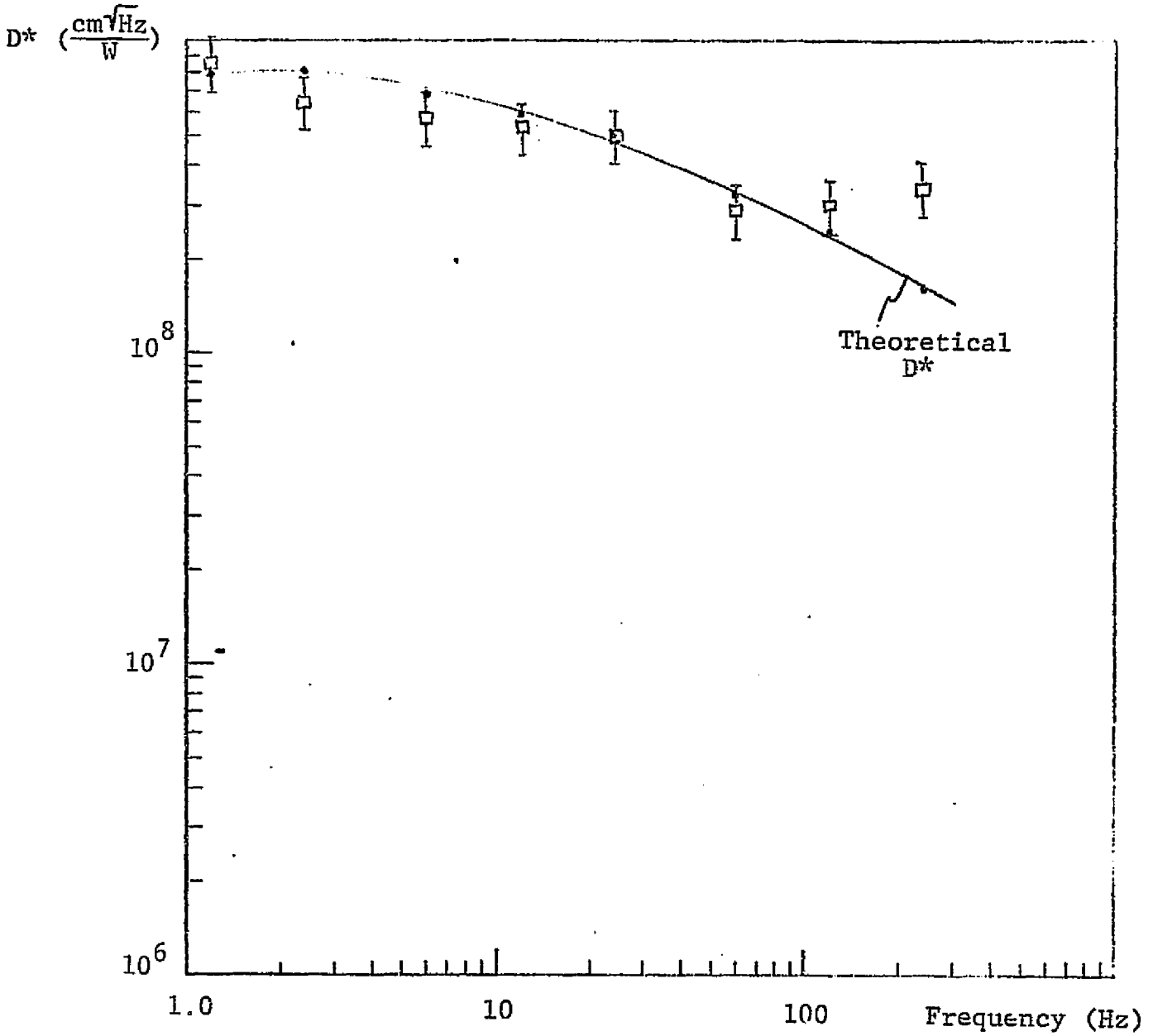

Figure 45 COMPARISON OF THEORETICAL AND EXPERIMENTAL D* OF SBN-12; f_o = 6 Hz, $\tan\delta$ = 0.0063 IN NOISE CALCULATIONS.

Table 12

NOISE CALCULATION PARAMETERS, CALCULATED AND EXPERIMENTAL NOISE FOR SBN-13

SBN-13

$A = 4.58 \times 10^{-3} cm^2$	$C = 59pF$	$R_L = 1 \times 10^{11}$
$d = 22 \mu m$	$\tan \delta = 0.002$	$i_g = 0.1$ pA
$f_o = 2.3$ Hz	$p = 3.3 \times 10^{-8} \frac{coul}{cm^2 °C}$	$T = 293K$

	Theoretical Noise ($V/\sqrt{Hz}$)	Experimental Noise
Freq (Hz)	$V_n(f_o = 2.3$ Hz, tan. $\delta = 0.002)$	$V_n(V/\sqrt{Hz})$
1.2	1×10^{-6}	1.5×10^{-6}
2.4	5.7×10^{-7}	1.17×10^{-6}
6	2.5×10^{-7}	4.2×10^{-7}
12	1.4×10^{-7}	1×10^{-6}
24	8.1×10^{-8}	2×10^{-7}
60	4.5×10^{-8}	1×10^{-7}
120	3.1×10^{-8}	4.3×10^{-8}
240	2.26×10^{-8}	2.8×10^{-8}

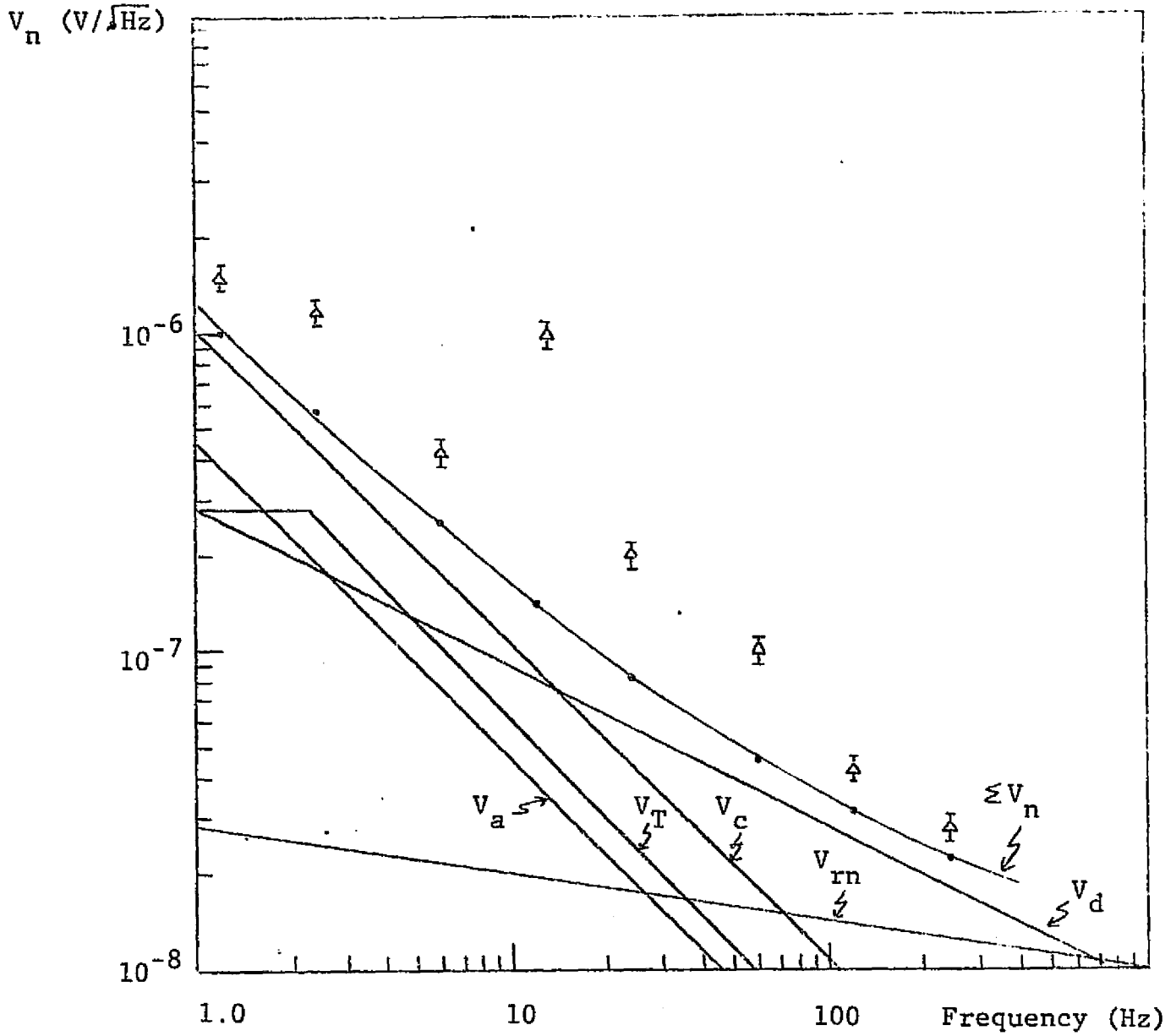

Figure 46 COMPARISON OF THEORETICAL AND EXPERIMENTAL NOISE OF SBN-13; f_o = 2.3 Hz, $\tan\delta$ = 0.002.

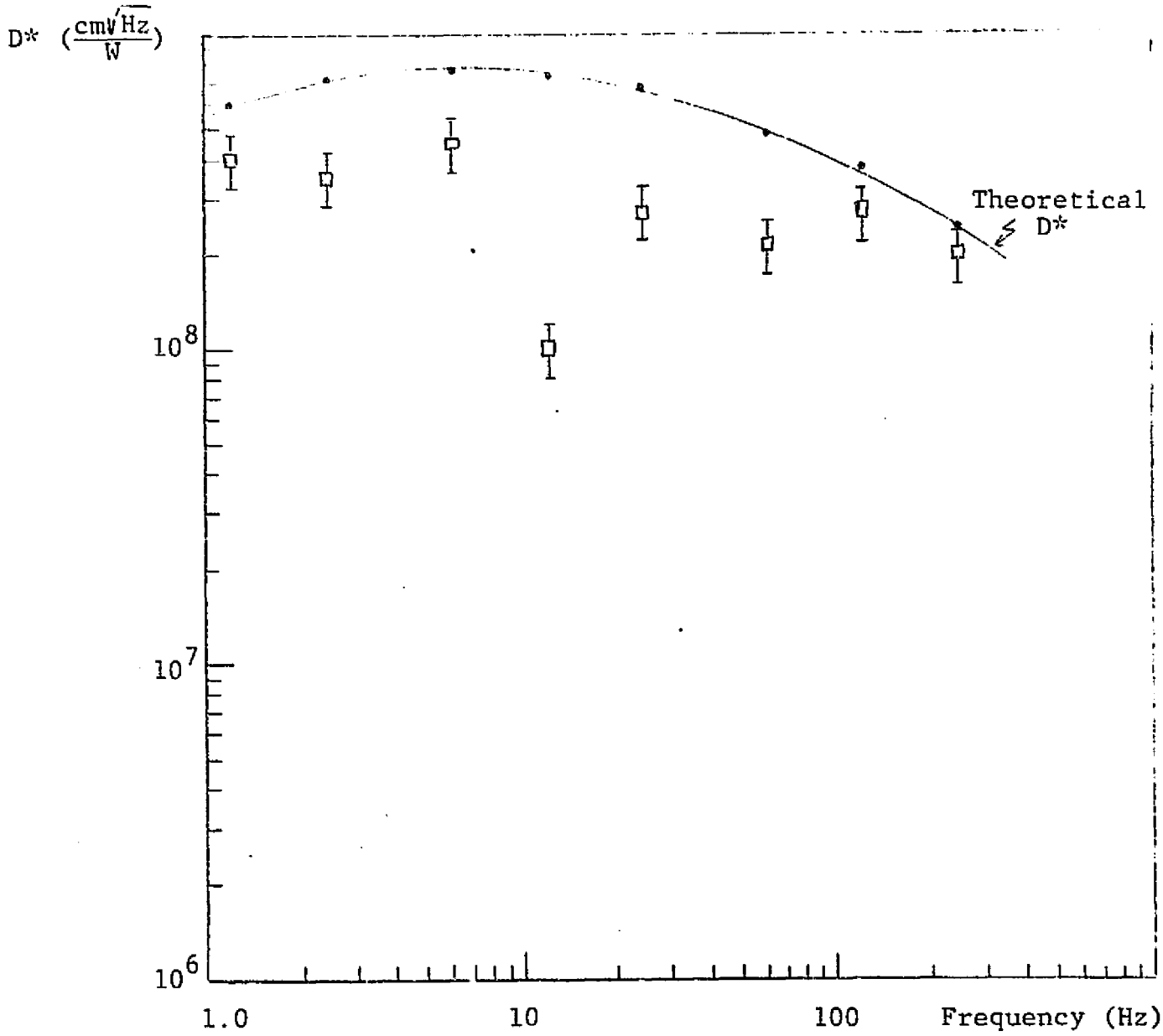

Figure 47 COMPARISON OF THEORETICAL AND EXPERIMENTAL D* OF SBN-13; f_o = 2.3 Hz, $\tan\delta$ = 0.002 in NOISE CALCULATIONS.

Table 13

NOISE CALCULATION PARAMETERS, CALCULATED AND EXPERIMENTAL NOISE FOR 080376-02-1

080376-02-1

$A = 7 \times 10^{-3} cm^2$	$C = 67pF$	$R_L = 1 \times 10^{11} \Omega$
$d = 35 \mu m$	$\tan\delta = 0.002$	$i_g = 0.1$ pA
$f_o = 1.3$ Hz	$p = 4.7 \times 10^{-8} \frac{coul}{cm^2 °C}$	$T = 293K$

	Theoretical Noise ($V/\sqrt{Hz}$)		Experimental Noise
Freq (Hz)	$V_n(f_o=1.3Hz, \tan\delta=0.002)$	$V_n(f_o=6Hz, \tan\delta=0.002)$	$V_n(V/\sqrt{Hz})$
1.2	1×10^{-6}	8.9×10^{-7}	8.3×10^{-7}
2.4	5.2×10^{-7}	5×10^{-7}	6.3×10^{-7}
6	2.2×10^{-7}	2.95×10^{-7}	3.1×10^{-7}
12	1.25×10^{-7}	1.6×10^{-7}	1.7×10^{-7}
24	7.5×10^{-8}	8.9×10^{-8}	1.1×10^{-7}
60	4.2×10^{-8}	4.6×10^{-8}	6.1×10^{-8}
120	2.9×10^{-8}	3.1×10^{-8}	4.4×10^{-8}
240	2.2×10^{-8}	2.2×10^{-8}	2.7×10^{-8}

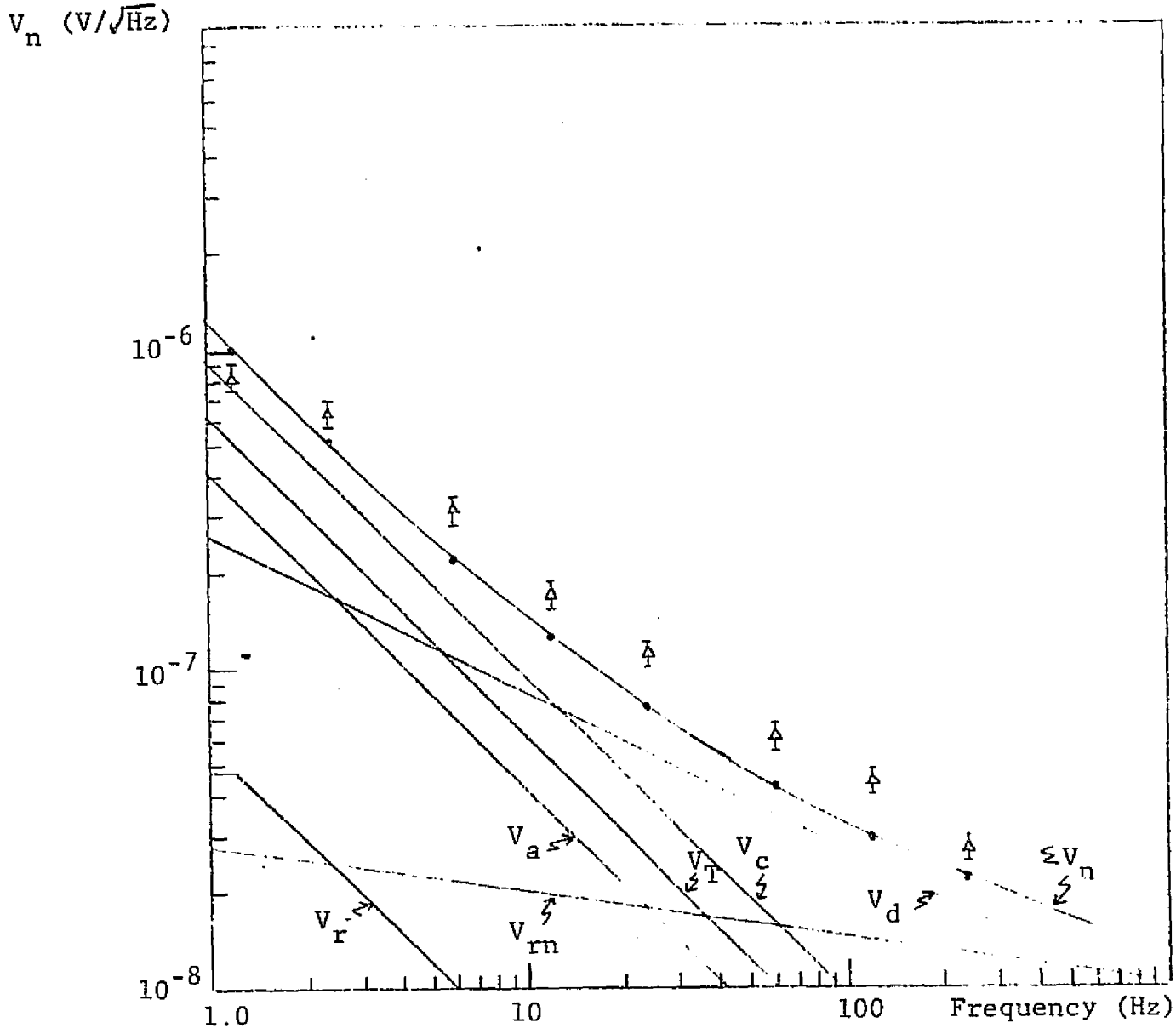

Figure 48 COMPARISON OF THEORETICAL AND EXPERIMENTAL NOISE OF 080376-02-1; f_o = 1.3Hz, tan δ = 0.002.

6 Hz and $\tan\delta = 0.002$, a better agreement between theory and experiment can be achieved. This is plotted in Figure 49. The D*'s corresponding to the noises plotted in Figures 48 and 49 are shown in Figures 50 and 51, respectively.

080376-02-4

In calculation the theoretical noise of 080376-02-4, the parameters shown in Table 14 were used, the results being plotted in Figure 52. To obtain a better match, a value of $f_o = 12$ Hz and an effective $\tan\delta = 0.0065$ were used. These results are shown in Figure 53. The resulting D*'s from the data of Figures 52 and 53 are shown in Figures 54 and 55, respectively.

Since SBN is piezoelectric as well as pyroelectric, any vibration of the detector can introduce some noise. For a detector mounted in air, the major source of noise occurs as a result of air vibrations. This source of noise can be eliminated by placing the detector into a vacuum dewar. However, there is still the possibility of vibration arriving at the detector through the dewar and mount. Thus the dewar must be properly mounted to reduce any vibrations of this sort. It was seen that if the dewar was placed in a foam-rubber filled box, the noise would increase. Rigid mounting of the dewar reduced the noise to its lowest value. The dewar holding structure is itself mounted on a large granite block. It appears, however, that for those detectors whose theoretical and experimental noise don't agree too well, the cause is microphonics. This can be expressed in terms of an increase value of the $\tan\delta$, i.e., the effective $\tan\delta$. If the dewar itself was suspended in a vacuum, perhaps this residual microphonics noise could be eliminated.

The thermal rolloff frequency of the detector responsivities was seen to vary from $f_o = 0.7$ Hz - 2.3 Hz. The value for f_o was obtained by determining at what frequency the voltage responsivity was a factor of 0.707 below the value expected if the detector were completely thermally isolated. This procedure is shown in Figure 56. The experimental value of R_v at 120 Hz is

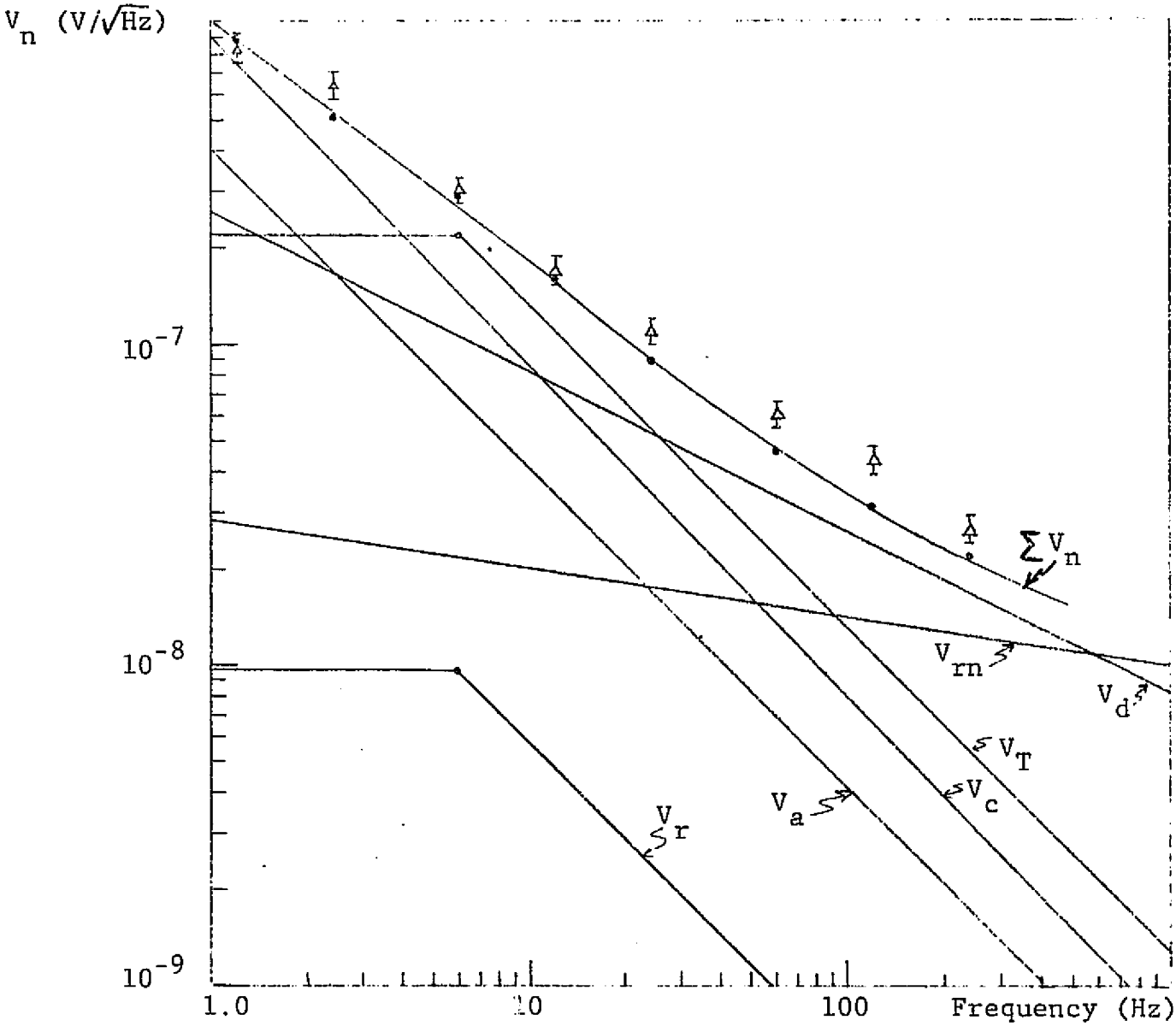

Figure 49 COMPARISON OF THEORETICAL AND EXPERIMENTAL NOISE OF 080376-02-1; f_o = 6 Hz, tanδ = 0.002.

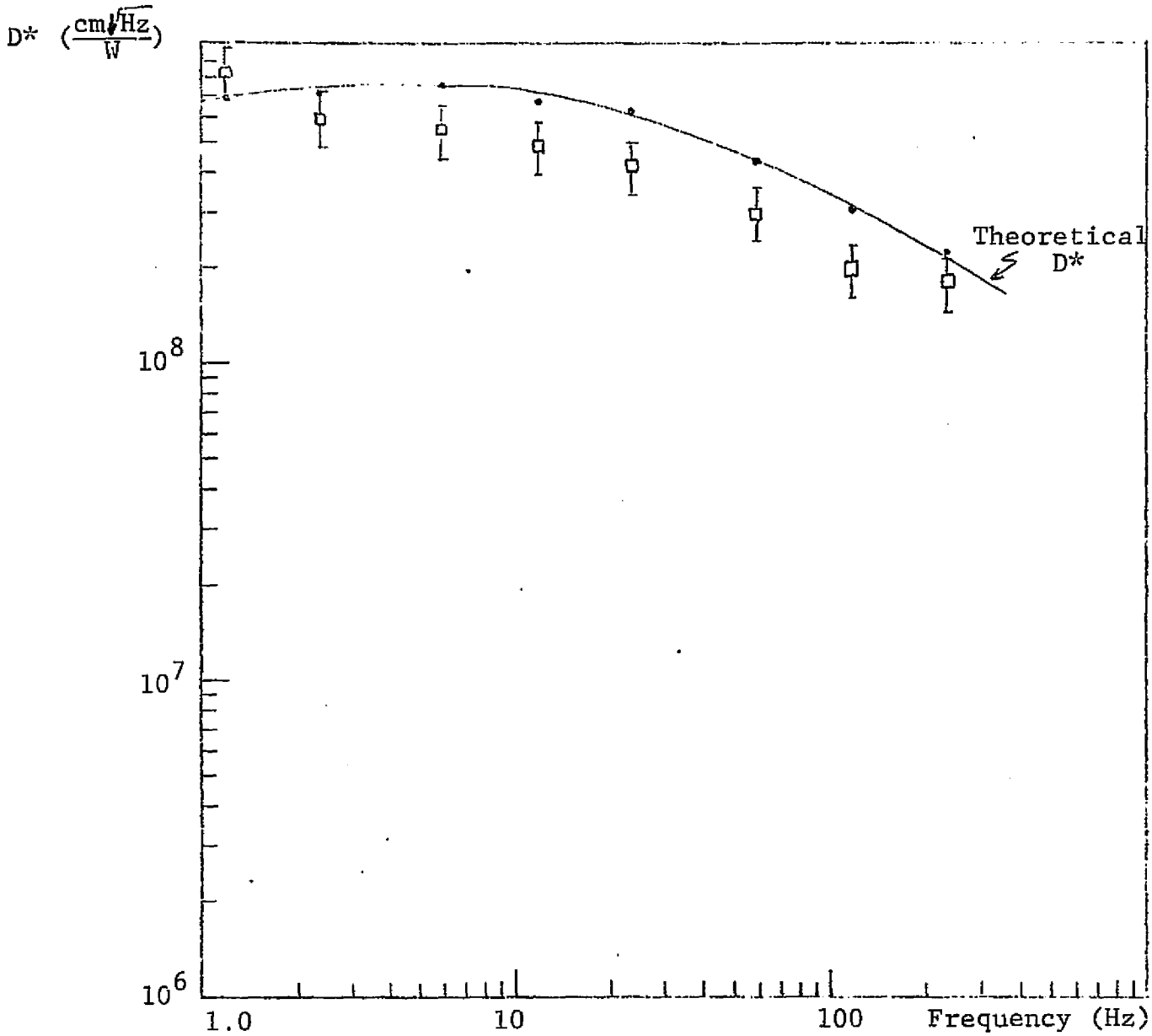

Figure 50 COMPARISON OF THEORETICAL AND EXPERIMENTAL D* OF 080376-02-1; WITH f_o = 1.3 Hz, tan δ = 0.002 IN NOISE CALCULATIONS.

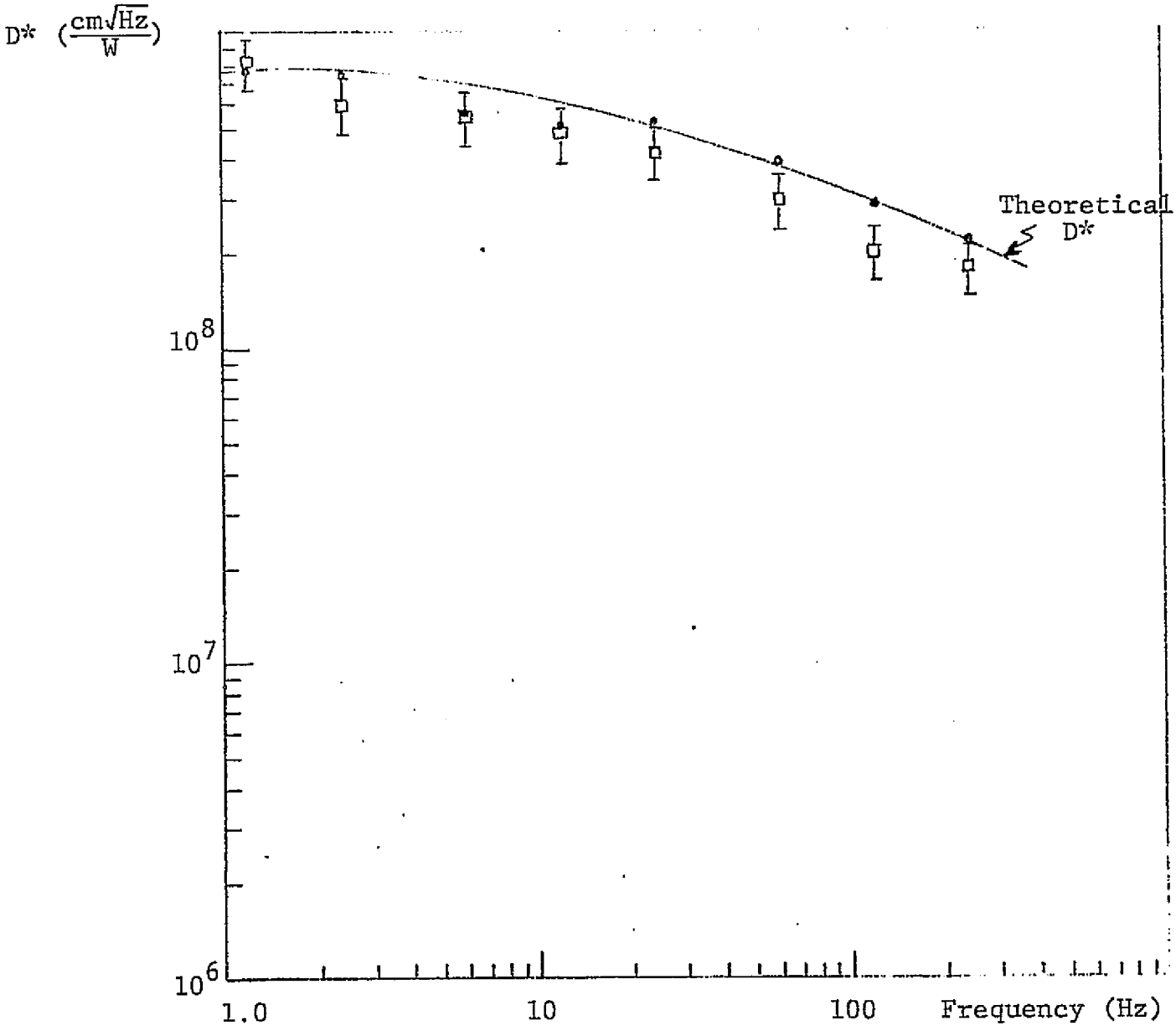

Figure 51 COMPARISON OF THEORETICAL AND EXPERIMENTAL D* OF 080376-02-1; WITH f_o = 6 Hz, tan δ = 0.002 IN NOISE CALCULATIONS.

C-2

Table 14

NOISE CALCULATION PARAMETERS, CALCULATED AND EXPERIMENTAL NOISE FOR 080376-02-4

080376-02-4

$A = 6.6 \times 10^{-3} cm^2$	$C = 51$ pF	$R_L = 1 \times 10^{11}\ \Omega$
$d = 45 \mu m$	$\tan\delta = 0.0024$	$i_g = 0.1$ pA
$f_o = 1$ Hz	$p = 5.3 \times 10^{-8} \frac{coul}{cm^2 °C}$	$T = 293K$

	Theoretical Noise ($V/\sqrt{Hz}$)		Experimental Noise
Freq (Hz)	$V_n(f_o=1Hz, \tan\delta = 0.0024)$	$V_n(f_o=12Hz, \tan\delta = 0.0077)$	$V_n(V/\sqrt{Hz})$
1.2	1.26×10^{-6}	1.22×10^{-6}	8.2×10^{-7}
2.4	6.4×10^{-7}	6.9×10^{-7}	5.4×10^{-7}
6	2.8×10^{-7}	3.8×10^{-7}	3×10^{-7}
12	1.66×10^{-7}	2.8×10^{-7}	2.4×10^{-7}
24	9.6×10^{-8}	1.65×10^{-7}	1.6×10^{-7}
60	5.2×10^{-8}	9×10^{-8}	9.7×10^{-7}
120	3.6×10^{-8}	5.4×10^{-8}	6×10^{-8}
240	2.5×10^{-8}	4.2×10^{-8}	3.6×10^{-8}

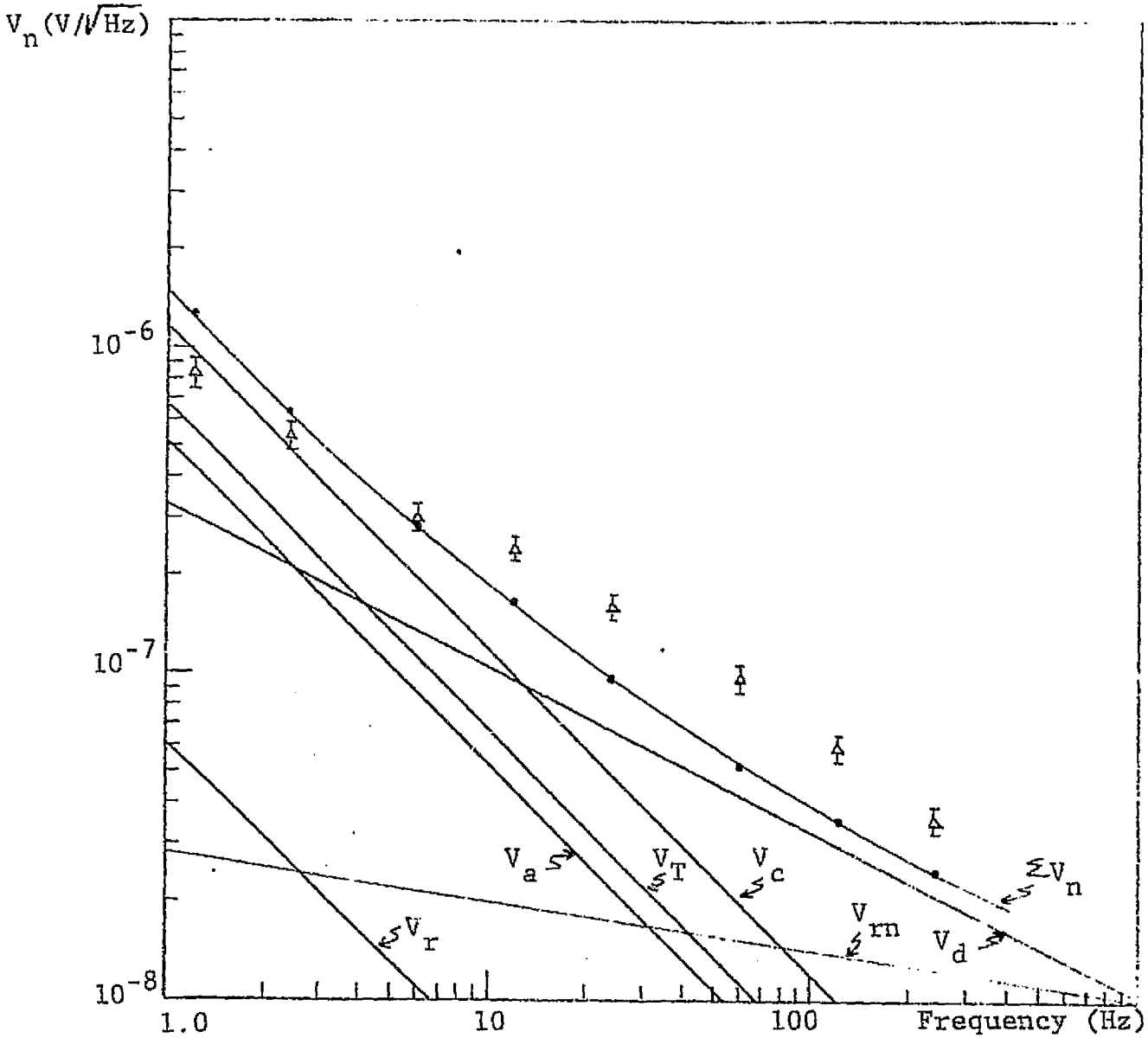

Figure 52 COMPARISON OF THEORETICAL AND EXPERIMENTAL NOISE OF 080376-02-4; f_o = 1 Hz, $\tan\delta$ = 0.0024.

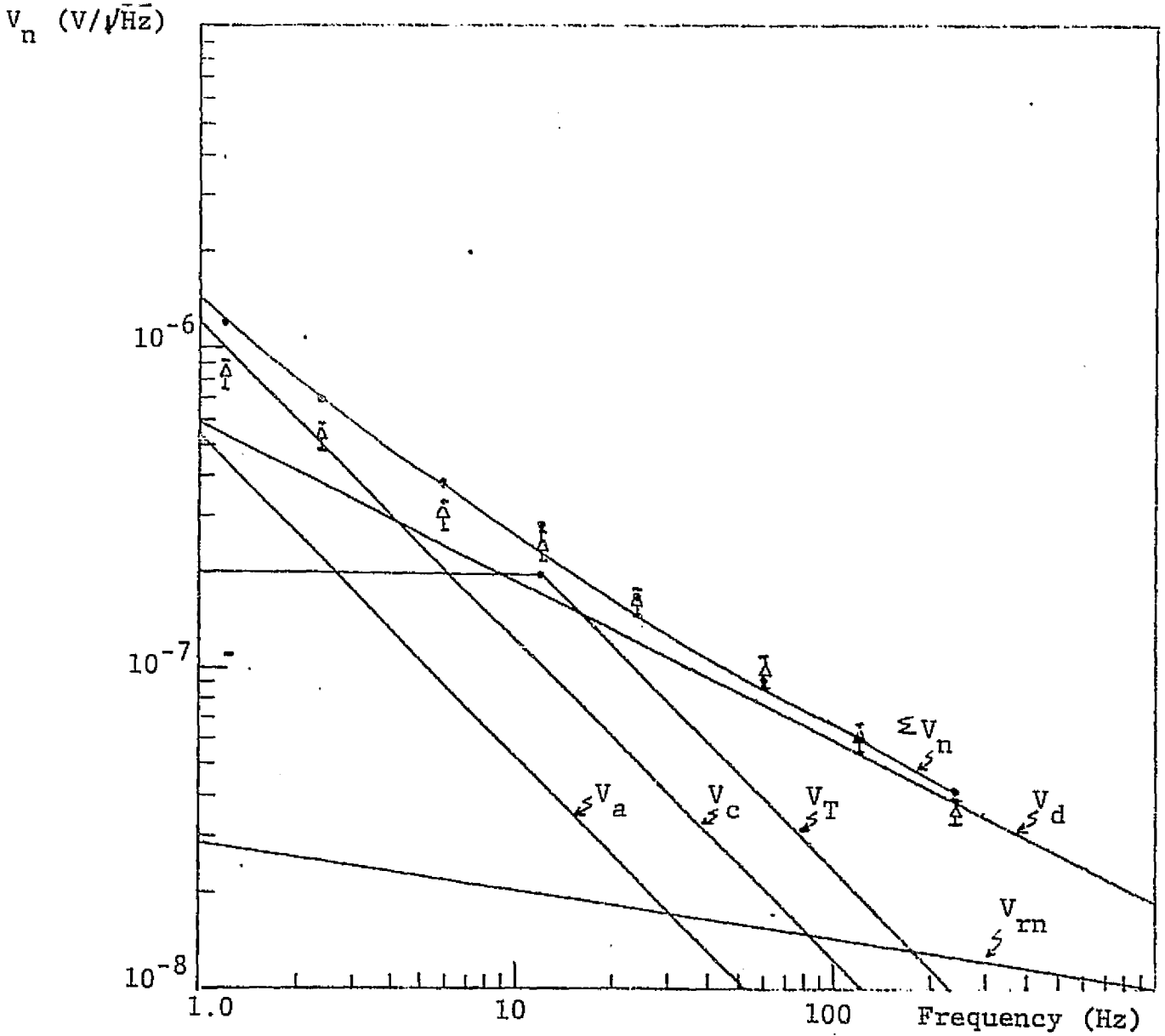

Figure 53 COMPARISON OF THEORETICAL AND EXPERIMENTAL NOISE OF 080376-02-4, f_o = 12 Hz, $\tan\delta$ = 0.0077.

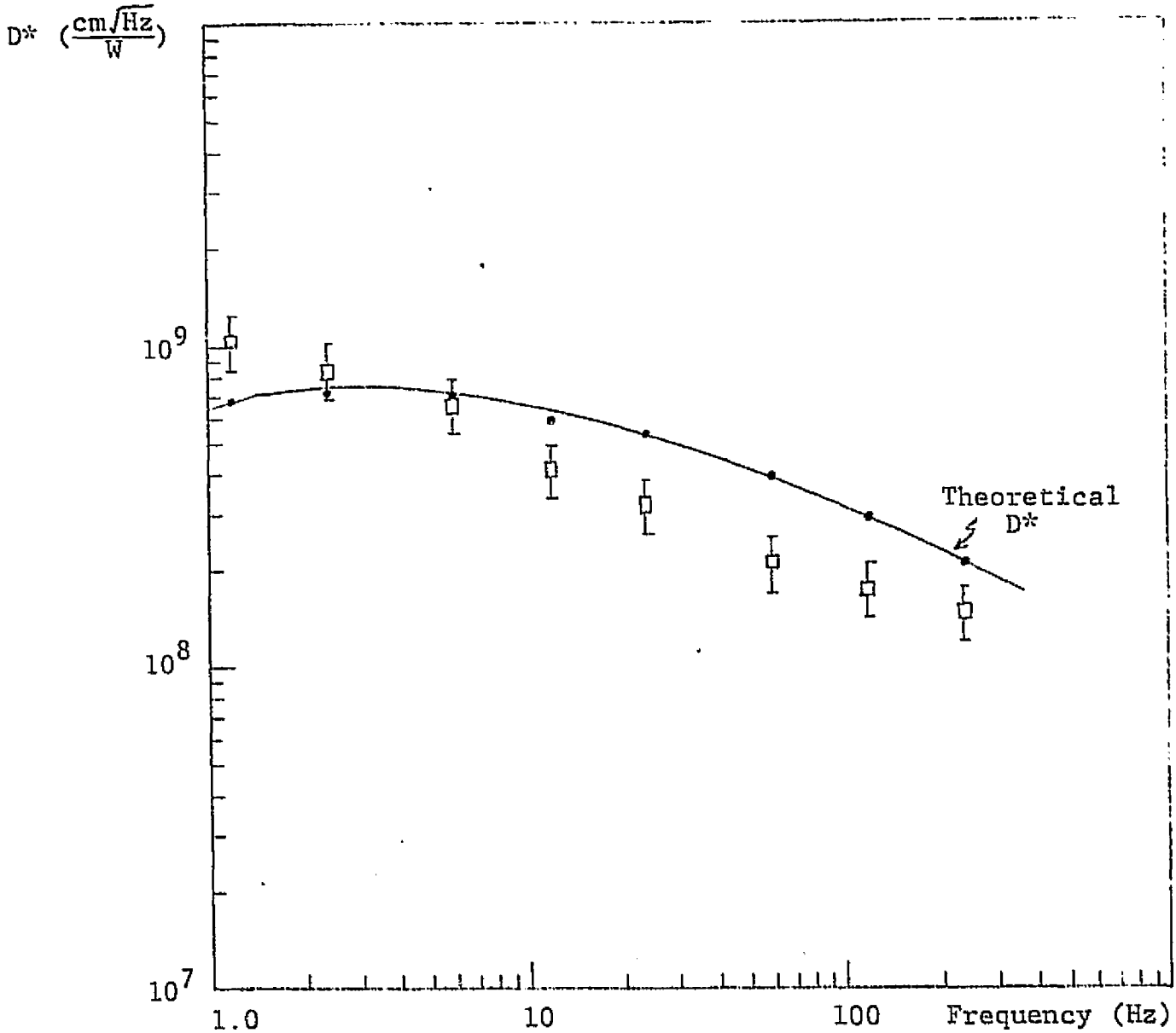

Figure 54 COMPARISON OF THEORETICAL AND EXPERIMENTAL D* OF 080376-02-4; f_o = 1 Hz, tan δ = 0.0024 in NOISE CALCULATIONS.

/808-11

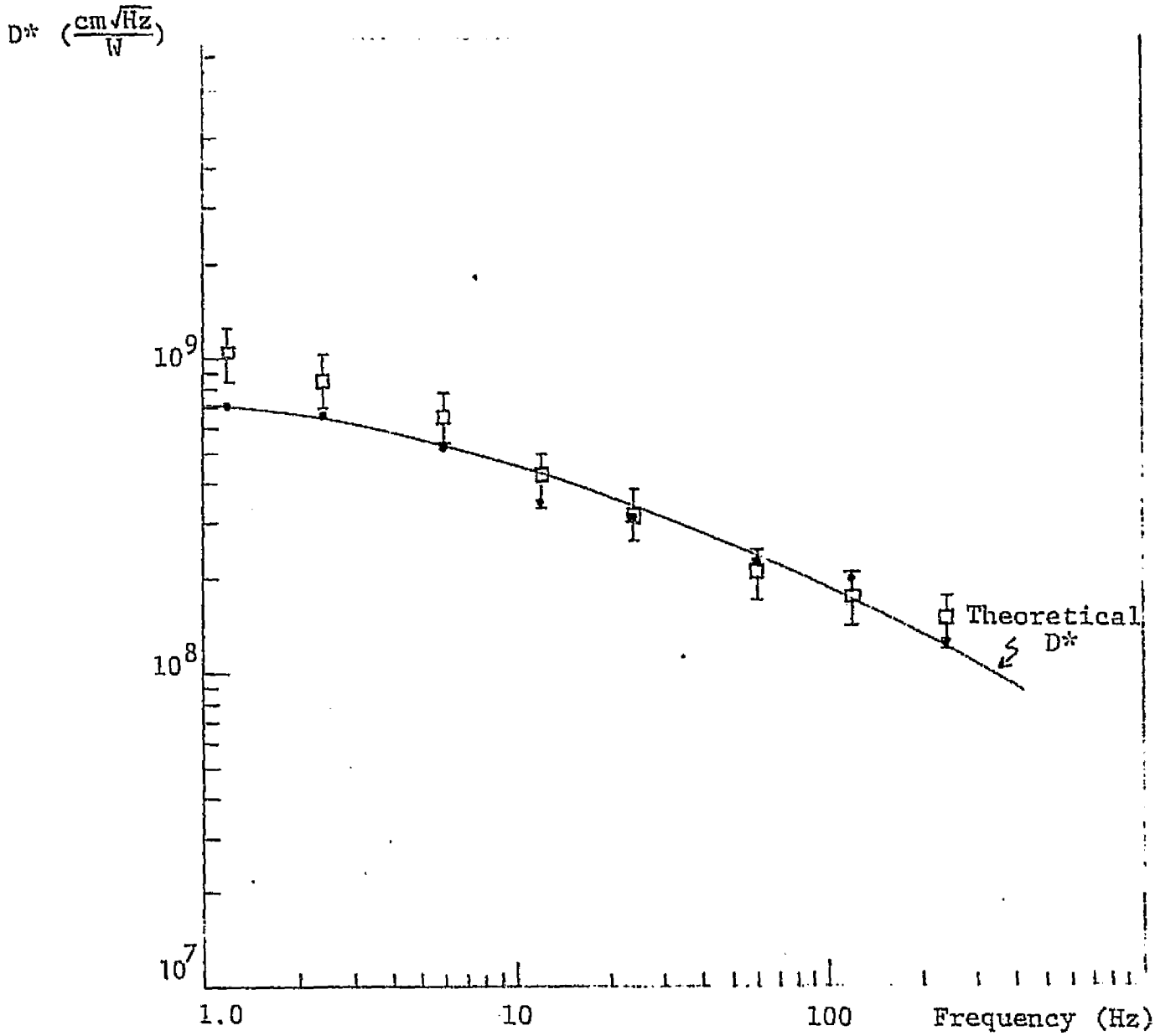

Figure 55 COMPARISON OF THEORETICAL AND EXPERIMENTAL D* OF 080376-02-4; f_o = 12 Hz, tan δ = 0.0077 in NOISE CALCULATIONS.

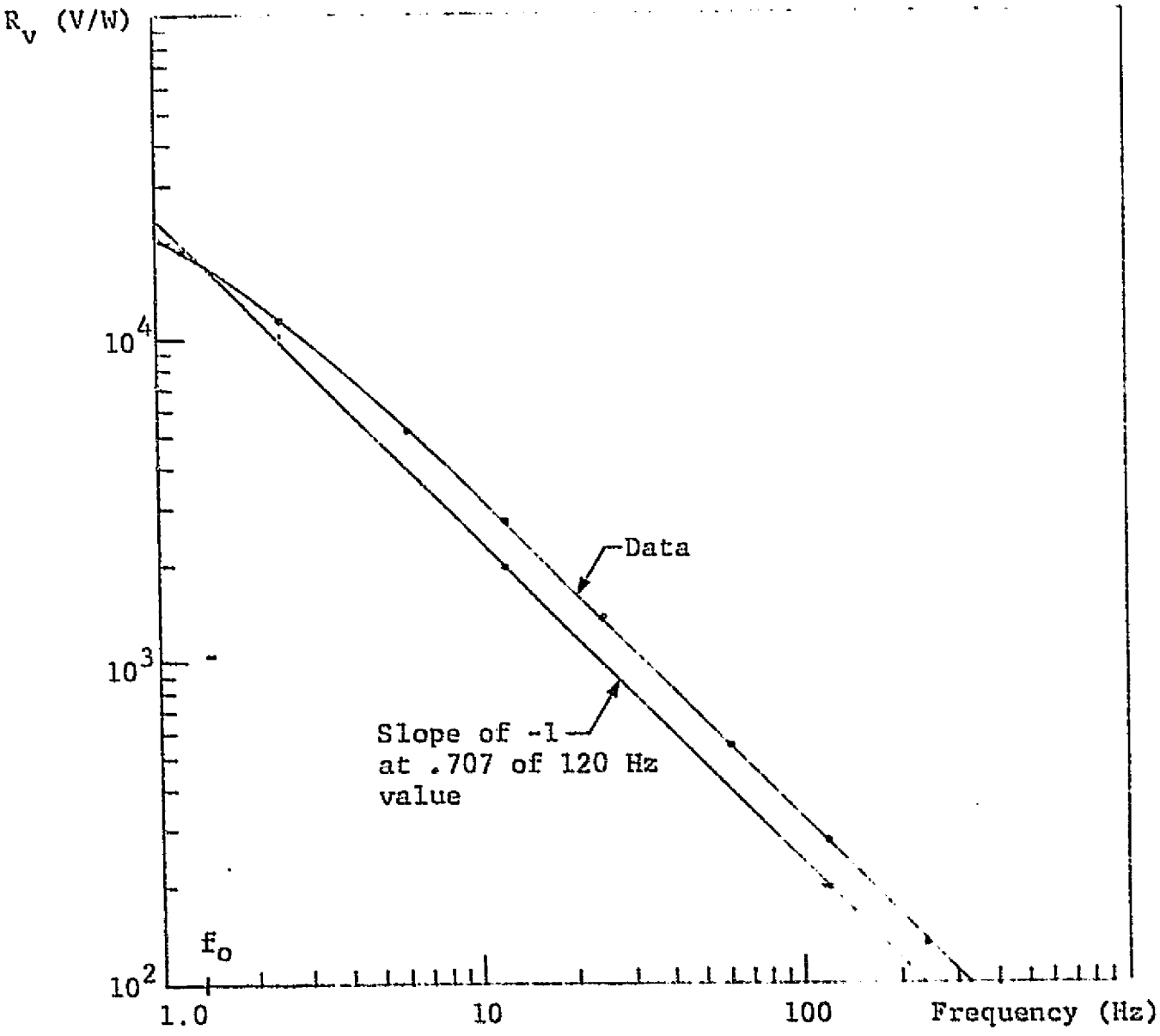

Figure 56 THERMAL ROLLOFF FREQUENCY (f_o) DETERMINATION FOR SBN-6.

used as a reference. Since this frequency is far above the thermal rolloff frequency, a line with a slope of 1/f is drawn through the point 0.707 R_v (120 Hz). The frequency at which this line intersects the experimental curve is taken to be f_o. Note that the value of f_o = 2.3 Hz is the highest observed, and this was seen for detector SBN-13. This particular detector was the only one not enclosed in a vacuum. Therefore, thermal conduction to the air, in addition to thermal conduction to the mount, was important.

It has been seen that the noise that is observed is not due entirely to the detector. It would therefore be of interest to remove these noise sources analytically and determine what the detector tanδ limited D* would be. This will be done as indicated in the following equations:

$$v_d^2 = e_{meas}^2 - v_T^2 - v_r^2 - v_a^2 - v_c^2 - v_{R_n}^2 \qquad (22)$$

Then the D* will be computed according to:

$$D^* = \frac{R_v}{V_d} \sqrt{A} \qquad (23)$$

The results of this computation are summarized in Table 15.

As a check of the variation of the voltage responsivity rolloff frequency with respect to the thermal conductance to the mounting, a sample was prepared which was either suspended from leads (low thermal conductivity) or completely heat sunk to the TO-5 can. The results are shown in Figure 57. Note the high degree of rolloff for the heat sunk detector, while for the suspended detector, $f_o << 1.2$ Hz. The pyroelectric coefficient of the material can be calculated from the voltage responsivity (Equation 14). This was done, and a value of $p_1 = 2.4 \times 10^{-8}$ coul/cm^2 ^oC was obtained if $\eta = 1$. The value of p measured in the TE cooler assembly was $p_2 = 3.1 \times 10^{-8}$ coul/cm^2 ^oC. This latter value is independent of the emissivity of the front surface, and thus, the ratio p_1/p_2 can give a value for η. Here $\eta = p_1/p_2 = 0.77$, which is a reasonable value for the Pt black emissivity, including the effect of the black's spectral cutoff.

Table 15

D* OBTAINED FROM DETECTOR tan δ NOISE, WITH OTHER NOISE SOURCES REMOVED

	V_d(V/√Hz)	R_V(V/W)	D*($\frac{cm\sqrt{Hz}}{W}$)	D*(expt) ($\frac{cm\sqrt{Hz}}{W}$)	Freq(Hz)
SBN-3	1.06×10^{-6}	13194	7.7×10^{8}	5.8×10^{8}	1.2
SBN-6	1.2×10^{-6}	11370	6.8×10^{8}	5.1×10^{8}	2.4
SBN-8	3.5×10^{-7}	4881	9.4×10^{8}	6.1×10^{8}	2.4
SBN-12	5.9×10^{-7}	8402	9.1×10^{8}	6.4×10^{8}	2.4
SBN-13	1.14×10^{-6}	8864	5.3×10^{8}	4×10^{8}	1.2
080376-02-1	3.9×10^{-7}	8223	9.5×10^{8}	8.3×10^{8}	1.2
080376-02-4	1.7×10^{-7}	2434	1.15×10^{9}	6.6×10^{8}	6

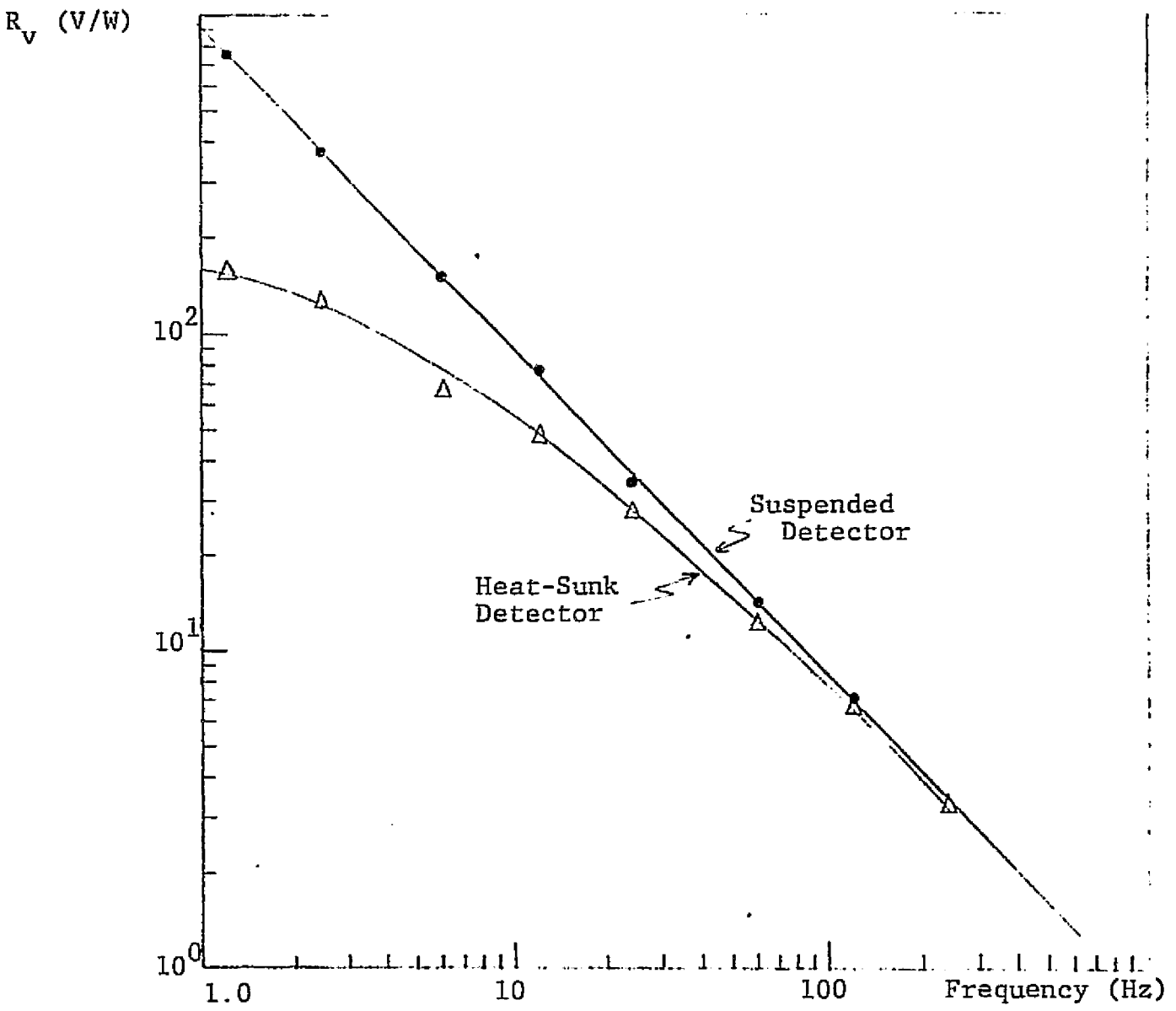

Figure 57 EFFECT OF THERMAL CONDUCTIVITY OF MOUNT ON DETECTOR VOLTAGE RESPONSIVITY, R_V. SAMPLE 080576-02.

SECTION 7

CONCLUSIONS AND RECOMMENDATIONS

The technical objectives of this program were to quantitatively relate SBN pyroelectric detector performance to theoretical predictions by varying and optimizing where possible crystal growth, wafer preparation, detector fabrication and mounting techniques. As a measure of our success in this effort, the following conclusions are identified.

Tan δ Improvement

The loss tangent was improved by a factor of 15 from 0.003 to 0.0002 by a unique poling technique. A D* value of 1.3×10^9 cm $Hz^{1/2}$/watt was achieved based on this technique.

Pyroelectric Coefficient Determination

It was found that high pyroelectric coefficients ($\geq$60% of theory) could be achieved without being impacted by the unique poling for minimizing of tan δ.

Absence of Dislocated Density Degradation

No performance degradation relatable to dislocation density was found for over a factor of 10 change in dislocation density variation.

Optimum Thinning Technique

It was found that ion milling was far superior to mechanical polishing and grinding for thinning to 10 to 15 μm based on yield as a criteria.

High Emissivity Black Coating

It was found that platinum black was <10% reflective out to 12 μm, and it also was compatible to a platinum sintering electrode process found to be highly successful on SBN detectors.

Optimum Thermal Mounting

A method of mounting detectors using a low conductivity thermal bump was demonstrated. This process with some slight modifications will be used for mosaic pyroelectric detector arrays.

It was generally concluded, based on extensive data, that SBN detector performance is consistent to the theory. This is an important conclusion, since variations in size and mounting configuration of the detector, and coupling to a CCD can now be based on a sound understanding of pyroelectric detector behavior.

Future work should address itself to (1) array technology, and (b) coupling to CCD's. Honeywell is already making pyroelectric detector arrays of thirtytwo elements connected with bumps similar to the ones developed on this program. This process should be optimized in much the same manner that crystal growth, wafer preparation and detector fabrication were optimized on this program. Additionally, interconnection to and readout with a CCD is technologically achievable now and should be investigated for optimum techniques and realizable performance compared to the theory.

REFERENCES

1. Rex Watton, Colin Smith, Brian Harper, and W.M. Wreathall, IEEE Transactions on Electron Devices, Vol ED21, No. 8, August 1974, pp. 462–469.

2. W.R. Blevin and Jon Geist, Applied Physics, Vol. 13, No. 5 May 1974, pp. 1171–1178.

3. B.E, Holeman, Infrared Physics, 1972, Vol. 12, pp. 125–135, Pergamon Press.

4. Sawyer, C.B. and Tower, C.H. Phys. Rev., 35 pp. 269 (1930).

5. Maciolek, R.B. and Liu, S.T., Journal Electronic Mat., 2 pp. 191 (1973).

6. Texmet is trademark of Buehler, Ltd, Evanston, Illinois.

7. Jones, R.C., Advances in Electronics, 5, pp. 1–96 (1953).

APPENDIX A

TEST REPORT NO. 22172-3

FOR

SBN INFRARED DETECTORS

(LK232A1, S/N R1 ; LK232A1, S/N R2)

PREPARED FOR:

NATIONAL AERONAUTICS AND SPACE ADMINISTRATION
LANGLEY RESEARCH CENTER
HAMPTON, VIRGINIA 23365

CONTRACT NAS1-14372

MARCH 20, 1978

PREPARED BY:

J. W. Marciniec 3/23/78
J. W. Marciniec
Associate Research Engineer

J. C. Gelpey 3/22/78
J. C. Gelpey
Research Engineer

APPROVED BY:

D. E. Marshall
D. E. Marshall
Project Manager

Paul Nelson 3-23-78
Paul Nelson
Product Assurance

HONEYWELL INC.
Electro-Optics Center
2 Forbes Road
Lexington, Massachusetts 02173

INTRODUCTION

This test report was prepared for the Electronic Devices Research Branch, NASA Langley Research Center, Hampton, Virginia under NASA contract NAS1-14372. The NASA Technical Representatives for this contract were Dr. Roger K. Crouch and Dr. James B. Robertson.

The strontium barium niobate (SBN) infrared detectors described in this test report were developed, fabricated and characterized at the Honeywell Electro-Optics Center in Lexington, Massachusetts.

The devices were fabricated by Mr. William Burnett and Mr. Brian Denley. The technical assistance of Mr. John Monahan in the testing of the devices is appreciated.

This test report presents performance data for two (2) strontium barium niobate ($Sr_{1-x}Ba_xNb_2O_6$, with x = 0.5) pyroelectric infrared detectors, each integrated with a matching JFET preamplifier and load resistor. These detectors are mounted in a metal dewar, chosen to enable the developmental detectors to be characterized conveniently over the 192 - 293°K temperature range.

TABLE OF CONTENTS

1.0 DESCRIPTION OF DETECTORS

Type of Detector	Pyroelectric
Material	$Sr_{1-x}Ba_xNb_2O_6$; x = 0.5
Window	Ge, Thickness = 40 mil Antireflection coated
JFET	U423, Siliconix

2.0 DETECTOR PARAMETERS AND TESTS CONDUCTED

A summary of the characteristics and performance of the two (2) SBN pyroelectric detectors is contained in Table I.

UNIT (Window Aperture =7/8")	DETECTOR ID	DETECTOR SIZE		DIELECTRIC PROPERTIES			DETECTIVITY vs. TEMPERATURE		DISTANCE FROM SURFACE OF DEWAR WINDOW TO DETECTOR (cm)
		ACTIVE AREA ($10^{-3}cm^2$)	THICKNESS (μm)	FREQUENCY (k Hz)	T=20°C Capacitance (pF)	T=20°C tanδ	TEMPERATURE (K)	DETECTIVITY (FREQUENCY = 1.2Hz) 10^8 cm-$Hz^{1/2}$/Watt)	
LK232A1, S/N R1	080376-02 -1	7.0	~ 35	0.12 1 10	67 68 67	0.002 0.0014 0.001	293 276 243 192	8.3 10.4 10.7 4.9	1.70
LK232A1, S/N R2	080376-02 -4	6.6	~ 45	0.12 1 10	51 51 50	0.0024 0.0015 0.001	293 276 243 192	10.5 13.3 10.7 9.5	1.77

TABLE I - PHYSICAL PARAMETERS AND PERFORMANCE OF DETECTORS

3.0 MEASUREMENT CONDITIONS

3.1 Physical Parameters

Blackbody Temperature (T_{BB})	500 K
Blackbody Aperture (d_A)	0.254 cm
Background Temperature (T_A)	293 K
Stefan-Boltzmann Constant (σ)	5.67×10^{-12} W/cm^2 °K^4
Detector to Orifice Distance (d)	15 cm
Chopping Frequency	1.2 - 240 Hz
Sine to RMS Conversion Factor (C)	0.437
Noise Bandwidth (Δ f)	1 Hz
Emissivity ϵ: Blackbody, Chopper	1.0
Window Transmittance Factor (F)	0.8

3.2 Flux Density (H_{BB}) at Detector

$$H_{BB} = \epsilon\sigma\ (T_{BB}^4 - T_A^4)\ \frac{d_A^2}{4d^2}\ C \cdot F\ (W/cm^2)$$

$$H_{BB} = 7.8 \times 10^{-6}\ (\pm\ 1 \times 10^{-6})\ W/cm^2$$

3.3 Blackbody Responsivity (R_{BB})

$$R_{BB} = \frac{V_{sig}}{H_{BB}\ A_d}\ (V/W)$$

3.4 Blackbody Detectivity (D^*_{BB})

$$D^*_{BB} = \frac{R_{BB}}{V_n} \cdot \sqrt{A_d}\ (cm\ \sqrt{Hz}\ /W)$$

3.5 Window Transmittance Factor(F)

The calculation of the Window Transmittance Factor (F) is as follows. Due to the antireflection coating, the surface reflection (R) is only 6%. However, the window transmittance begins to cutoff at ~15.5 μm. For a 500 K blackbody, a 15% loss of energy (W_L) results. This can be expressed as:

$$F = (1-R)(1-W_L) = (1-0.06)(1-0.15) = 0.8$$

The responsivity and noise measurements were made using a Spectral Dynamics Corporation Model SD335 Real Time Analyzer, with preamplification by a Honeywell and a Princeton Applied Research Model 113 preamplifier combination.

The plotted responsivity and detectivity data includes the window transmittance factor, thus the data is normalized to the detector surface.

The cryogenics used for the low temperature measurements were:

Ice Water - 273 K

Freon 12 - 243 K

Freon 13 - 192 K

4.0 TEST RESULTS

4.1 080376-02-1 Test Results

DETECTOR ID: 080376-02-1
DETECTOR AREA 7×10^{-3} cm^2
THICKNESS 35 μm
BLACKBODY TEMPERATURE 500 K
DETECTOR TEMPERATURE 293 K
DETECTOR IN VACUUM

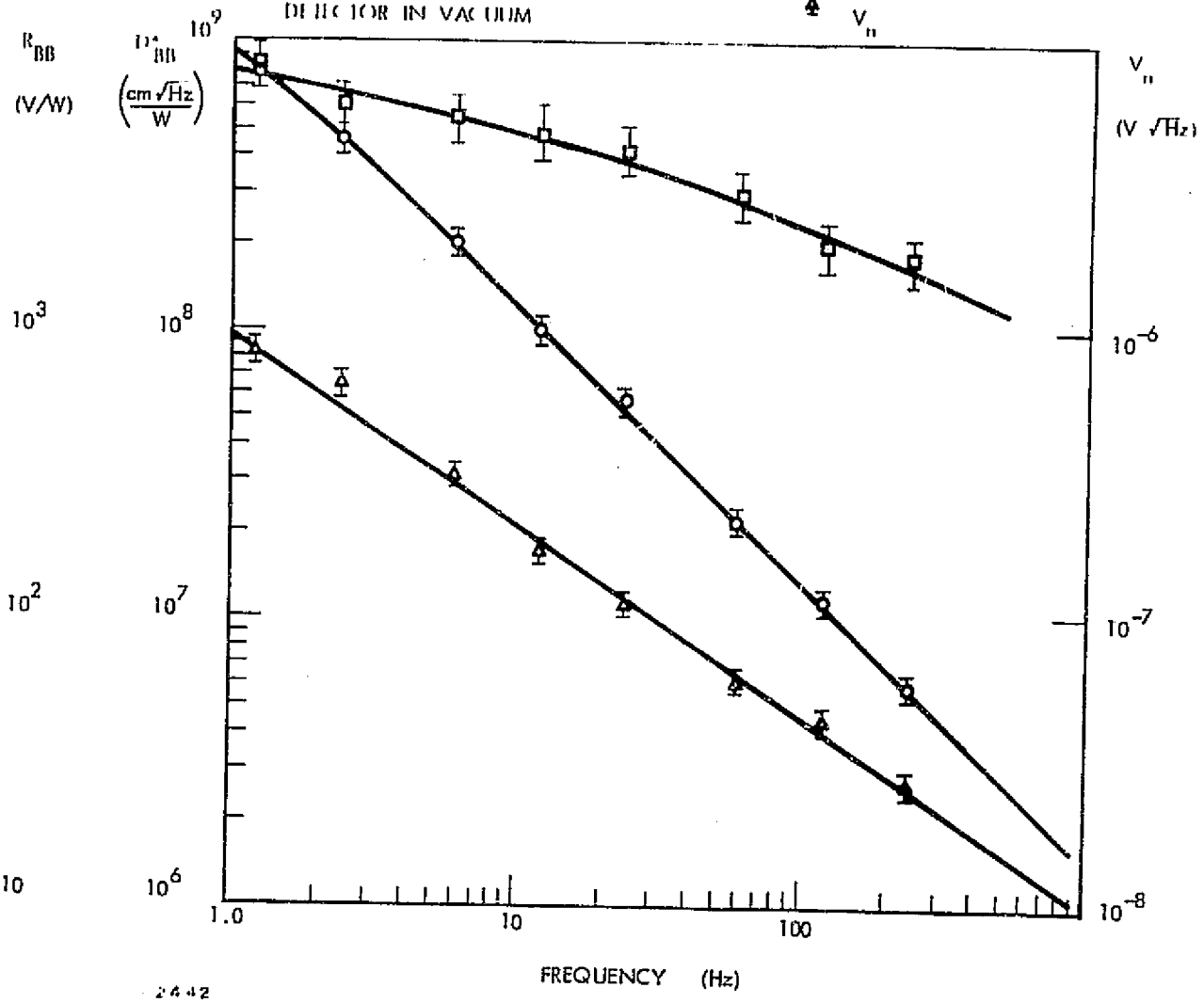

FIGURE 1 DETECTOR PERFORMANCE 080376-02-1, 293K

DETECTOR ID: 080376-02-1
DETECTOR AREA $7 \times 10^{-3} cm^2$
THICKNESS ~ 35 μm
BLACKBODY TEMPERATURE = 500 K
DETECTOR TEMPERATURE 276 K
DETECTOR IN VACUUM

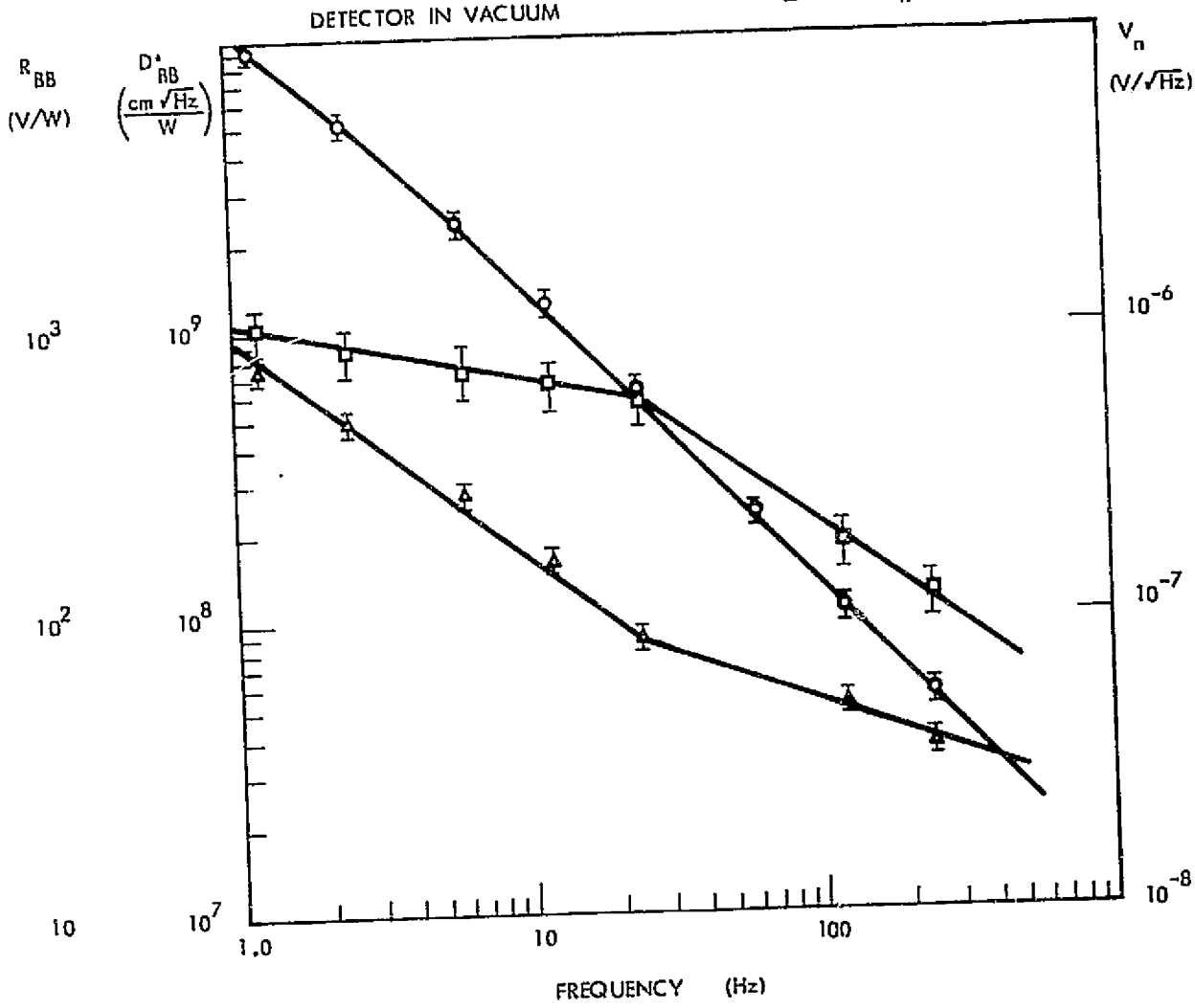

FIGURE 2 DETECTOR PERFORMANCE 080376-02-1, 276 K

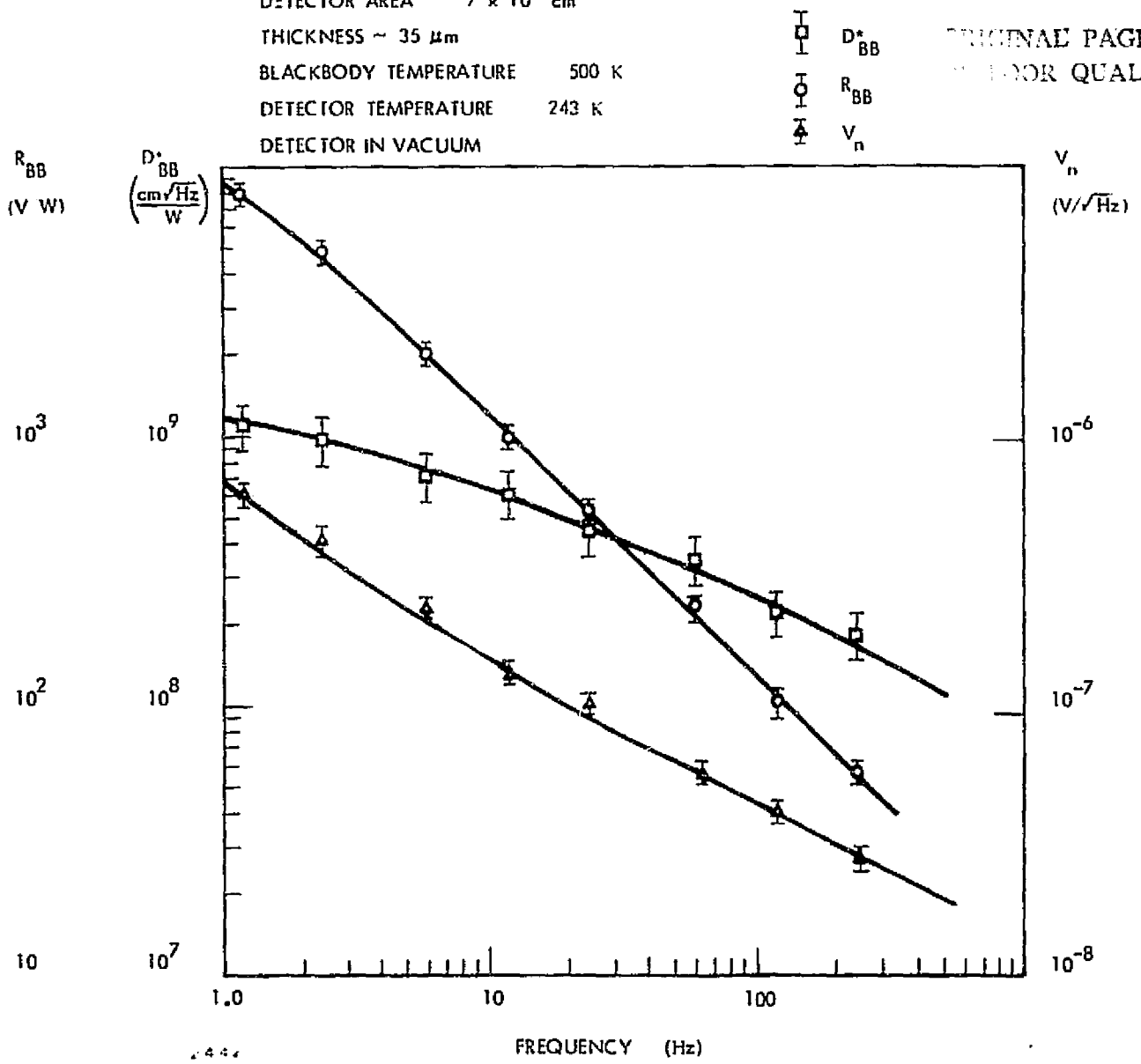

Figure 3 DETECTOR PERFORMANCE 080376-02-1, 243 K

DETECTOR ID: 080376-02-1
DETECTOR AREA $7 \times 10^{-3} cm^2$
THICKNESS 35 μm
BLACKBODY TEMPERATURE 500 K
DETECTOR TEMPERATURE 192 K
DETECTOR IN VACUUM

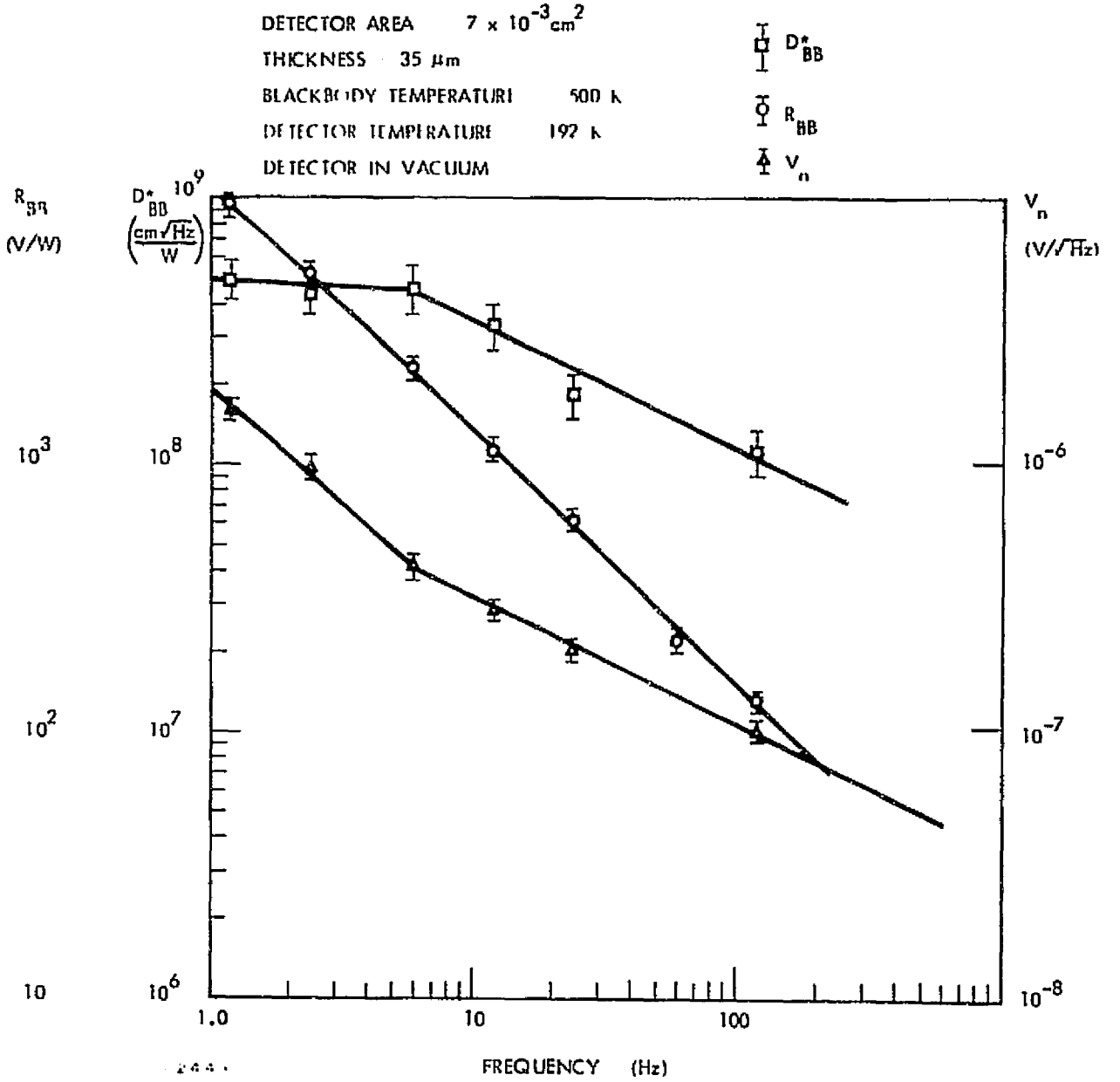

FIGURE 4 DETECTOR PERFORMANCE 080376-02 -1, 192 K

4.2 080376-02-4 Test Results

DETECTOR ID 080376-02-4
DETECTOR AREA $6.6 \times 10^{-3} cm^2$
THICKNESS ~ 45 μm
BLACKBODY TEMPERATURE 500 K
DETECTOR TEMPERATURE 293 K
DETECTOR IN VACUUM

D^*_{BB}
R_{BB}
V_n

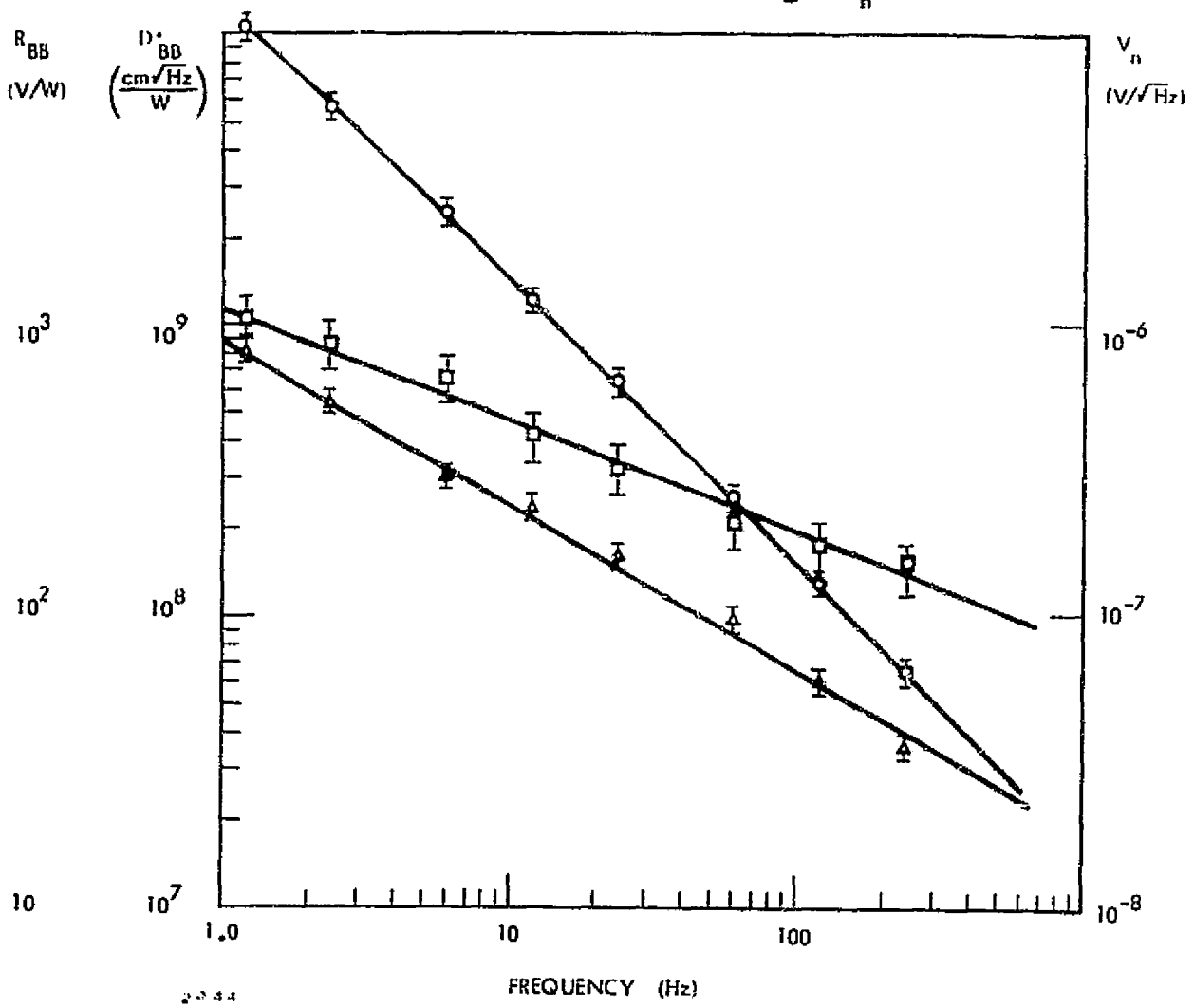

FIGURE 5 DETECTOR PERFORMANCE 080376-02-4, 293 K

DETECTOR ID: 080376-02-4
DETECTOR AREA 6.6×10^{-3} cm^2
THICKNESS 45 μm
BLACKBODY TEMPERATURE 500 K
DETECTOR TEMPERATURE 276 K
DETECTOR IN VACUUM

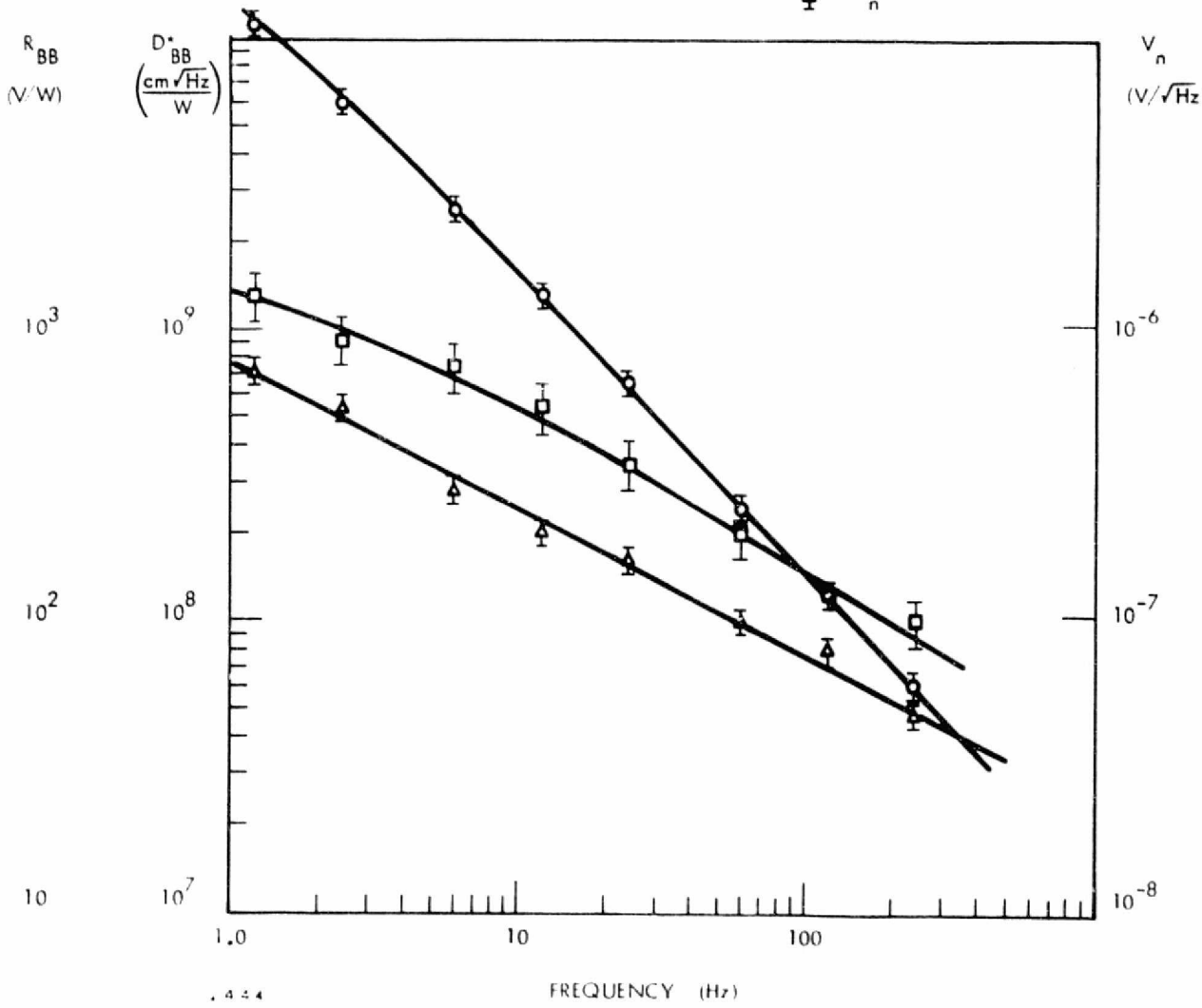

FIGURE 6 DETECTOR PERFORMANCE 080376-02-4, 276 K

DETECTOR ID: 080376-02-4
DETECTOR AREA 6.6×10^{-3} cm^2
THICKNESS 45 μm
BLACKBODY TEMPERATURE 500 K
DETECTOR TEMPERATURE 243 K
DETECTOR IN VACUUM

D^*_{BB}
R_{BB}
V_n

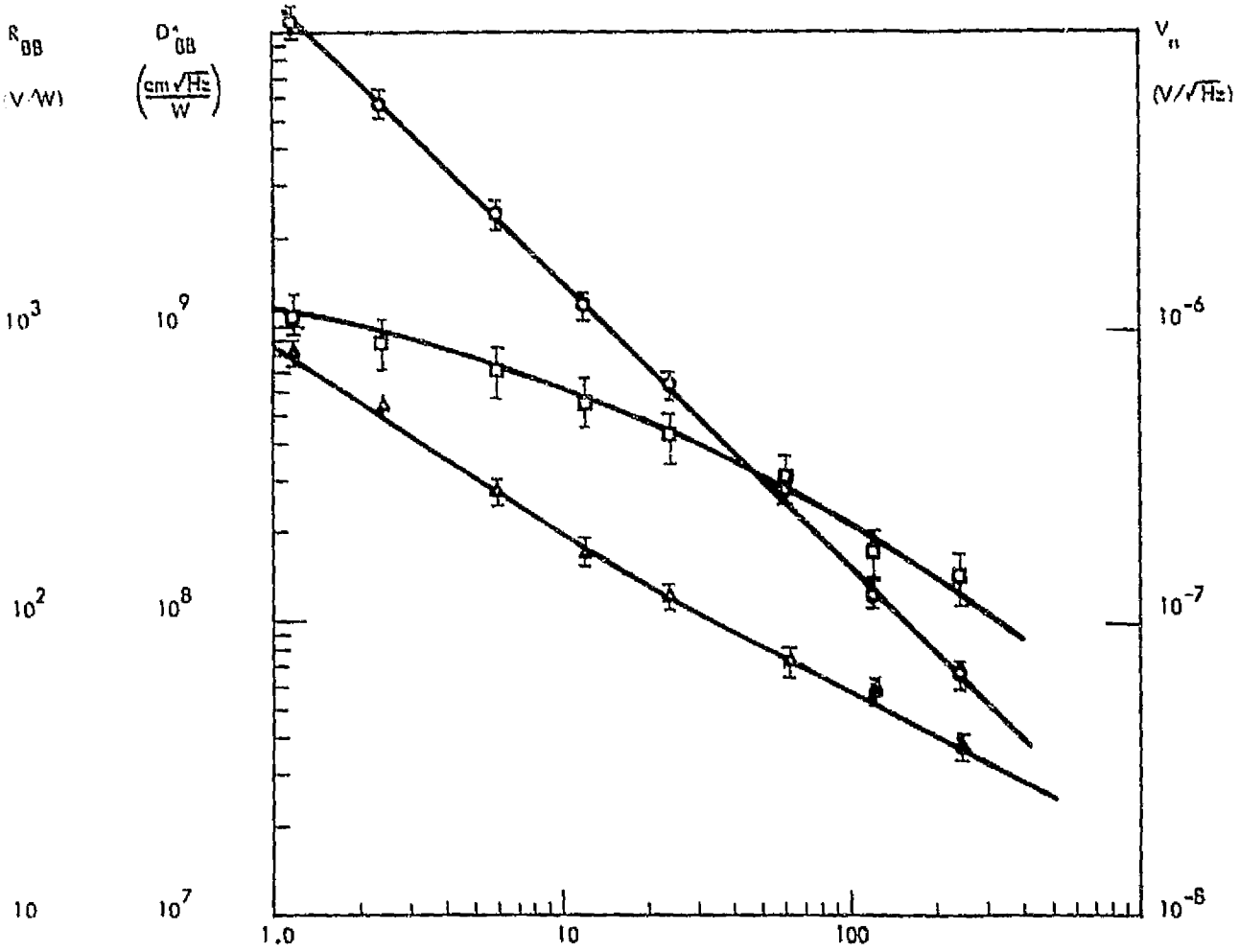

FIGURE 7 DETECTOR PERFORMANCE 080376-02-4, 243 K

DETECTOR ID: 080376-02-4
DETECTOR AREA 6.6×10^{-3} cm^2
THICKNESS ~ 45 µm
BLACKBODY TEMPERATURE 500 K
DETECTOR TEMPERATURE 192 K
DETECTOR IN VACUUM

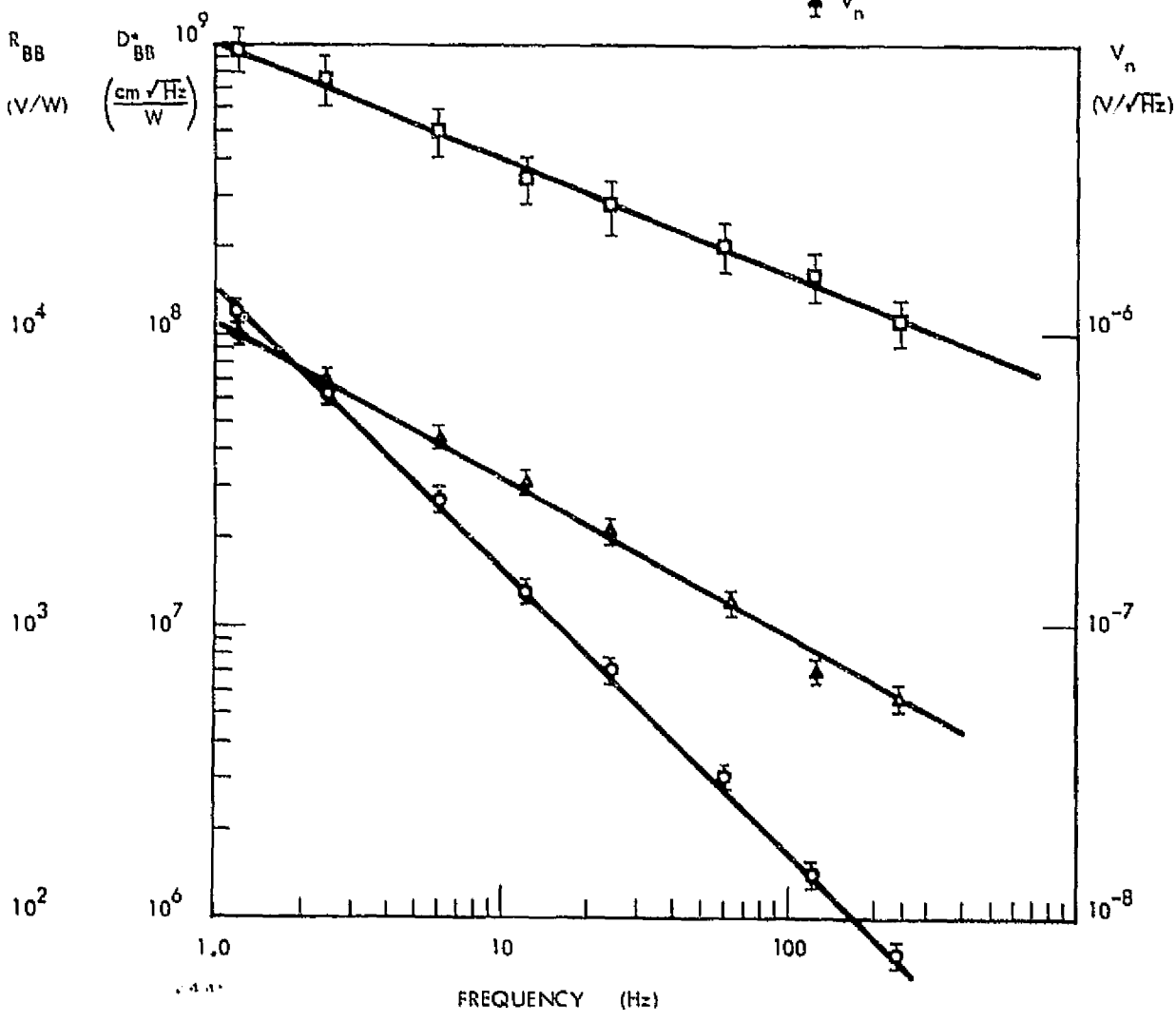

FIGURE 8 DETECTOR PERFORMANCE, 080376-02-4, 192 K

4.3 Summary of Temperature Dependence of D^*_{BB}, Responsivity, and Noise of Detectors, at 1.2 Hz

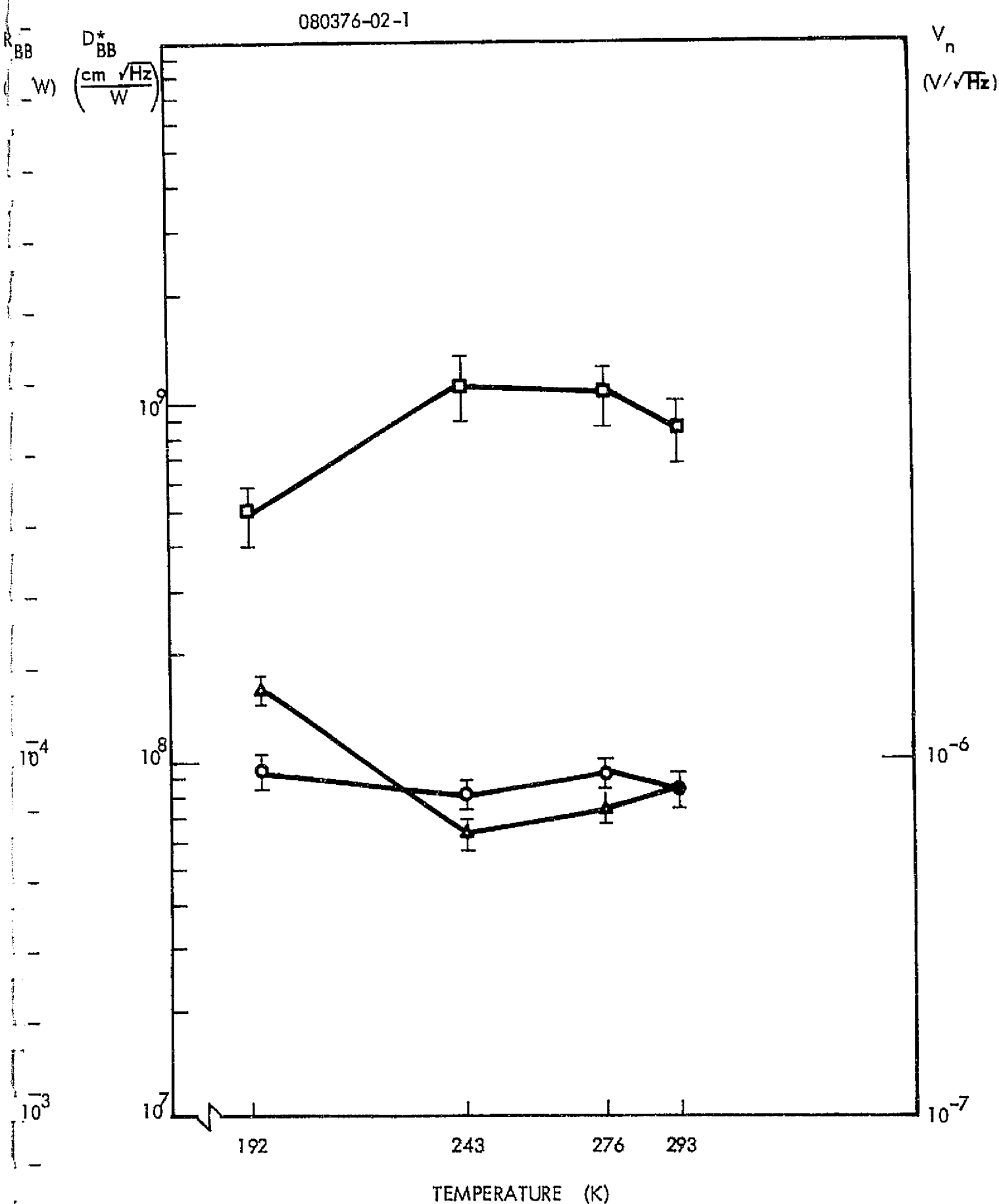

2441 FIGURE 9 TEMPERATURE BEHAVIOR OF DETECTOR 080376-02-1
D*, RESPONSIVITY AND NOISE. FREQUENCY = 1.2 Hz A19

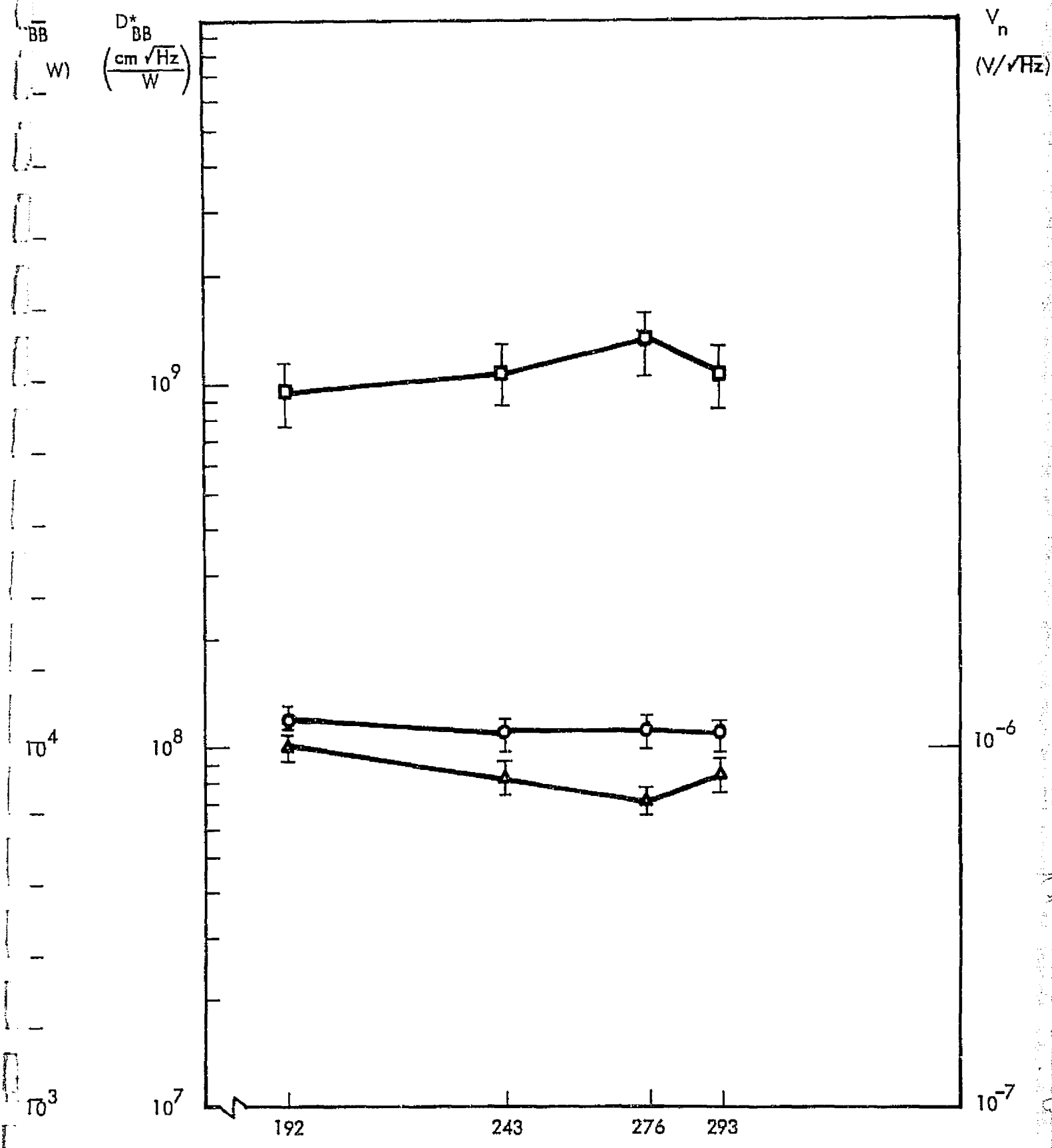

FIGURE 10 TEMPERATURE BEHAVIOR OF DETECTOR 080376-02-4
D*, RESPONSIVITY, AND NOISE. FREQUENCY = 1.2 Hz

4.4 Temperature Dependence of Detectors' Capacitance and tan δ

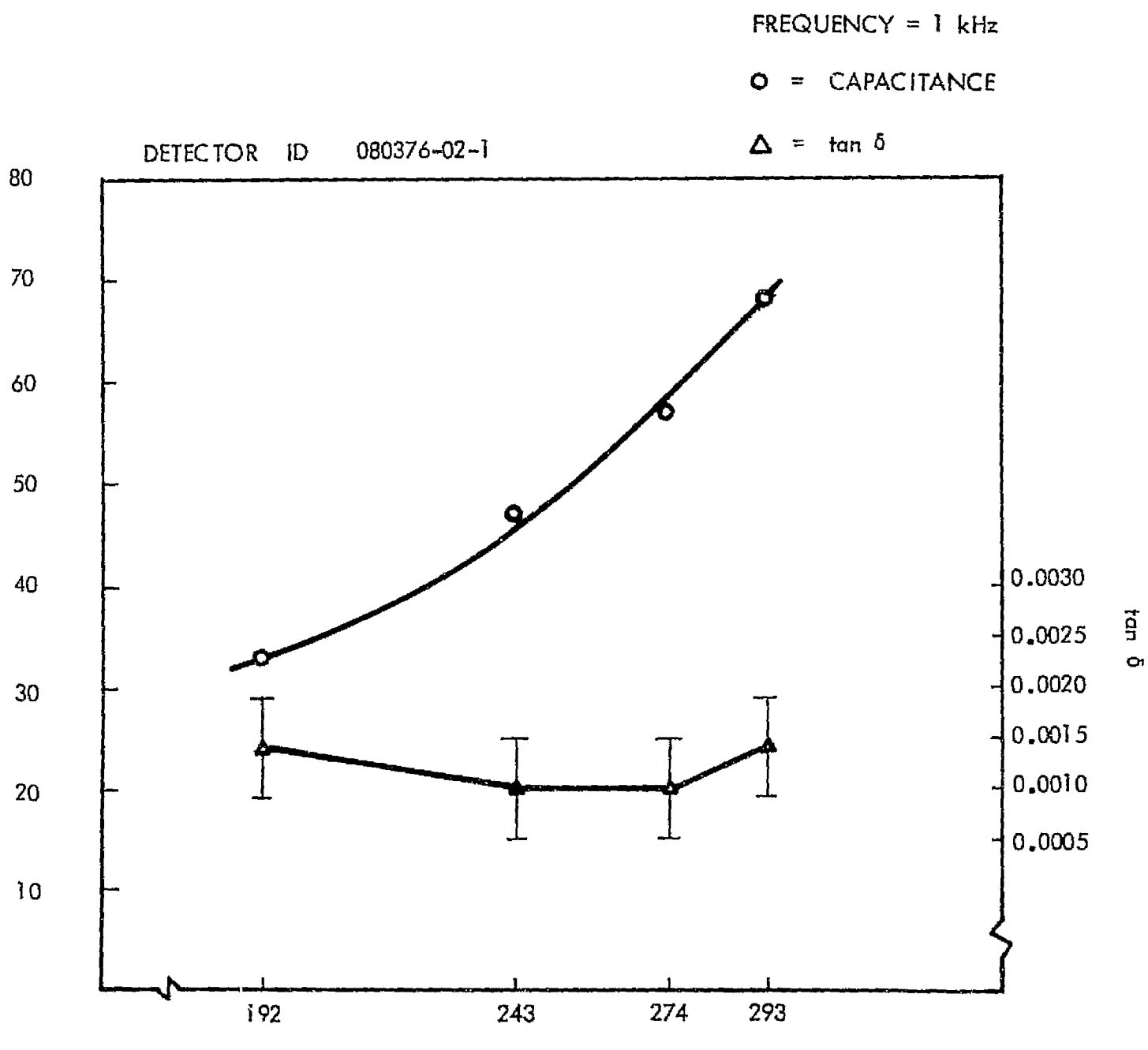

FIGURE 11 CAPACITANCE AND tan δ VERSUS TEMPERATURE FOR DETECTOR 080376-02-1, at 1 kHz

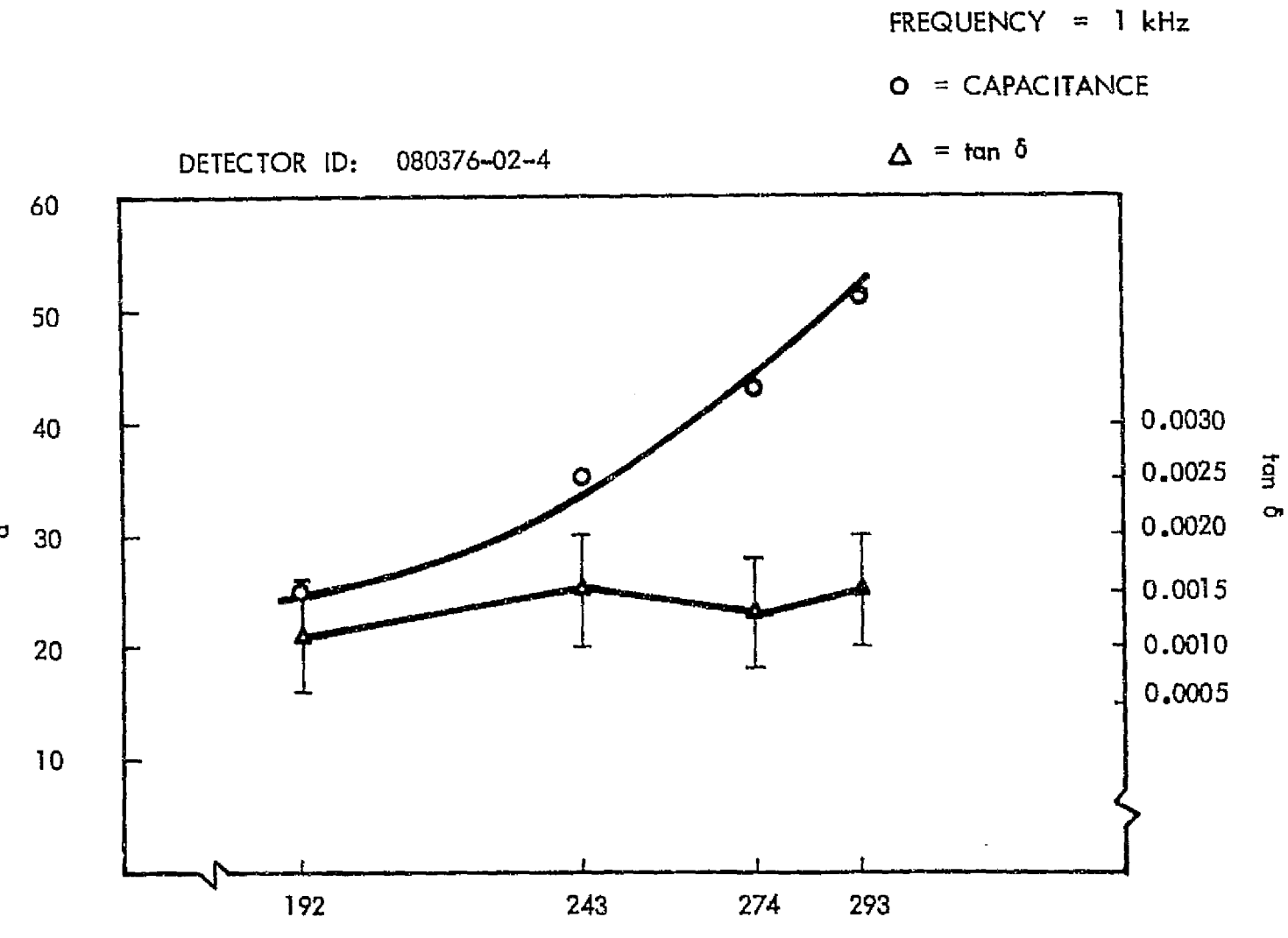

FIGURE 12 CAPACITANCE AND tan δ VERSUS TEMPERATURE FOR DETECTOR 080376-02-4, AT 1 kHz

5.0 DETECTOR READOUT CIRCUITRY

The detectors are mounted directly onto preamplfier boards containing a U423 JFET and a 1×10^{11} Ω load resistor. These preamplifier boards are then mounted onto the cold finger of a Cryogenics Associates IR-14 dewar. The pin connections for the detectors are shown in Figure 13. When the "Cap. (+)" pin is used in conjunction with the "Det.Gnd." pin for a given detector, the capacitance and tanδ of the device can be measured.

The biasing conditions for the JFET are shown in Figure 14. Referring to Figure 14, the gate of the JFET is biased at zero volt through the 10^{11} ohm load resistor across the detector. The n-channel JFET drain is biased at 5 volts positive with respect to the gate. The JFET is connected as a source-follower and its operating current is defined by the load resistor to be:

$$I_{DS} = \frac{-V_{ss} + V_s}{R_L}$$

where R_L is the source load resistor (100 K Ω). Using a relatively large V_{ss} compared to V_s, which is on the order of 1 volt makes the operating current I_{DS} nearly independent of variations in V_s from unit to unit. Also, a large R_L can be used for a large V_{ss}. Since the source-follower gain is given by:

$$G = \frac{g_m R_L}{1 + g_m R_L}$$

5.0 DETECTOR READOUT CIRCUITRY (cont'd)

where g_m is the JFET transconductance, a large R_L means a near unity gain independent of JFET parameters. This gives the advantage of not having to consider the JFET gain in detector noise and responsivity measurements.

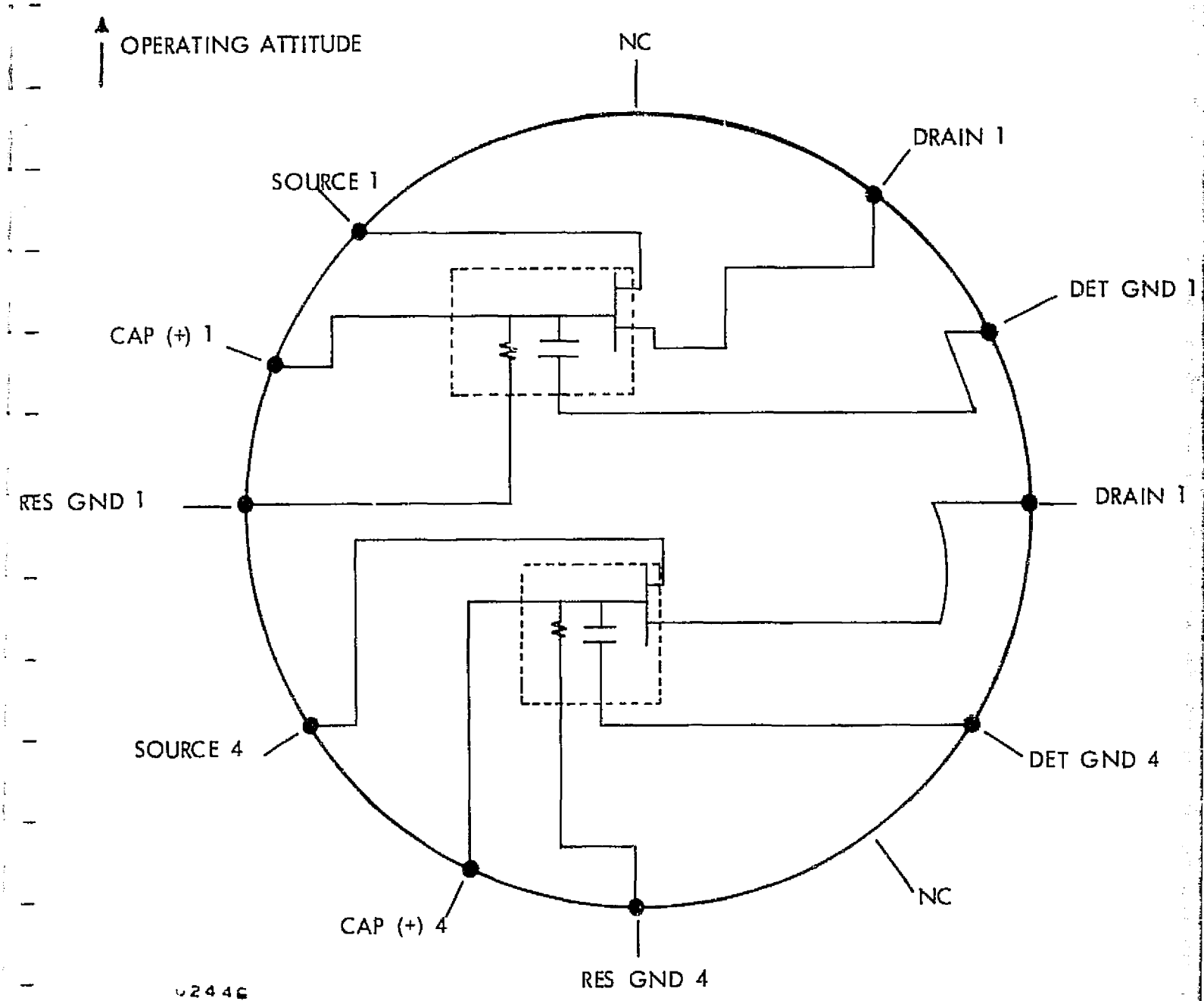

FIGURE 13 PIN CONNECTIONS FOR DEVICES 080376-02-1 and 080376-02-4, MOUNTED IN CRYOGENICS ASSOCIATES IR-14 DEWAR.

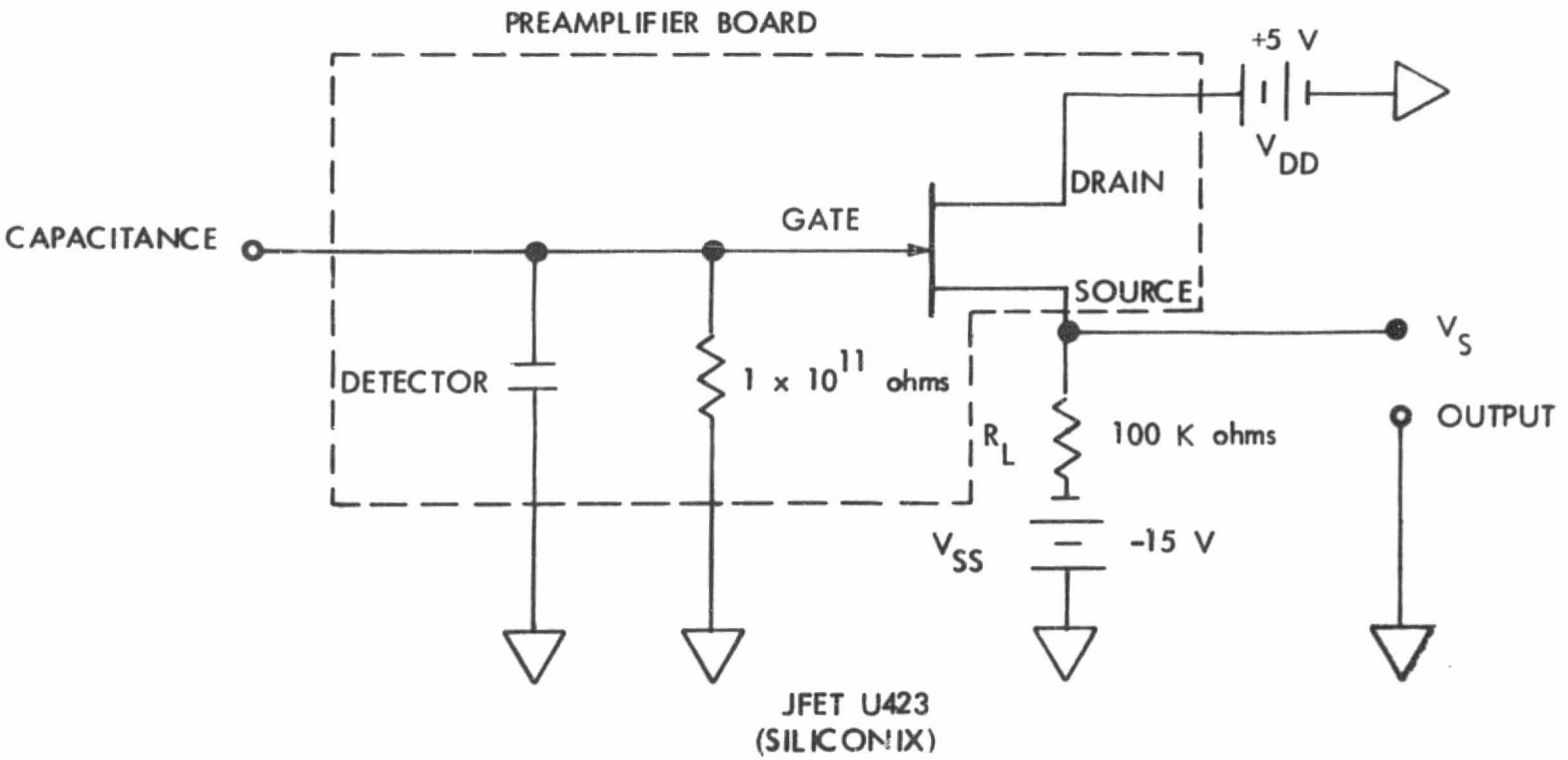

FIGURE 14 JFET PREAMPLIFIER BIASING AND READOUT CONNECTIONS

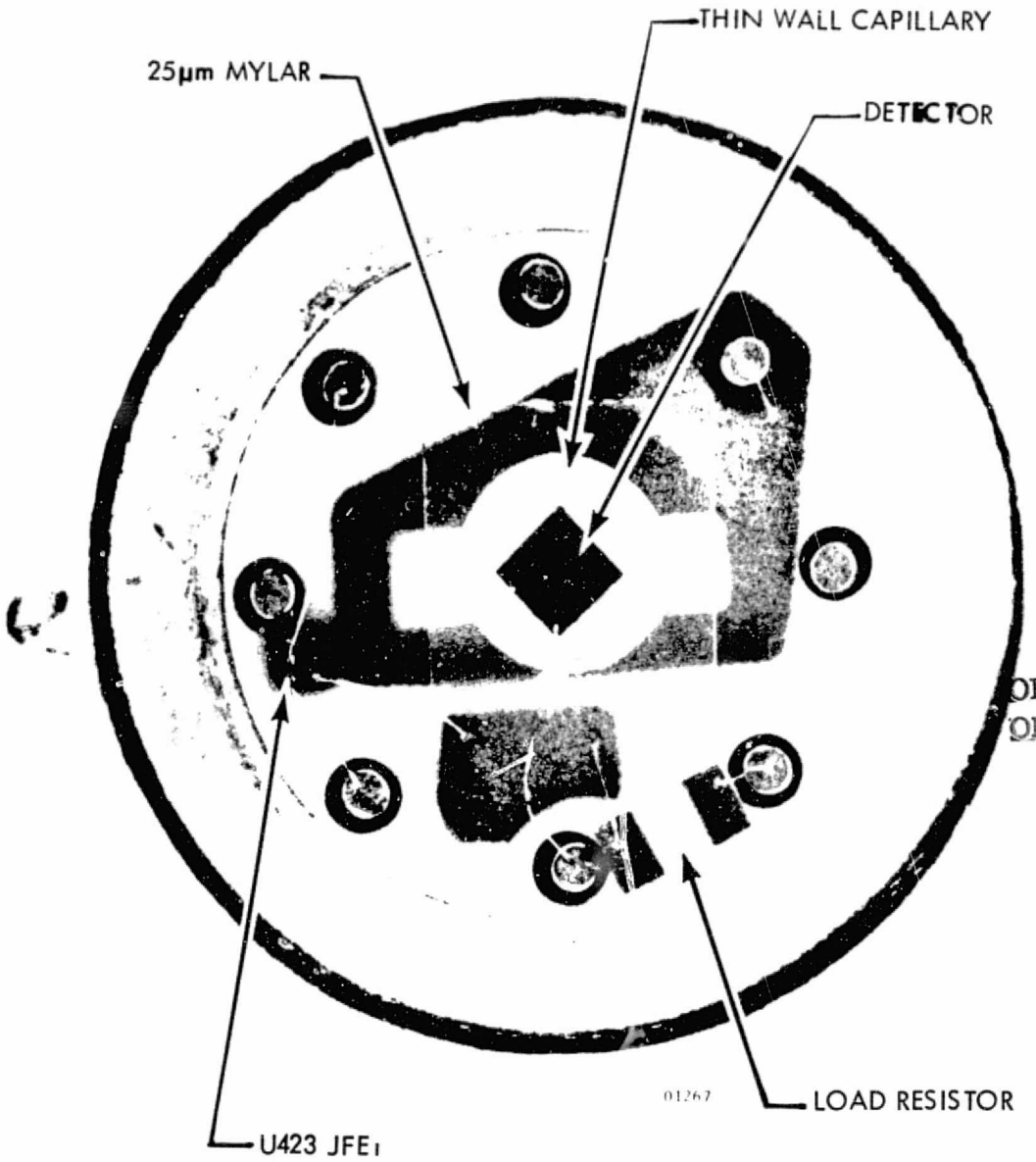

FIGURE 15 TOP VIEW OF A DETECTOR ASSEMBLY SIMILAR TO THOSE SHIPPED.

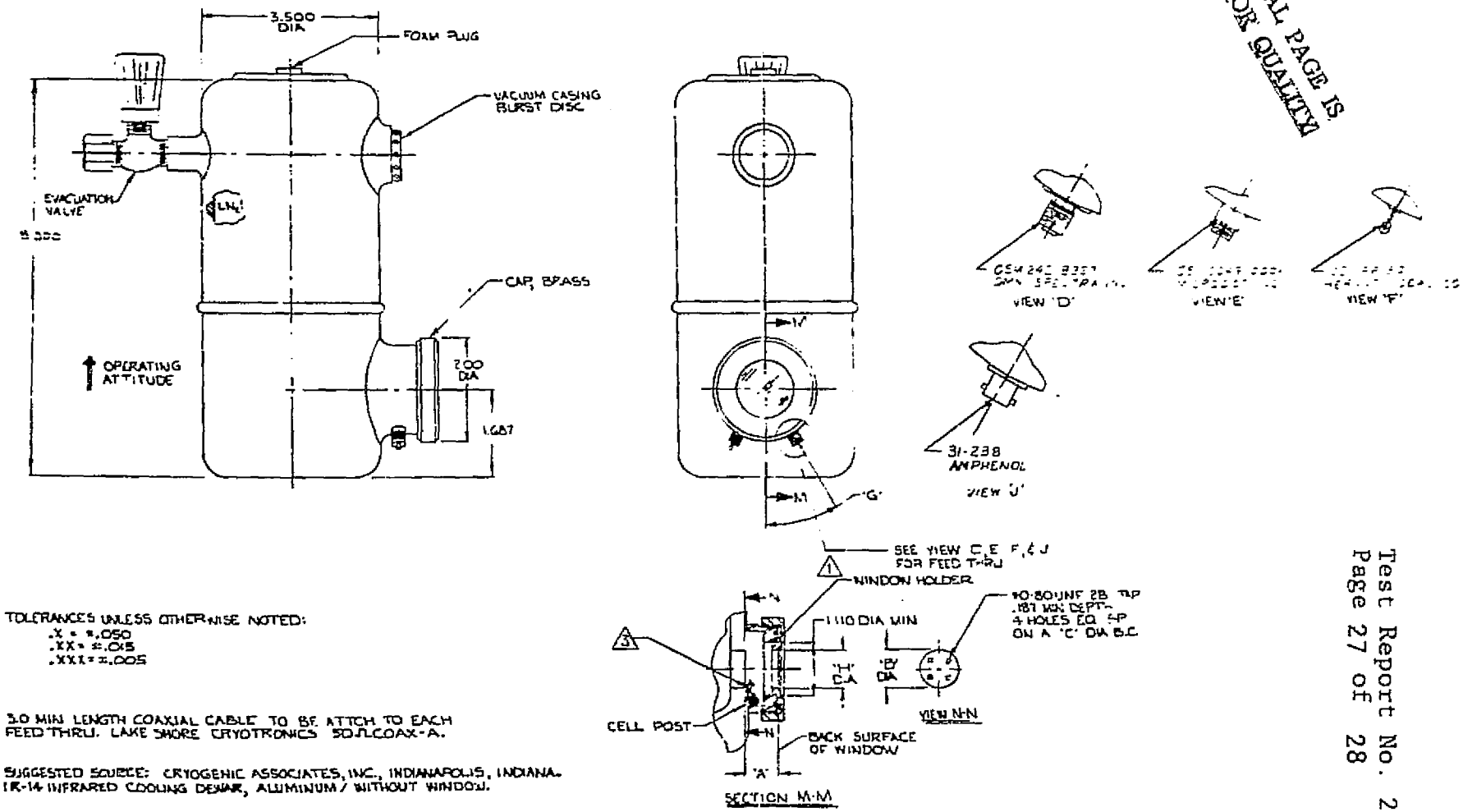

4. TOLERANCES UNLESS OTHERWISE NOTED:
   .X = ±.050
   .XX = ±.015
   .XXX = ±.005

3. 3.0 MIN LENGTH COAXIAL CABLE TO BE ATTCH TO EACH FEED THRU. LAKE SHORE CRYOTRONICS 50-1LCOAX-A.

2. SUGGESTED SOURCE: CRYOGENIC ASSOCIATES, INC., INDIANAPOLIS, INDIANA. IR-14 INFRARED COOLING DEWAR, ALUMINUM / WITHOUT WINDOW.

1. WINDOW HOLDER. (SEE TABLE) TO BE VENDOR SUPPLIED.

Figure 16 DETECTOR DEWAR SPECIFICATIONS

6.0 HANDLING PRECAUTIONS

Under no circumstances should the detector temperature be allowed to exceed 100°C.

Care should be taken to insure a good dewar vacuum ($\sim 1 \times 10^{-6}$ Torr) before using cryogens to cool the detectors. This will prevent moisture condensation on the detector surfaces and the dewar window. Since the dewar holding time for LN_2 is 24 hours, it is essential that measures are taken to allow the detectors to reach room temperature before releasing the vacuum in the dewar.

Caution should be observed not to subject the dewar to unnecessary jarring motions.

APPENDIX B

TEST REPORT NO. 22172-2

FOR

SBN INFRARED DETECTORS

(LK232A1, SN1; LK232A1, SN2; LK233A1, SN1)

Prepared for:

National Aeronautics and Space Administration
Langley Research Center
Hampton, Virginia 23365

Contract NAS1-14372

December 30, 1977

Prepared by:

J.W. Marciniec
Associate Research Engineer

J.C. Gelpey
Research Engineer

Approved by:

D.E. Marshall
Project Manager

Paul Nelson 1-9-78
Paul Nelson
Product Assurance

HONEYWELL
Electro-Optics Center
2 Forbes Road
Lexington, Massachusetts 02173

INTRODUCTION

This test report was prepared for the Electronic Devices Research Branch, NASA Langley Research Center, Hampton, Virginia under NASA contract NAS1-14372. The NASA Technical Representatives for this contract were Dr. Roger K. Crouch and Dr. James B. Robertson.

The strontium barium niobate (SBN) infrared detectors described in this test report were developed, fabricated and characterized at the Honeywell Electro-Optics Center in Lexington, Massachusetts.

The devices were fabricated by Mr. Brian Denley and Mr. Don Smith. The technical assistance of Mr. John Monahan in the testing of the devices is appreciated.

This test report describes performance data for five (5) strontium barium niobate ($Sr_{1-x}Ba_xNb_2O_6$ with $x = 0.5$) pyroelectric infrared detectors, each integrated with a matching JFET preamplifier and load resistor. Four of these detector/preamp/load resistor assemblies are mounted in metal dewars, with two assemblies per dewar, and the fifth assembly is mounted in a TO-5 header. Metal dewars were chosen to enable these developmental detectors to be characterized conveniently over the 193-296° K temperature range. These detector units were delivered to NASA Langley Research Center in December, 1977.

TABLE OF CONTENTS

1.0 DESCRIPTION OF DETECTORS

Type of Detector	Pyroelectric
Material	$Sr_{1-x}Ba_xNb_2O_6$; x = 0.5
Window	Ge, Thickness = 40 mil Antireflection coated
JFET	U423, Siliconix

2.0 DETECTOR PARAMETERS AND TESTS CONDUCTED

A summary of the characteristics and performance of the five (5) SBN pyroelectric detectors is contained in Table I.

Table 1

PHYSICAL PARAMETERS AND PERFORMANCE OF DETECTORS

UNIT	DETECTOR NUMBER	DETECTOR SIZE		DIELECTRIC PROPERTIES			DETECTIVITY VERSUS TEMPERATURE	
		ACTIVE AREA (10^{-3} cm^2)	THICKNESS (μm)	FREQUENCY (kHz)	T = 23° C CAPACITANCE (pF)	T = 23° C tan δ	TEMPERATURE (K)	DETECTIVITY (FREQUENCY=12 Hz) (10^8 cm-Hz$^{\frac{1}{2}}$/watt)
LK232A1, SN1 (Dewar 1)	SBN-3	3.82	15	0.1 1 10	67 64 63	0.013 0.009 0.004	296 273 243	5.8 8.8 11.1
WINDOW APERTURE =7/8"	SBN-8	4.52	25	0.1 1 10	71 70 69	0.003 0.002 0.001	296	7.2
LK232A1, SN2 (DEWAR 2)	SBN-6	2.88	25	0.1 1 10	36 35 34	0.003 0.002 0.001	296 273 243 193	6.6 6.8 6.8 3.8
WINDOW APERTURE =7/8"	SBN-12	4.13	22	0.1 1 10	50 49 49	----- 0.001 -----	296 273 243 193	8.5 6.8 7.4 4.7
LK233A1, SN1 (TO-5 Header) WINDOW APERTURE =5/32"	SBN-13	4.58	22	0.1 1 10	59 58 56	0.002 ----- -----	296	3.4

3.0 MEASUREMENT CONDITIONS

3.1 Physical Parameters

Blackbody Temperature (T_{BB})	500 K
Blackbody Aperture (d_A)	0.254 cm
Background Temperature (T_A)	296 K
Stefan-Boltzmann Constant (σ)	5.67×10^{-12} W/cm^2 °K
Detector to Orifice Distance (d)	15 cm
Chopping Frequency	1.2 - 240 Hz
Sine to RMS Conversion Factor (C)	0.437
Noise Bandwidth (Δ f)	1 Hz
Emissivity ϵ: Blackbody, Chopper	1.0
Window Transmittance Factor (F)	0.8

3.2 Flux Density (H_{BB}) at Detector

$$H_{BB} = \epsilon\sigma \left(T_{BB}^4 - T_A^4\right) \frac{d_A^2}{4d^2} \; C \cdot F \; (W/cm^2)$$

$$H_{BB} = 7.8 \times 10^{-6} \; (\pm \; 1 \times 10^{-6}) \; W/cm^2$$

3.3 Blackbody Responsivity (R_{BB})

$$R_{BB} = \frac{V_{sig}}{H_{BB} \; A_d} \quad (V/W)$$

3.4 Blackbody Detectivity (D^*_{BB})

$$D^*_{BB} = \frac{R_{BB}}{V_n} \cdot \sqrt{A_d} \quad (cm \sqrt{Hz} \; /W)$$

3.5 Window Transmittance Factor(F)

The calculation of the Window Transmittance Factor (F) is as follows. Due to the antireflection coating, the surface reflection (R) is only 6%. However, the window transmittance begins to cutoff at ~15.5 μm. For a 500 K blackbody, a 15% loss of energy (W_L) results. This can be expressed as:

$$F = (1-R)(1-W_L) = (1-0.06)(1-0.15) = 0.8$$

The responsivity and noise measurements were made using a Spectral Dynamics Corporation Model SD335 Real Time Analyzer, with preamplification by a Honeywell and a Princeton Applied Research Model 113 preamplifier combination.

The plotted responsivity and detectivity data includes the window transmittance factor, thus the data is normalized to the detector surface.

The cryogenics used for the low temperature measurements were:

Ice Water - 273 K

Freon 12 - 243 K

Freon 13 - 193 K

4.0 TEST RESULTS

4.1 SBN-3 Test Results

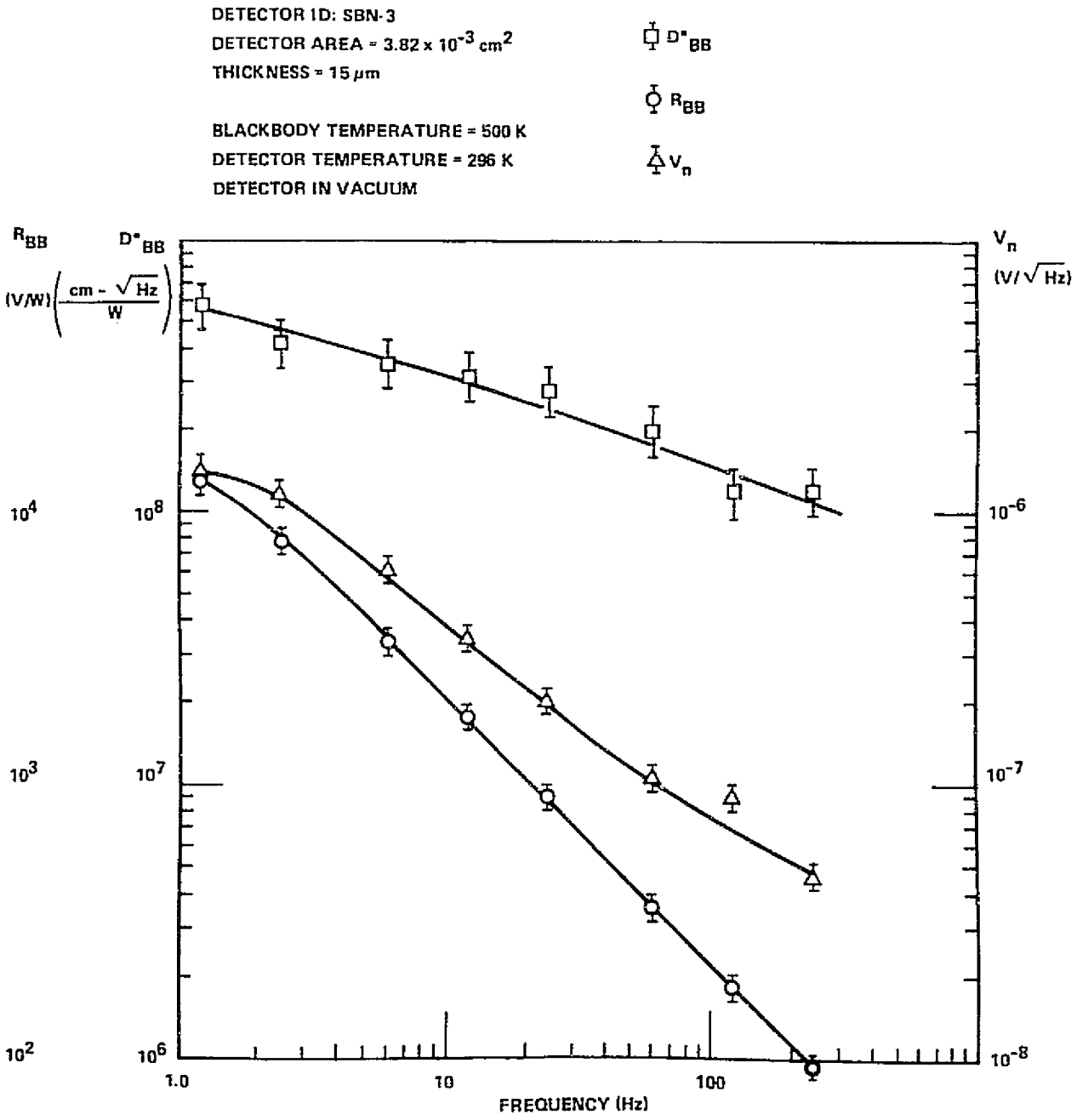

Figure 1 DETECTOR PERFORMANCE, SBN-3, 296 K

DETECTOR ID: SBN-3
DETECTOR AREA = $3.82 \times 10^{-3} cm^2$
THICKNESS = 15 μm

BLACKBODY TEMPERATURE = 500 K
DETECTOR TEMPERATURE = 273 K
DETECTOR IN VACUUM

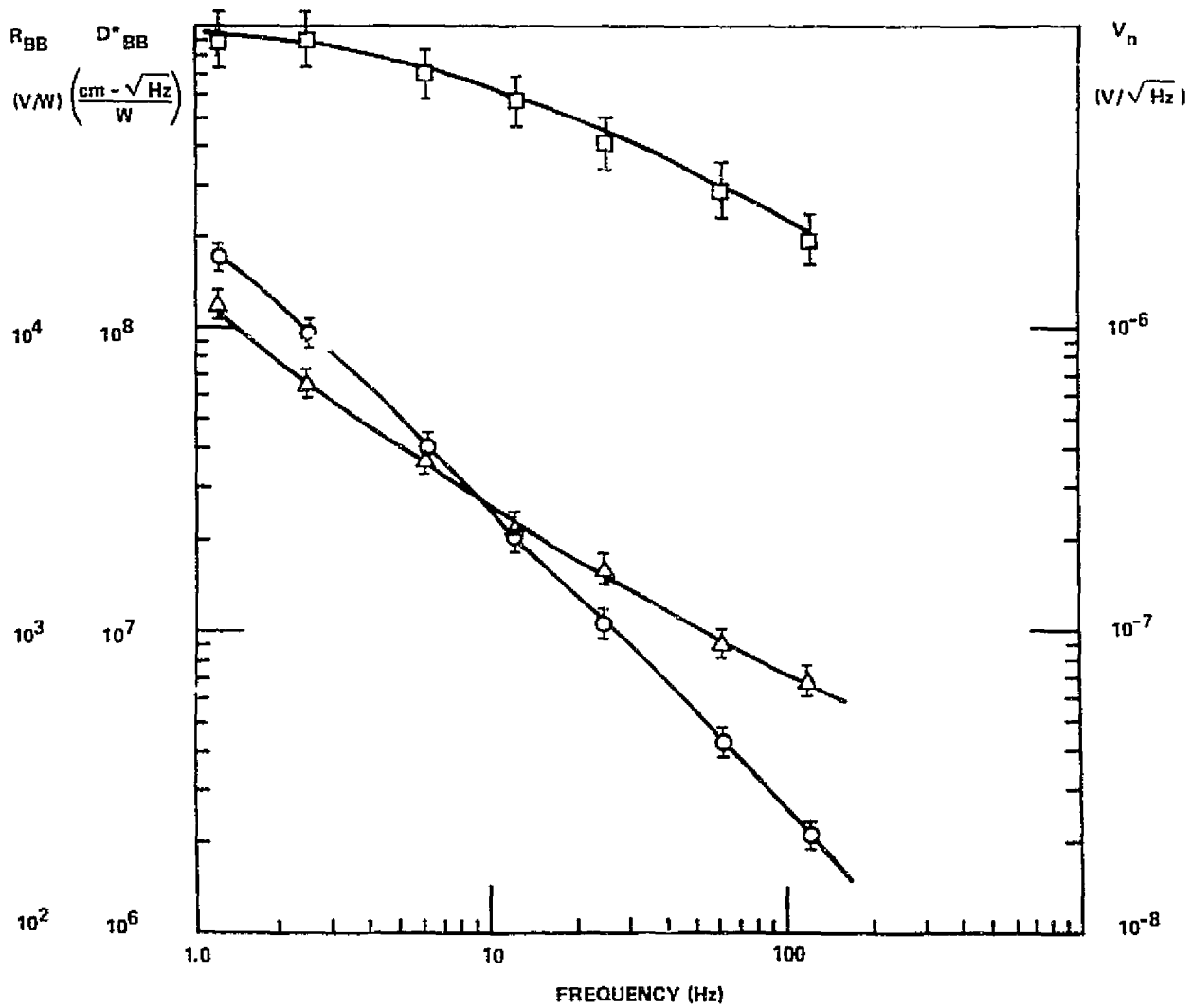

Figure 2 DETECTOR PERFORMANCE, SBN-3, 273 K

Detector ID: SBN-3
Detector Area = 3.8×10^{-3} cm^2
Thickness = 15 μm

Blackbody Temperature = 500 K
Detector Temperature = 243 K
Detector in Vacuum

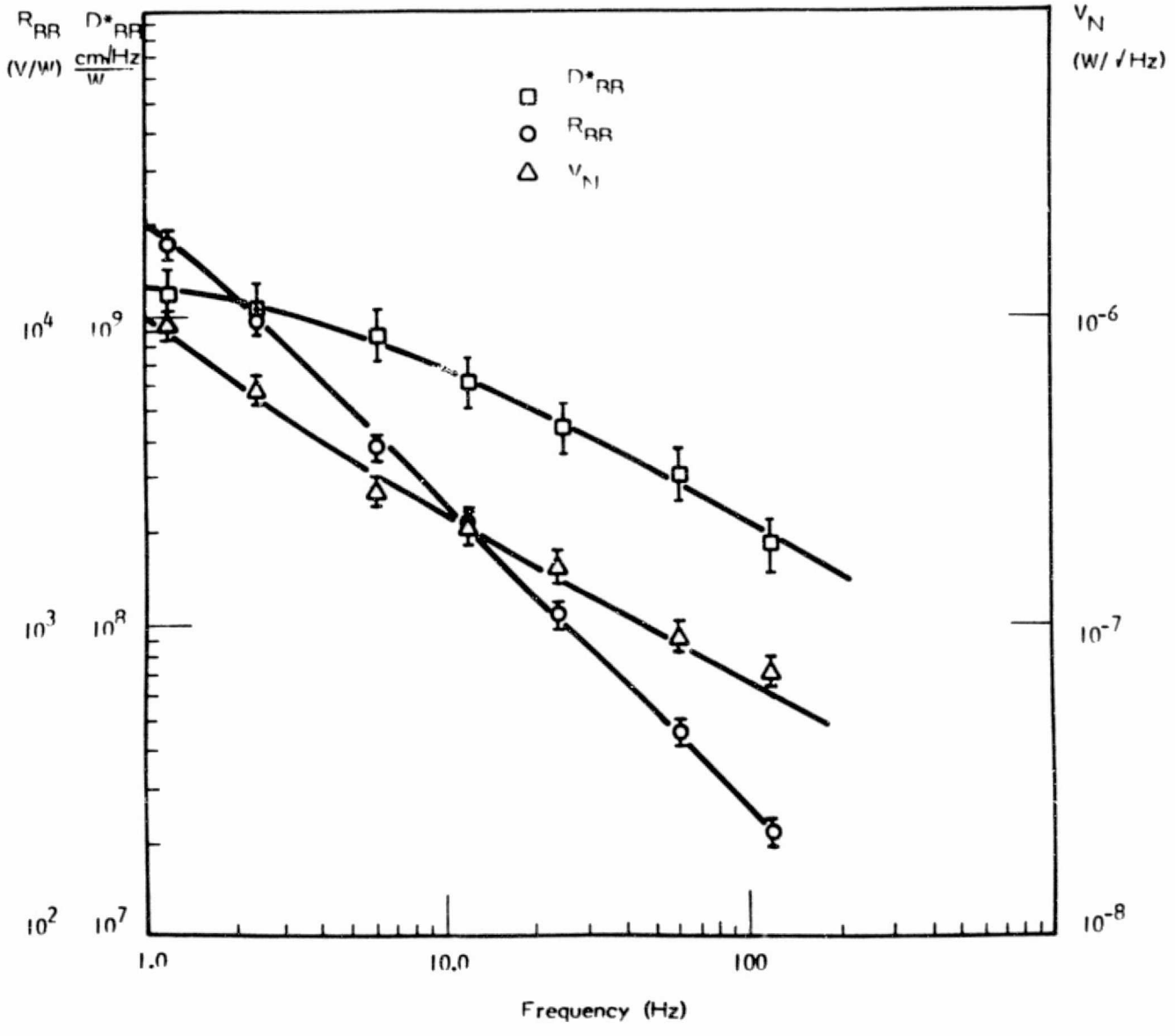

Figure 3 DETECTOR PERFORMANCE, SBN-3, 243 K

4.2 SBN-6 Test Results

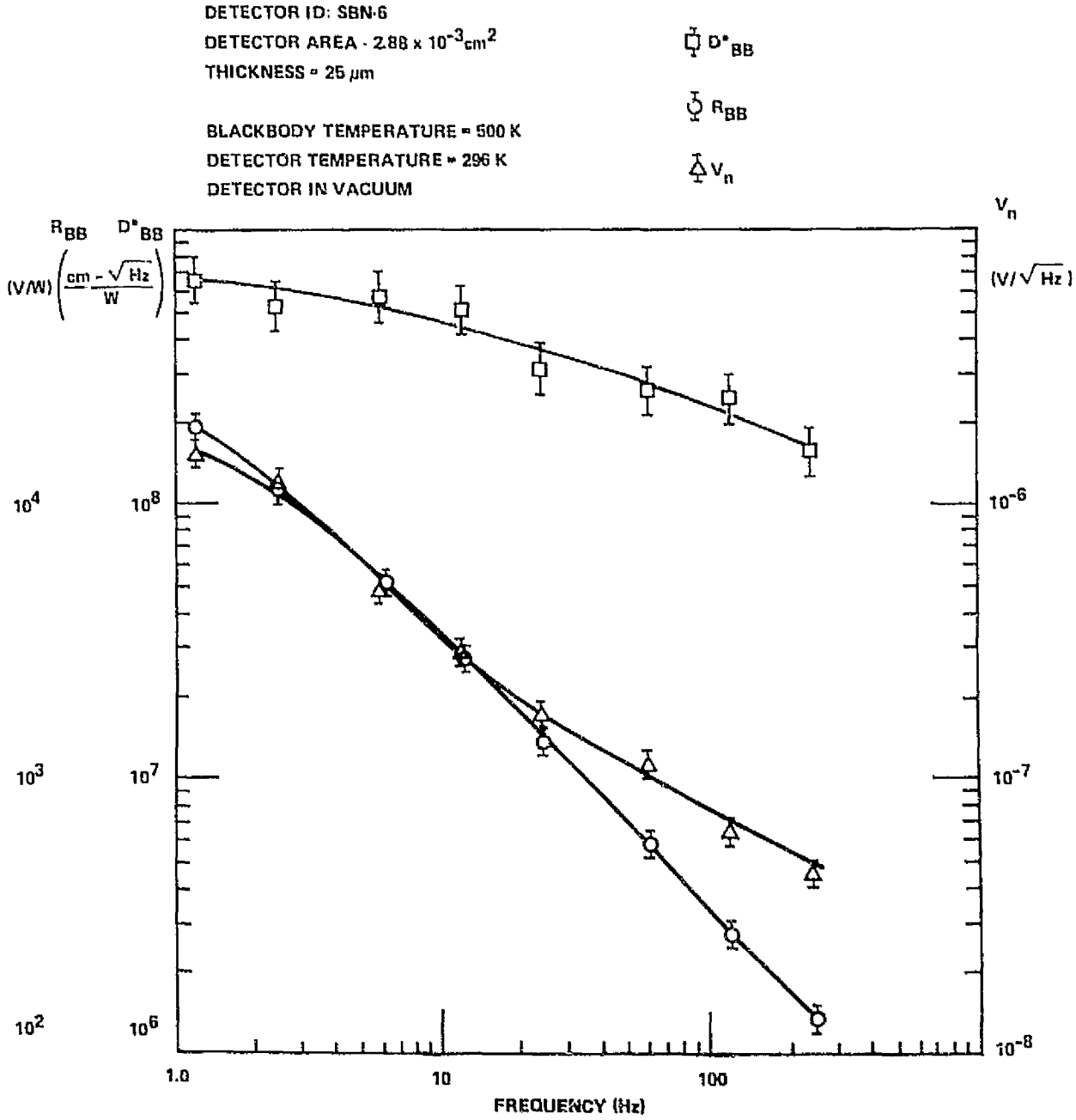

Figure 4 DETECTOR PERFORMANCE, SBN-6, 296 K

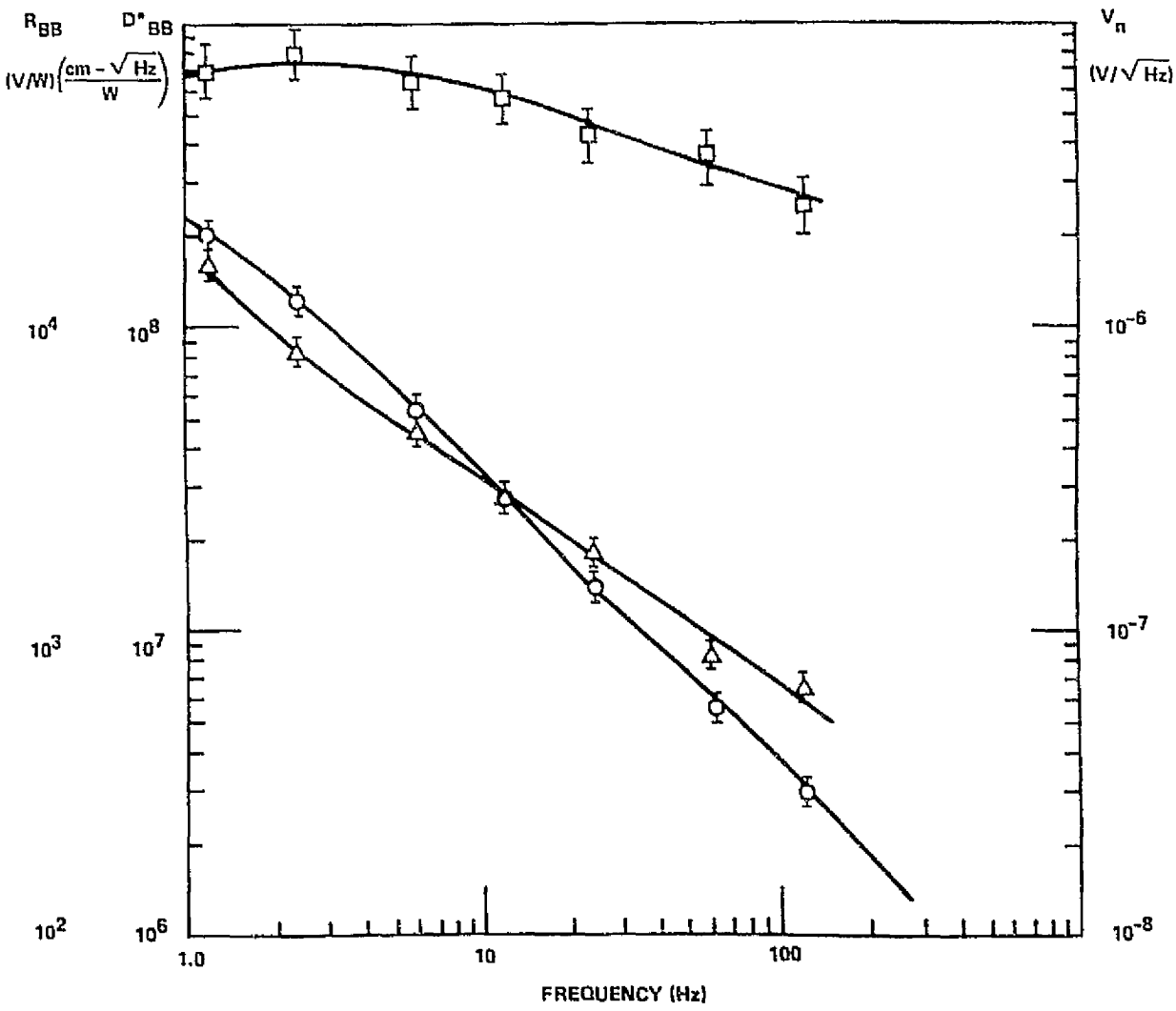

Figure 5 DETECTOR PERFORMANCE, SBN-6, 273 K

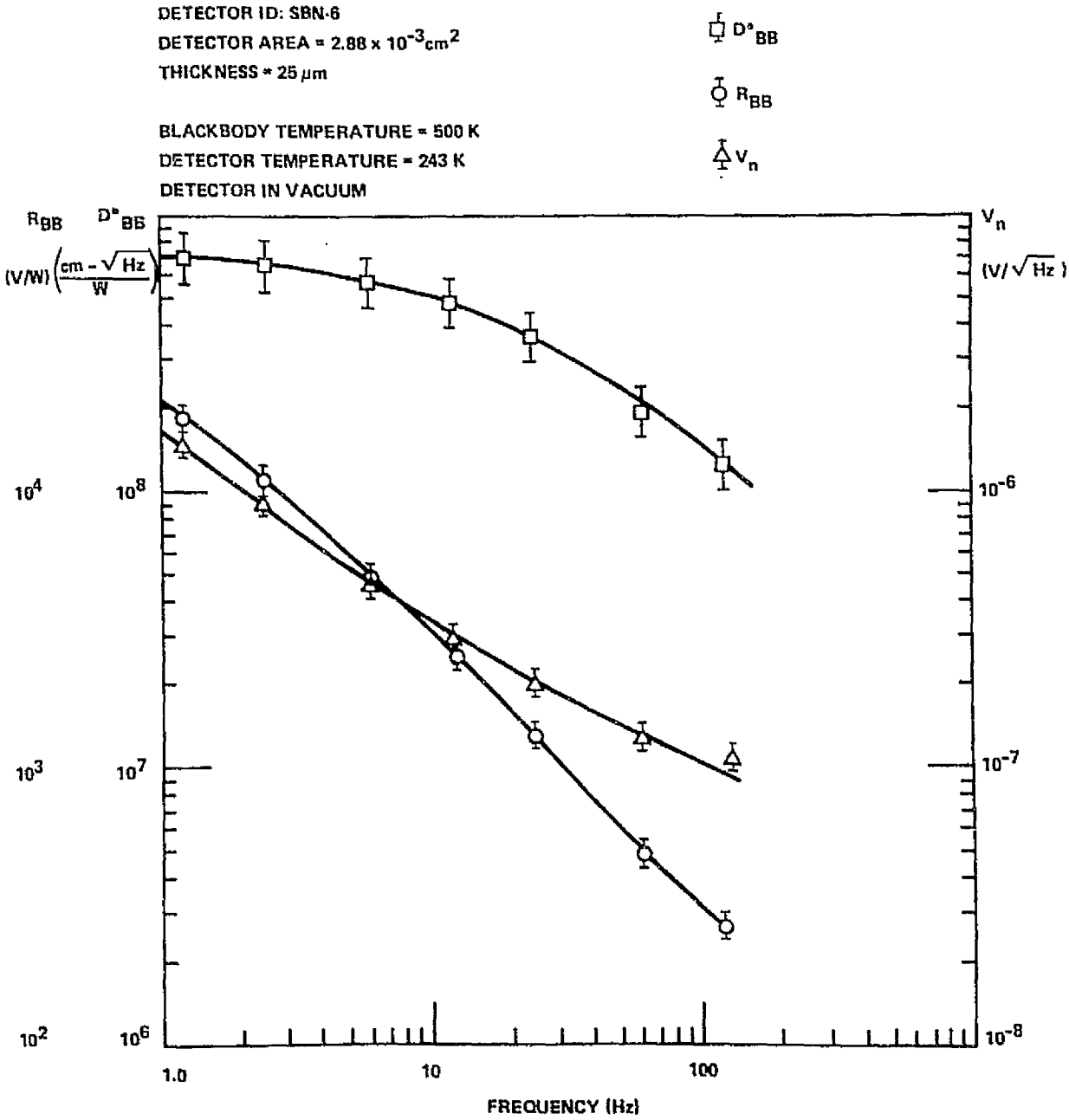

Figure 6 DETECTOR PERFORMANCE, SBN-6, 243 K

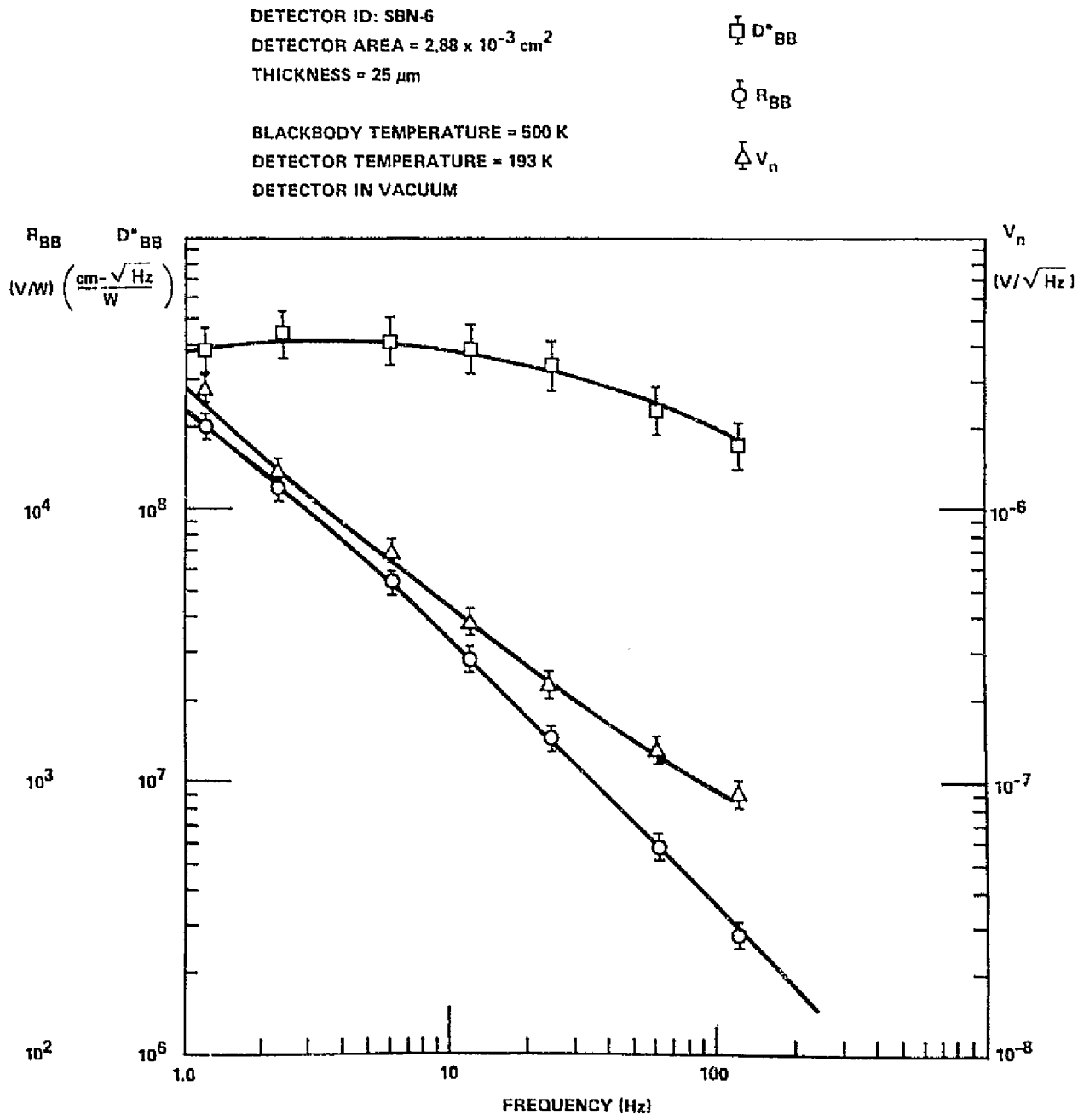

Figure 7 DETECTOR PERFORMANCE, SBN-6, 193 K

4.3 SBN-8 Test Results

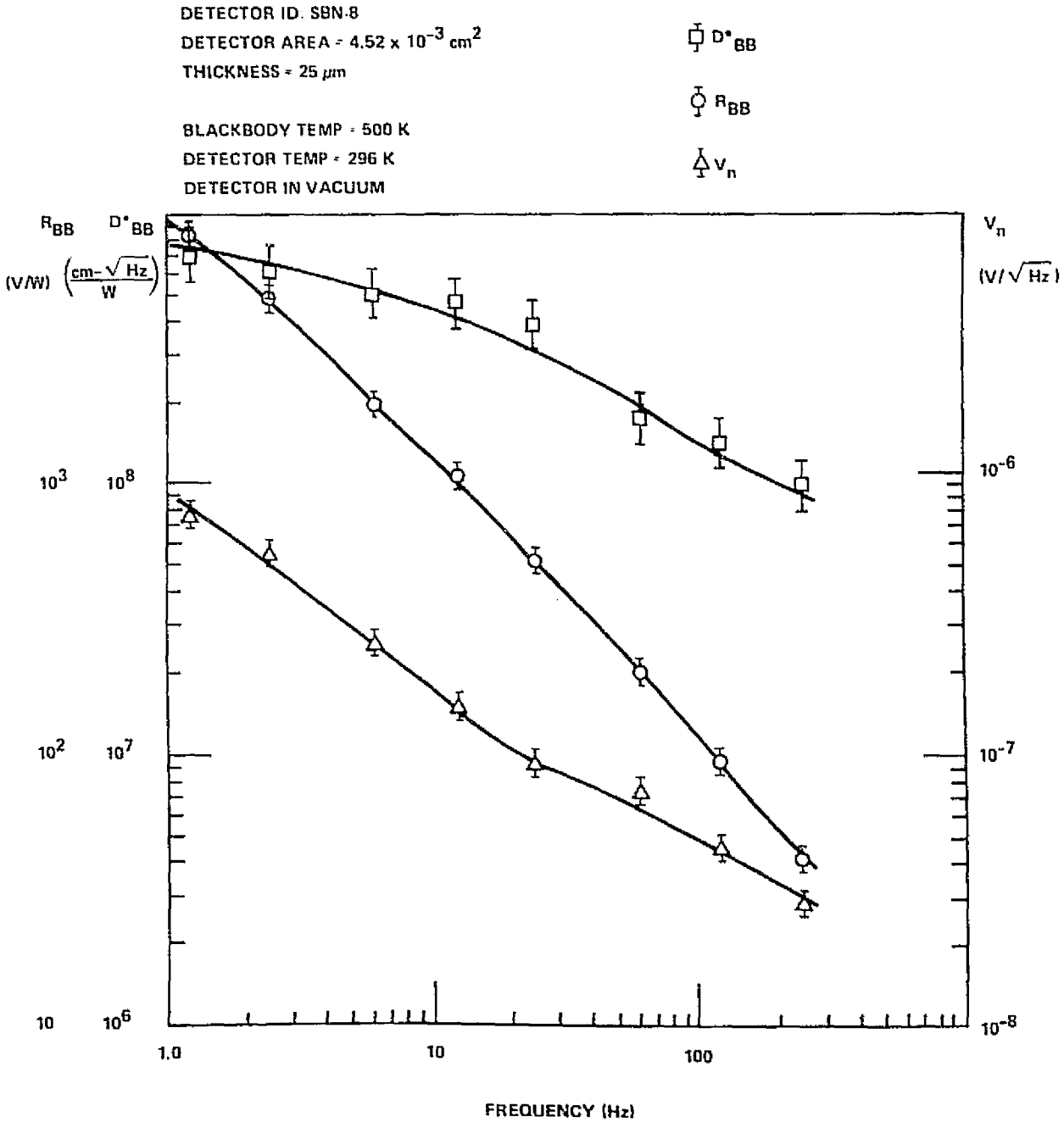

Figure 8 DETECTOR PERFORMANCE, SBN-8, 296 K

4.3 SBN-12 Test Results

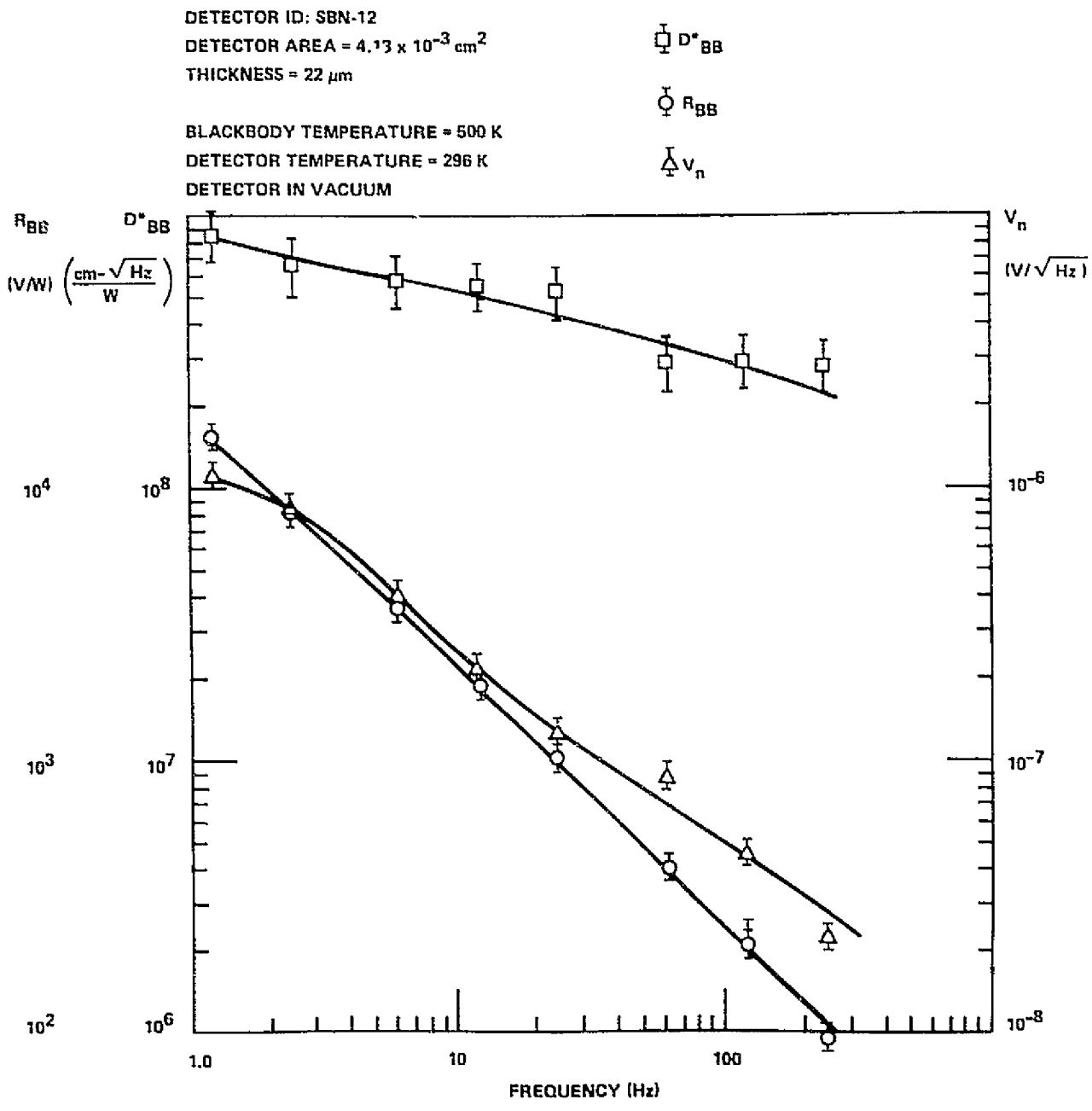

Figure 9 DETECTOR PERFORMANCE, SBN-12, 296 K

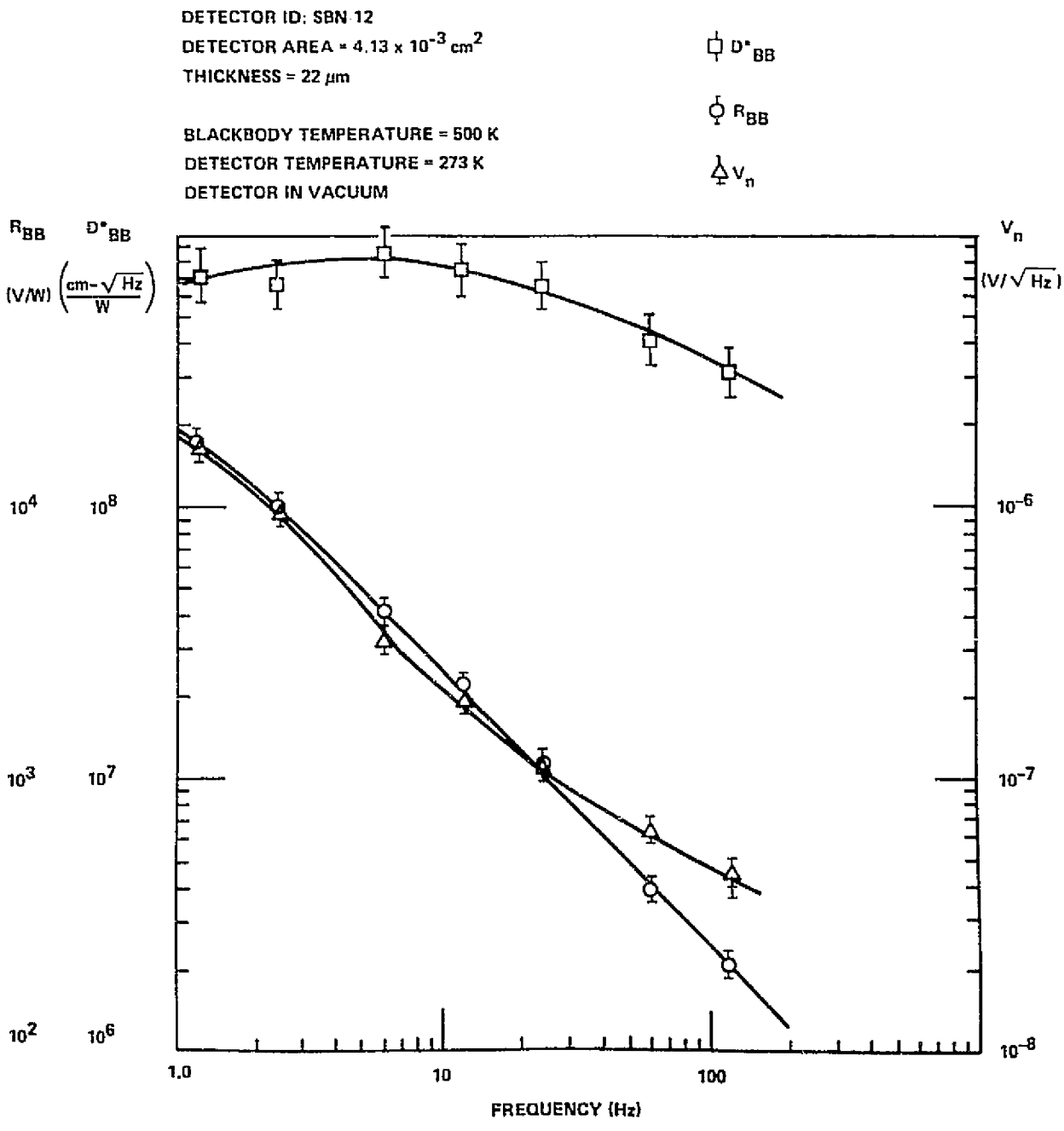

Figure 10 DETECTOR PERFORMANCE, SBN-12, 273 K

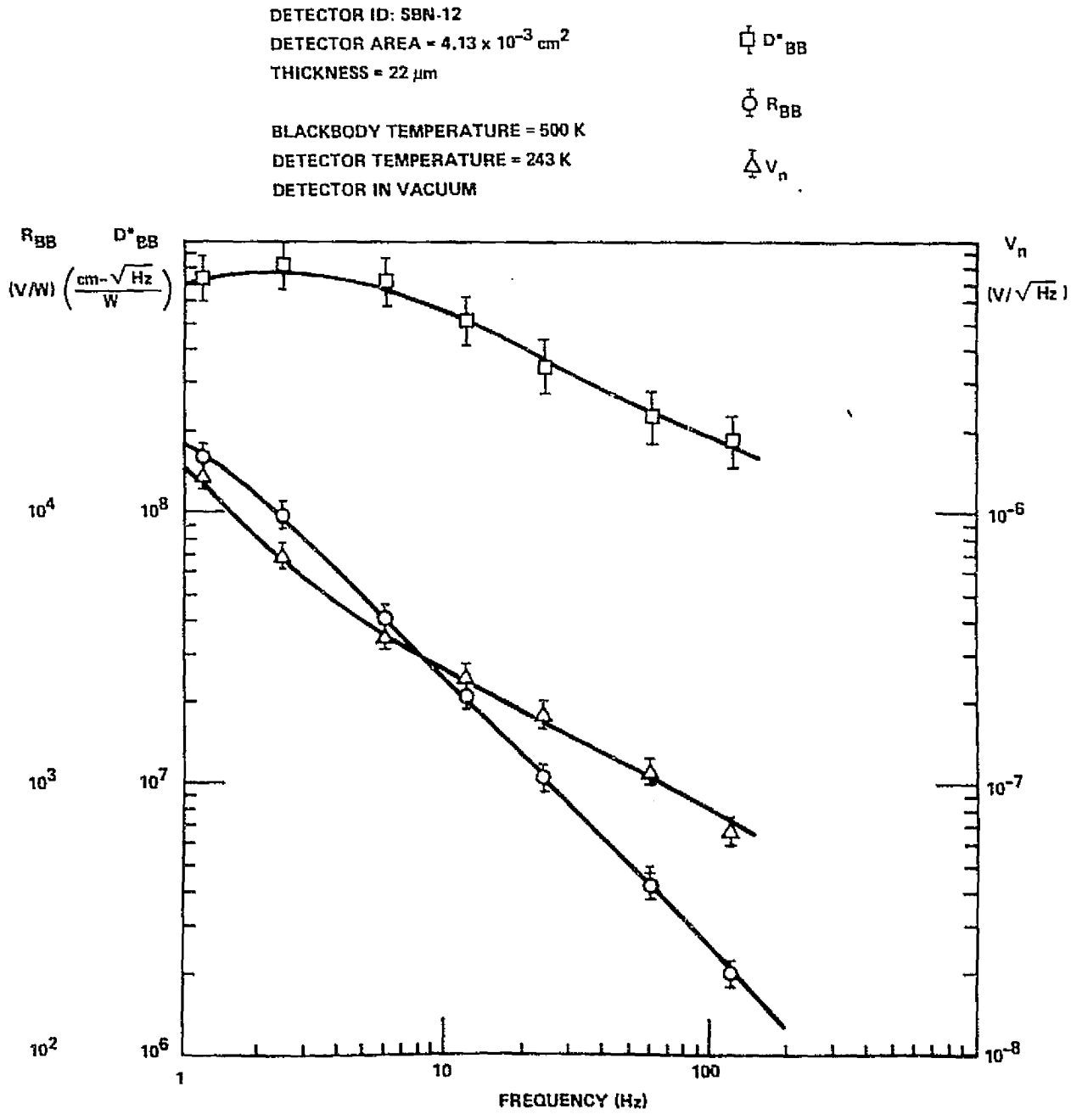

Figure 11 DETECTOR PERFORMANCE, SBN-12, 243 K

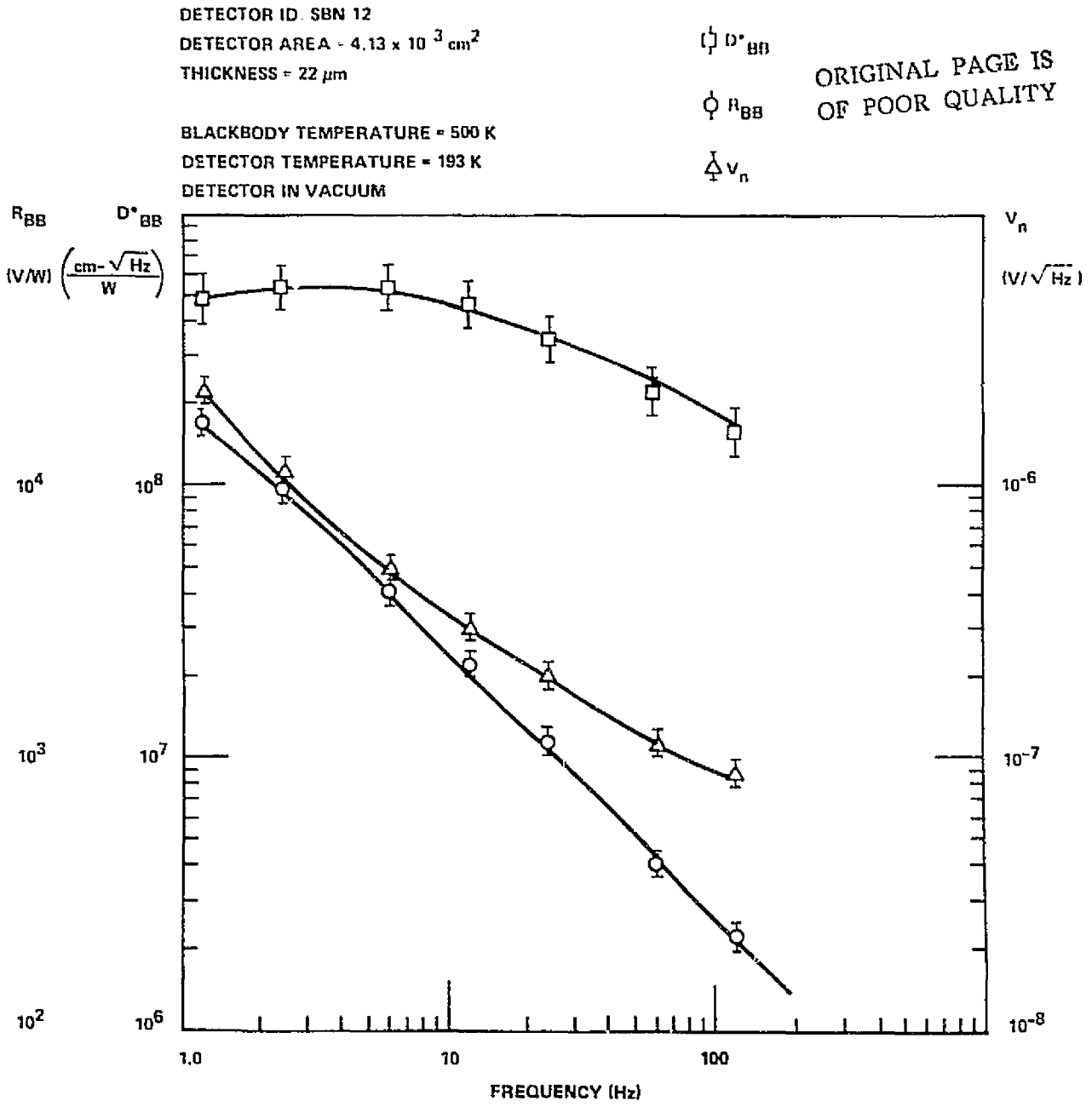

Figure 12 DETECTOR PERFORMANCE, SBN-12, 193 K

4.5 SBN-13 Test Results

Detector ID: SBN-13
Detector Area = 4.58×10^{-3} cm^2
Thickness = 22 μm

Blackbody Temperature = 500K
Detector Temperature = 296K
TO-5 CAN

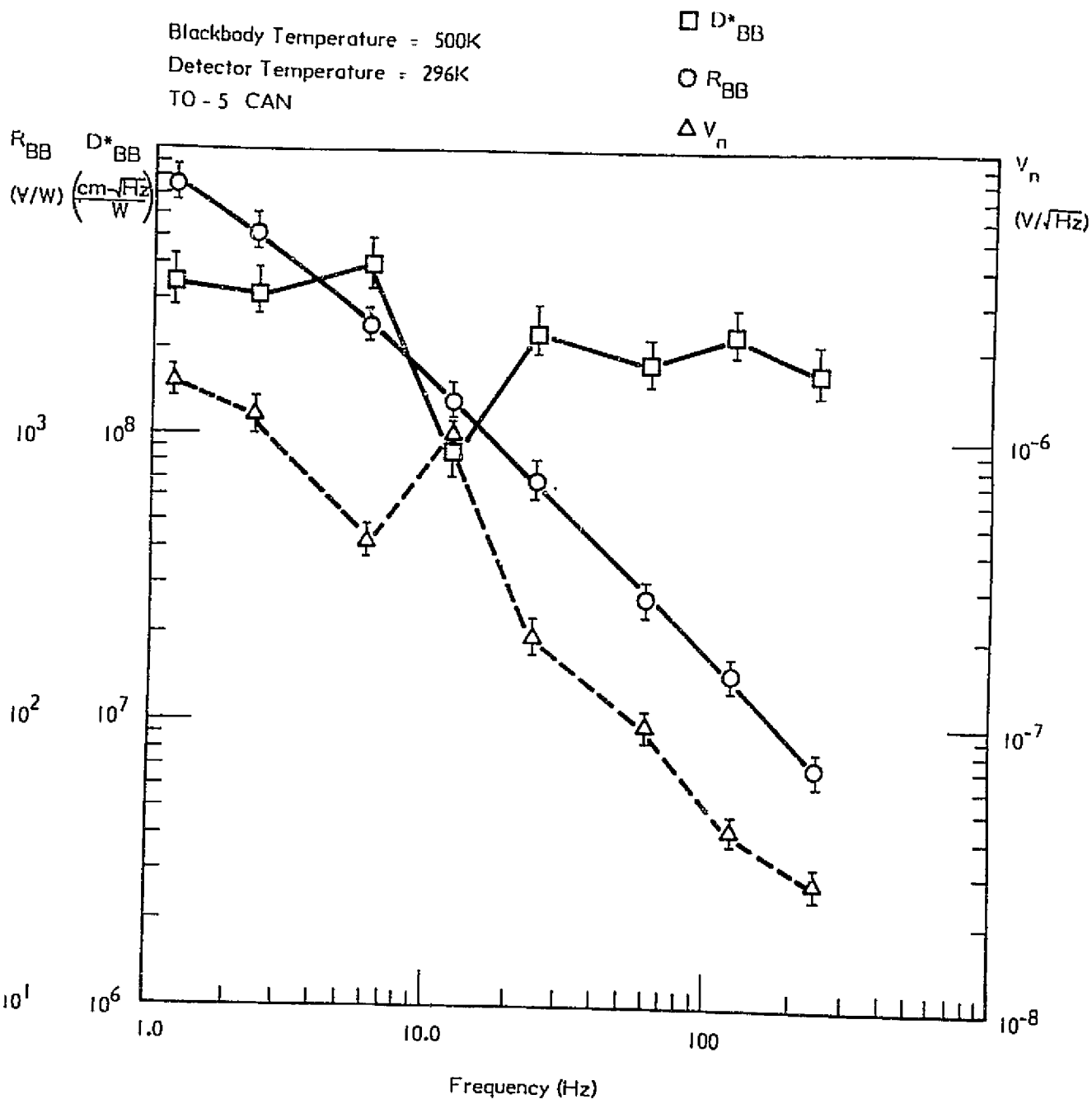

Figure 13 DETECTOR PERFORMANCE, SBN-13, 296 K

4.6 Summary of Detector Performances as a Function of Temperature for SBN-3, SBN-6, and SBN-12

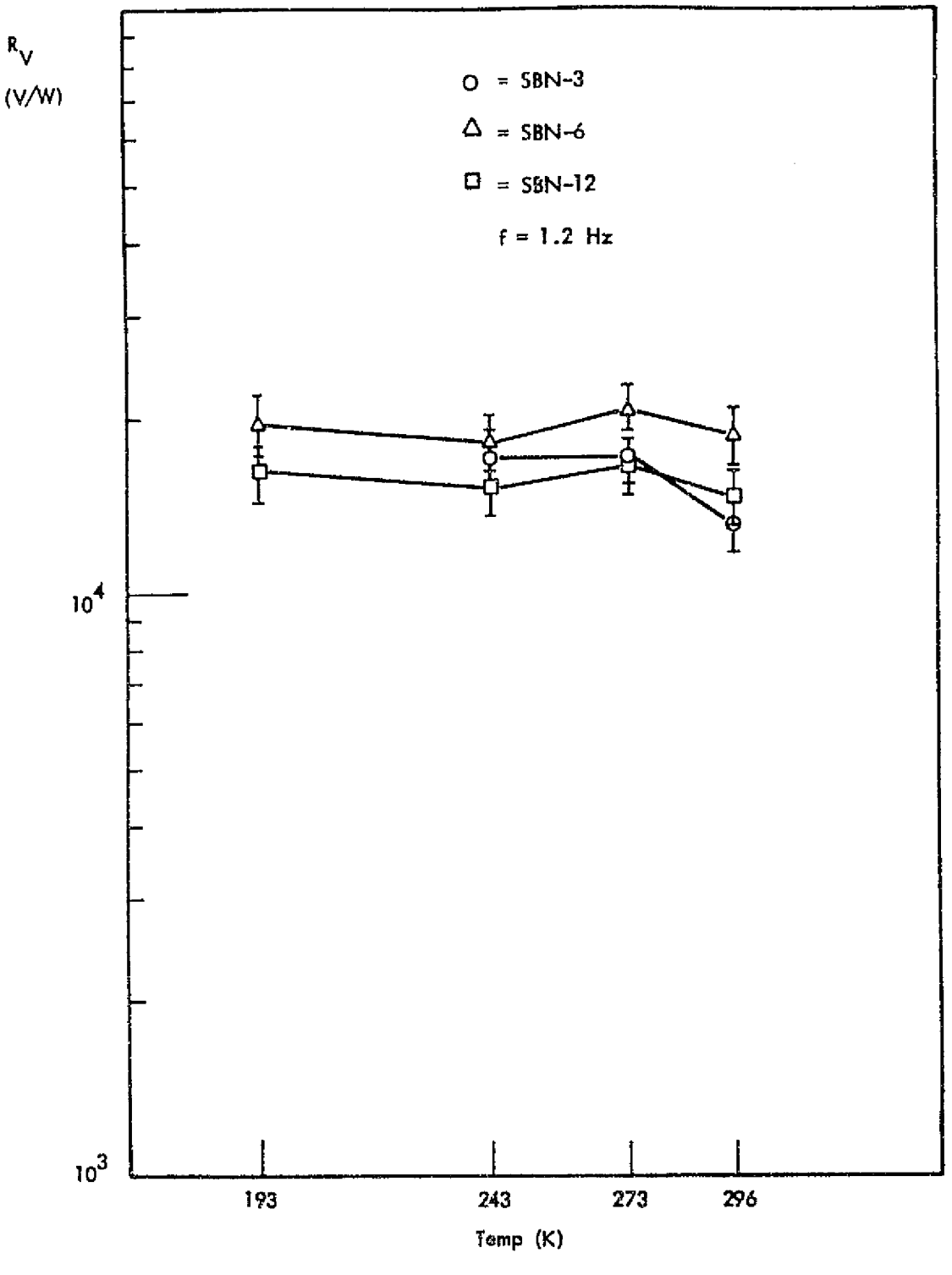

Figure 14 DETECTOR VOLTAGE RESPONSIVITY AT 1.2 Hz AS A FUNCTION OF TEMPERATURE FOR DETECTORS SBN-3, SBN-6, AND SBN-12

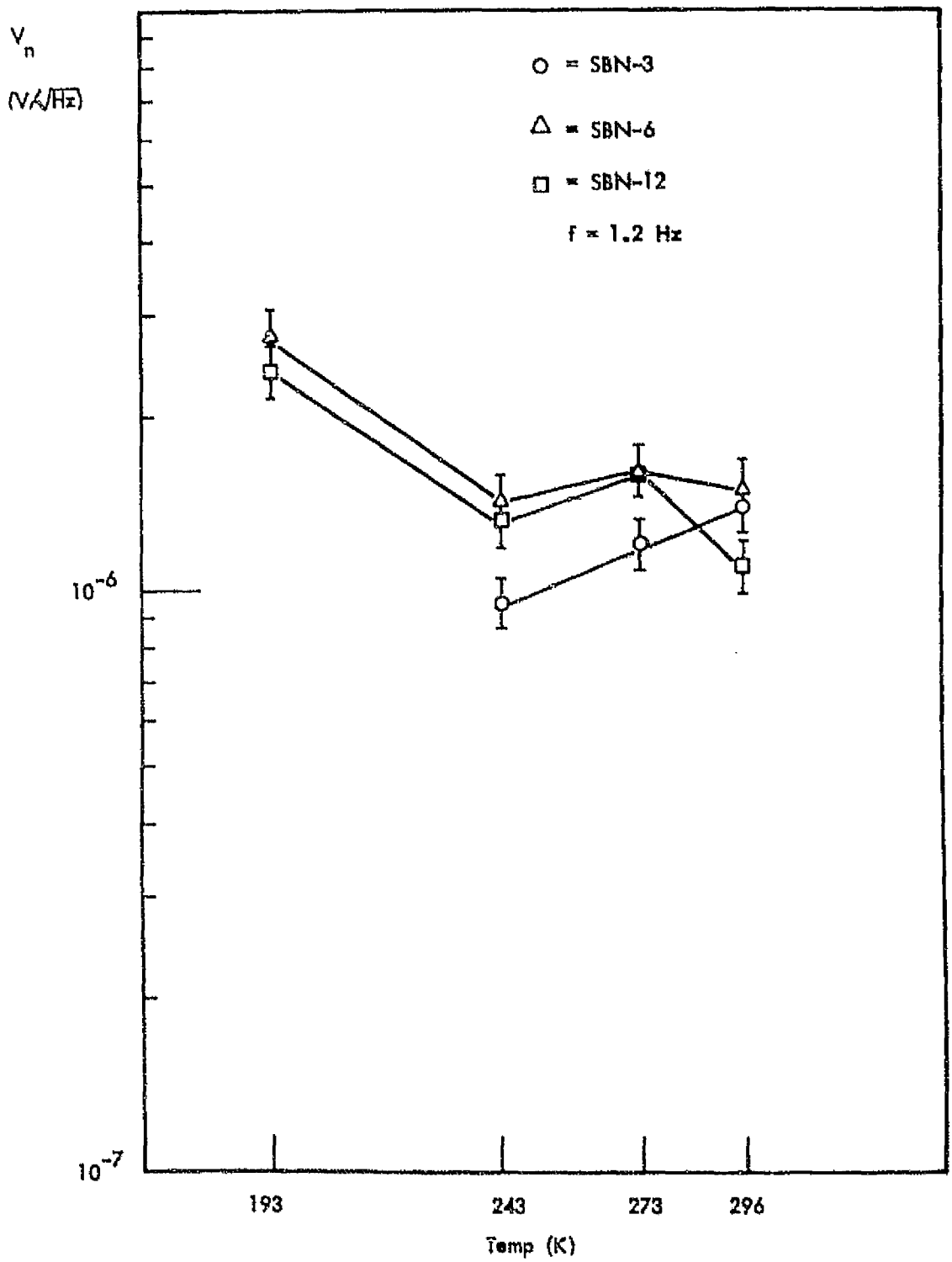

Figure 15 DETECTOR NOISE AT 1.2 Hz AS A FUNCTION OF TEMPERATURE, FOR DETECTORS SBN-3, SBN-6, AND SBN-12

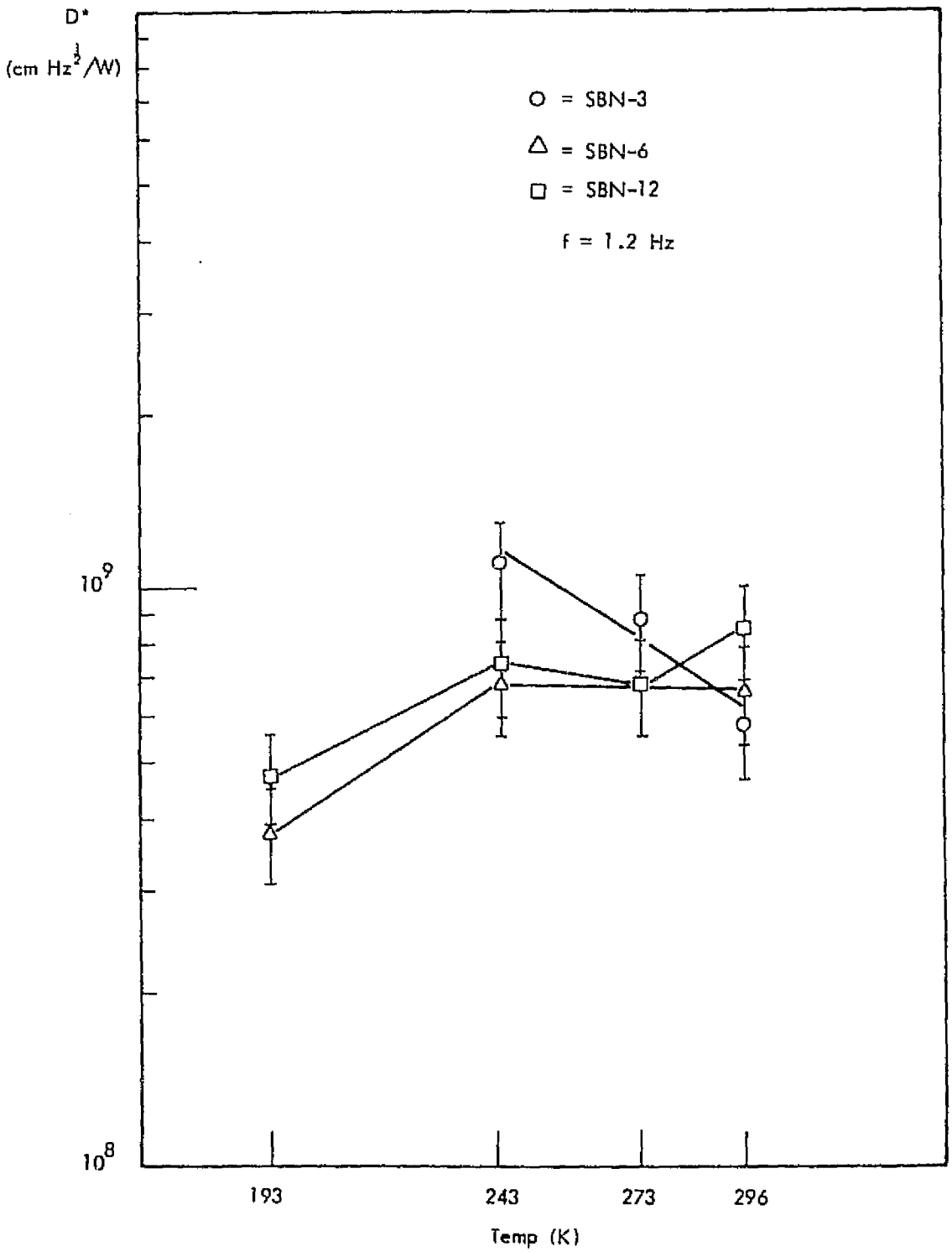

Figure 16 DETECTOR DETECTIVITY AT 1.2 Hz AS A FUNCTION OF TEMPERATURE, FOR DETECTORS SBN-3, SBN-6 AND SBN-12

4.7 Capacitance and tanδ vs. Temperature

Test Results

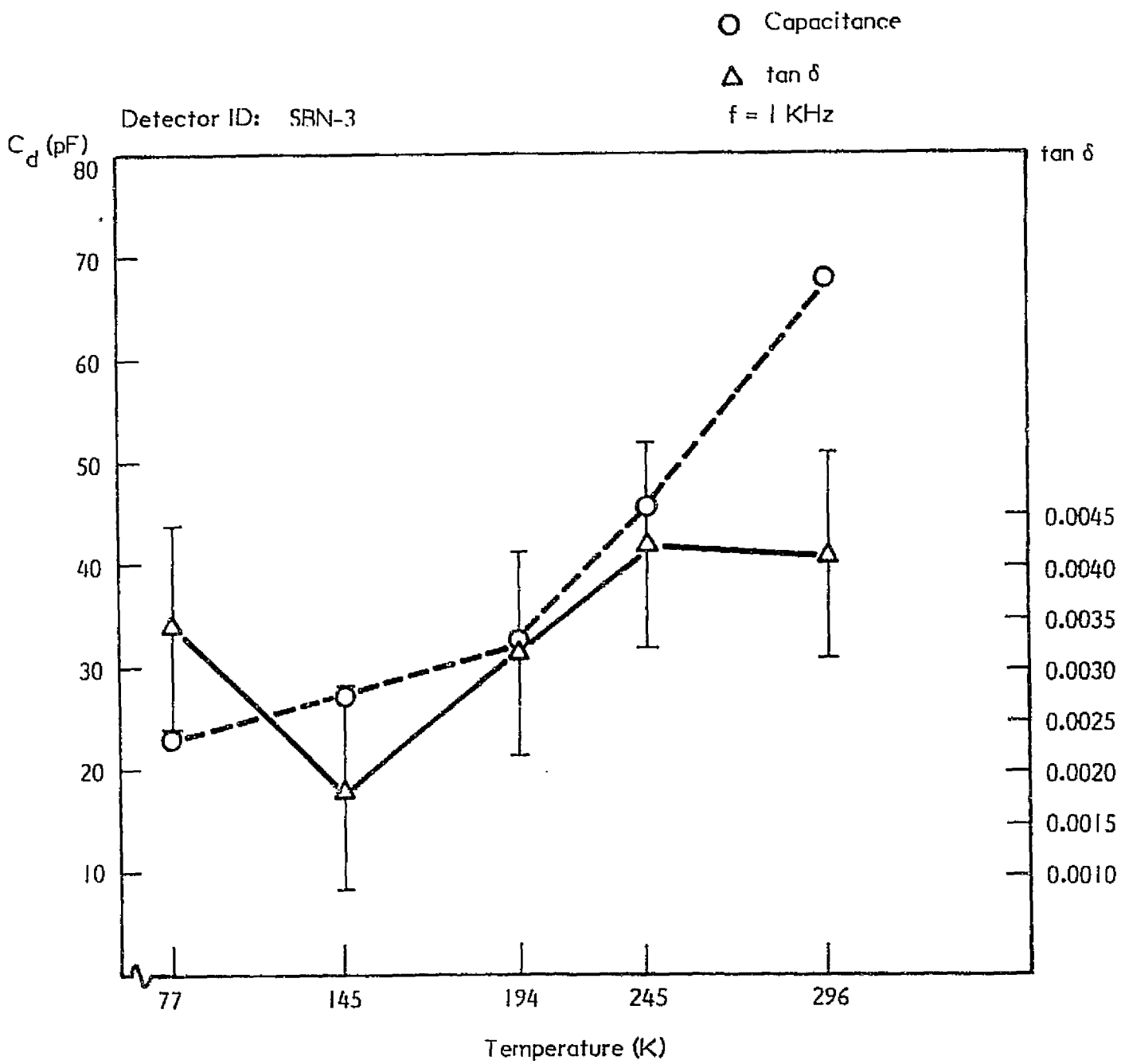

Figure 17 CAPACITANCE AND TAN δ VS TEMPERATURE FOR SBN-3, AT 1 kHz

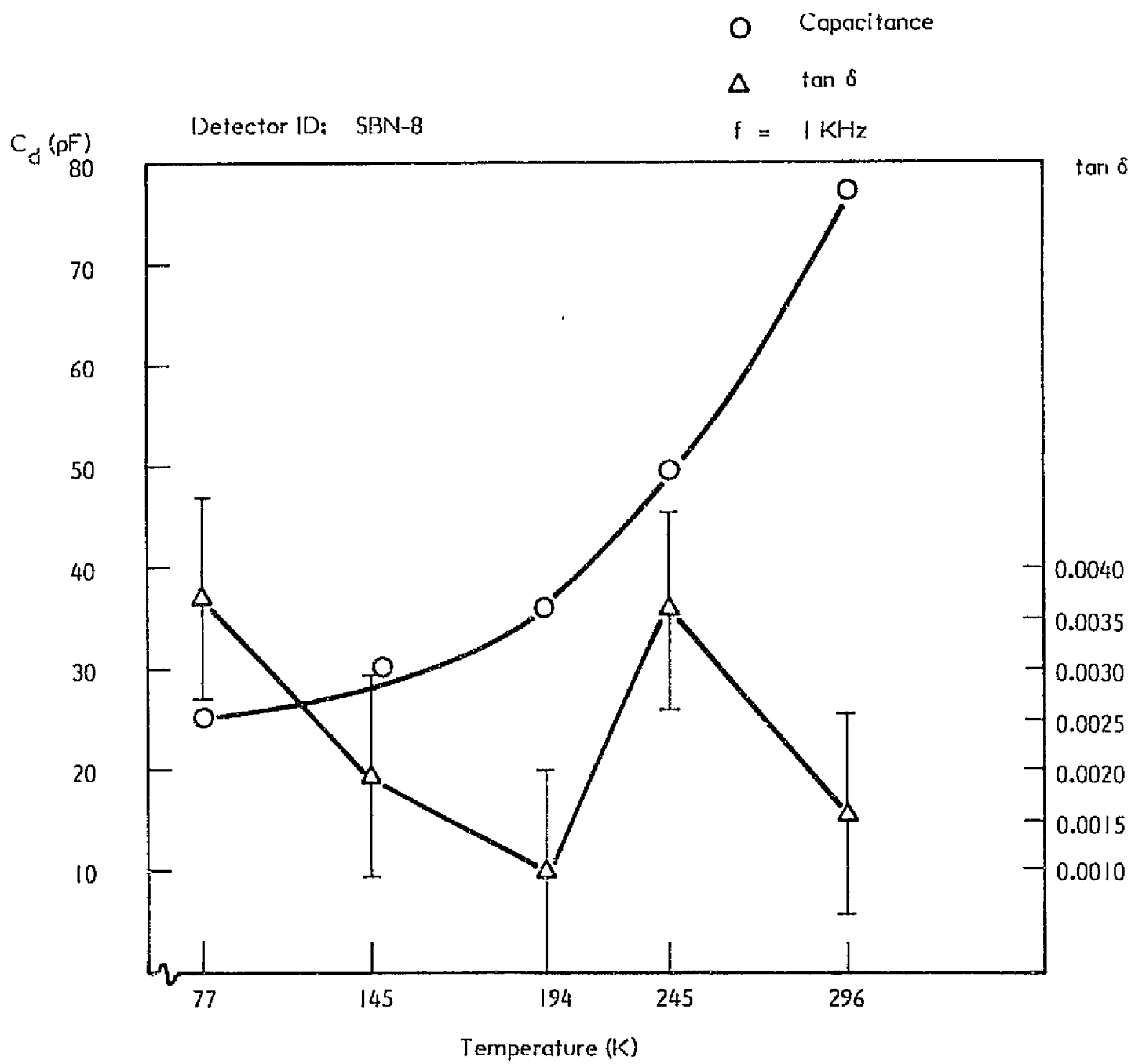

Figure 18 CAPACITANCE AND TAN δ VS TEMPERATURE FOR SBN-8, AT 1 kHz

5.0 DETECTOR READOUT CIRCUITRY

The detectors are mounted directly onto preamplifier boards containing a U423 JFET and a $1 \times 10^{11}\ \Omega$ load resistor. Those detectors which are mounted in dewars have the necessary electrical connections labeled next to the corresponding pins of the dewar. The pin configuration of the detector mounted on the TO-5 can is drawn on the following page, in addition to the basic circuit for all the detectors.

Dewar 1 has a Lake Shore Cryotronics, Inc. DT-500 FP temperature sensor mounted on the cold finger of the dewar with the detectors. Its leads are labeled next to the appropriate dewar pins. A voltage to temperature conversion chart is supplied, being valid for a 10 μ amp forward current. There is also an external lead electrically connected to the front surface of the detector, labeled "capacitance", for each detector in Dewar 1. When used in conjunction with the detector ground, the capacitance of the device can be measured.

Referring to Fig. 19, the gate of the JFET is biased at zero volt through the 10^{11} ohm load resistor across the detector. The n-channel JFET drain is biased at 5 volts positive with respect to the gate. The JFETis connected as a source-follower and its operating current is defined by the load resistor to be:

$$I_{DS} = \frac{-V_{ss} + V_s}{R_L}$$

where R_L is the source load resistor (100 KΩ). Using a relatively large V_{ss} compared to V_s, which is on the order of 1 volt makes the operating current I_{DS} nearly independent of variations in V_s from unit to unit. Also, a large R_L can be used for a large V_{ss}. Since the source-follower gain is given by:

$$G = \frac{g_m R_L}{1 + g_m R_L}$$

where g_m is the JFET transconductance, a large R_L means a near unity gain independent of JFET parameters. This gives the advantage of not having to consider the JFET gain in detector noise and responsivity measurements.

5.0 DETECTOR READOUT CIRCUITRY

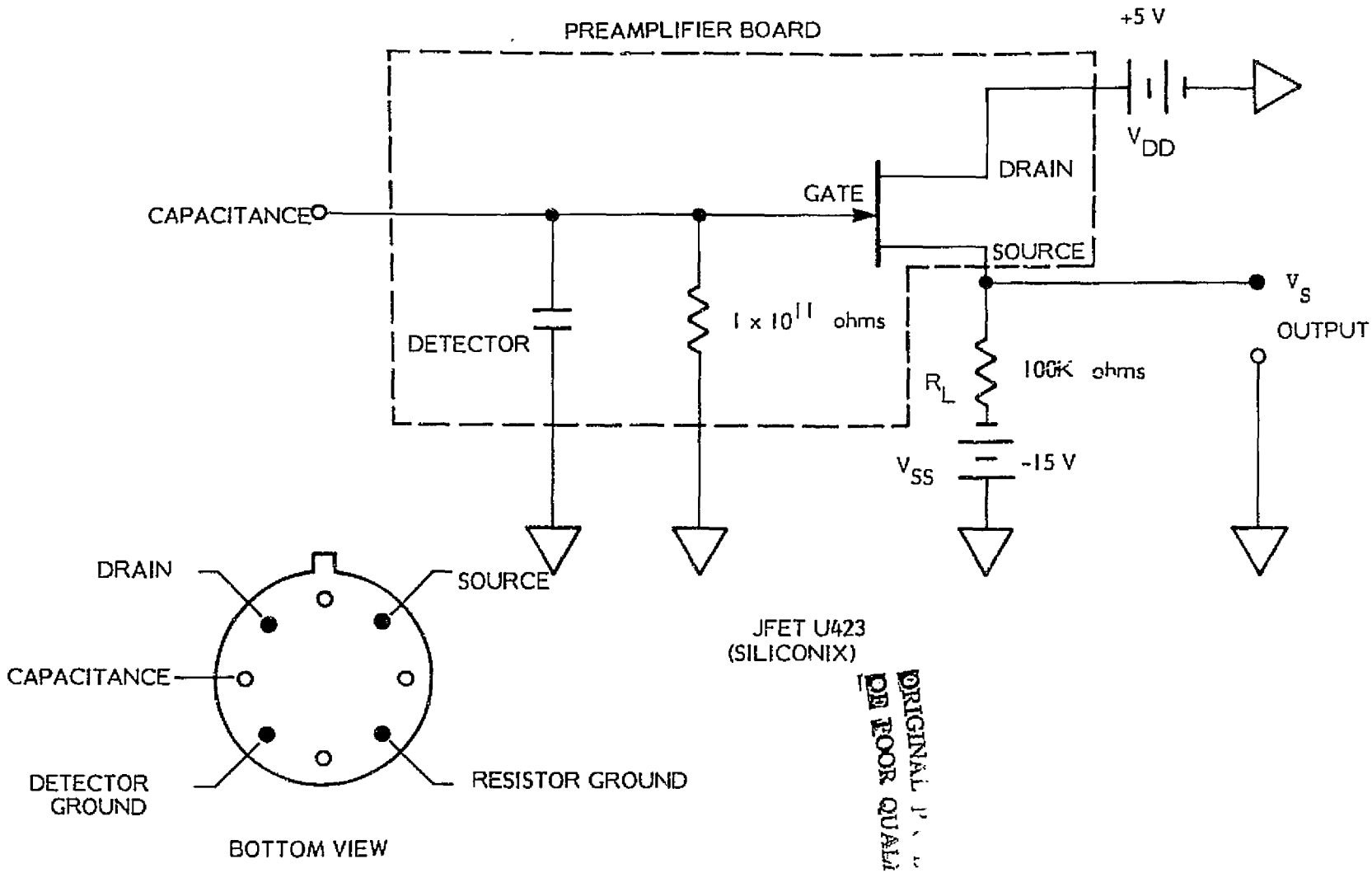

NOTE: CAPACITANCE LEAD ON DETECTORS SBN-3 AND SBN-8 ONLY.

Figure 19 JFET PREAMPLIFIER BIASING AND READOUT CONNECTIONS

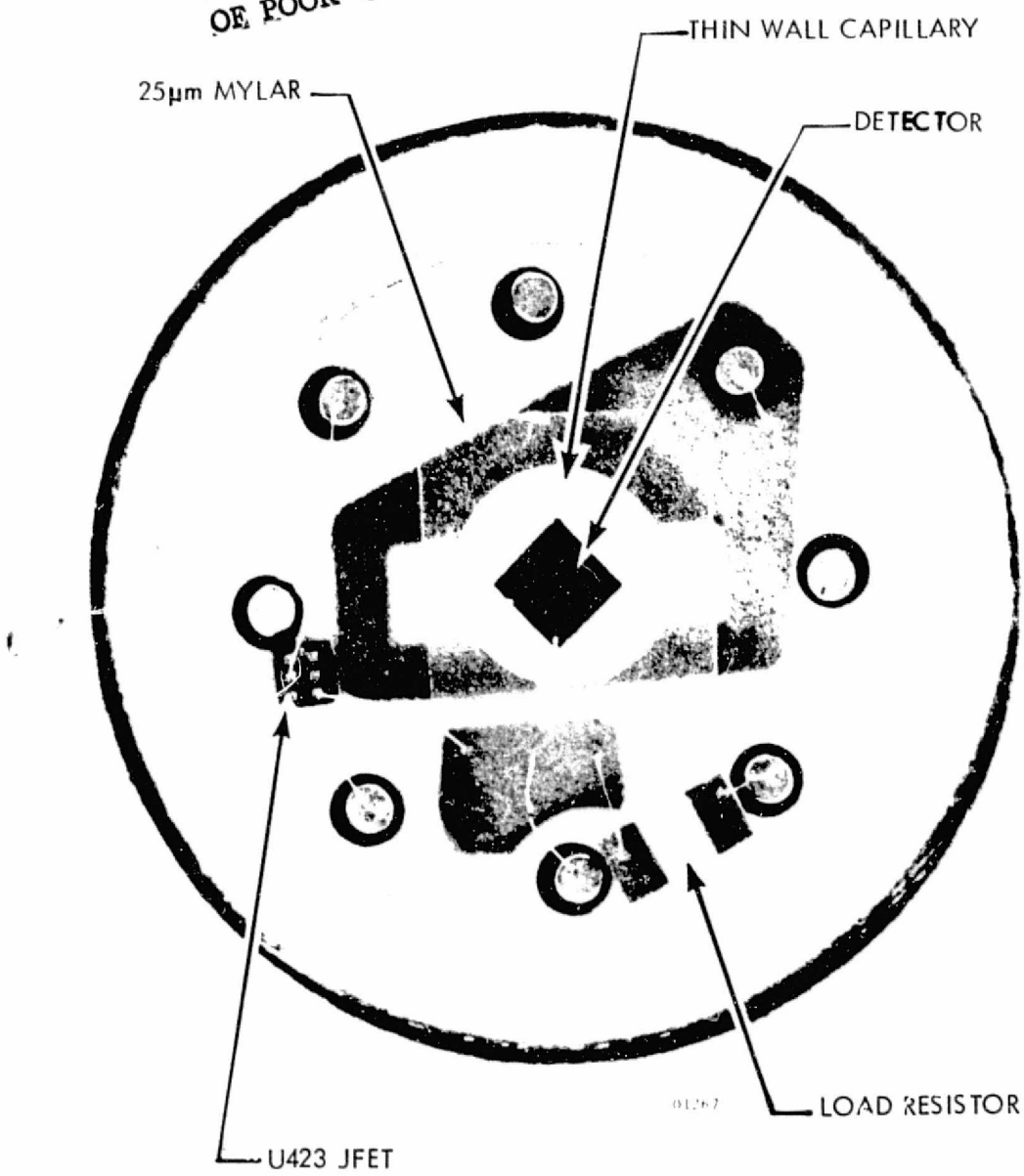

Figure 20 TOP VIEW OF A TO-5 DETECTOR PACKAGE SIMILAR TO THAT SHIPPED

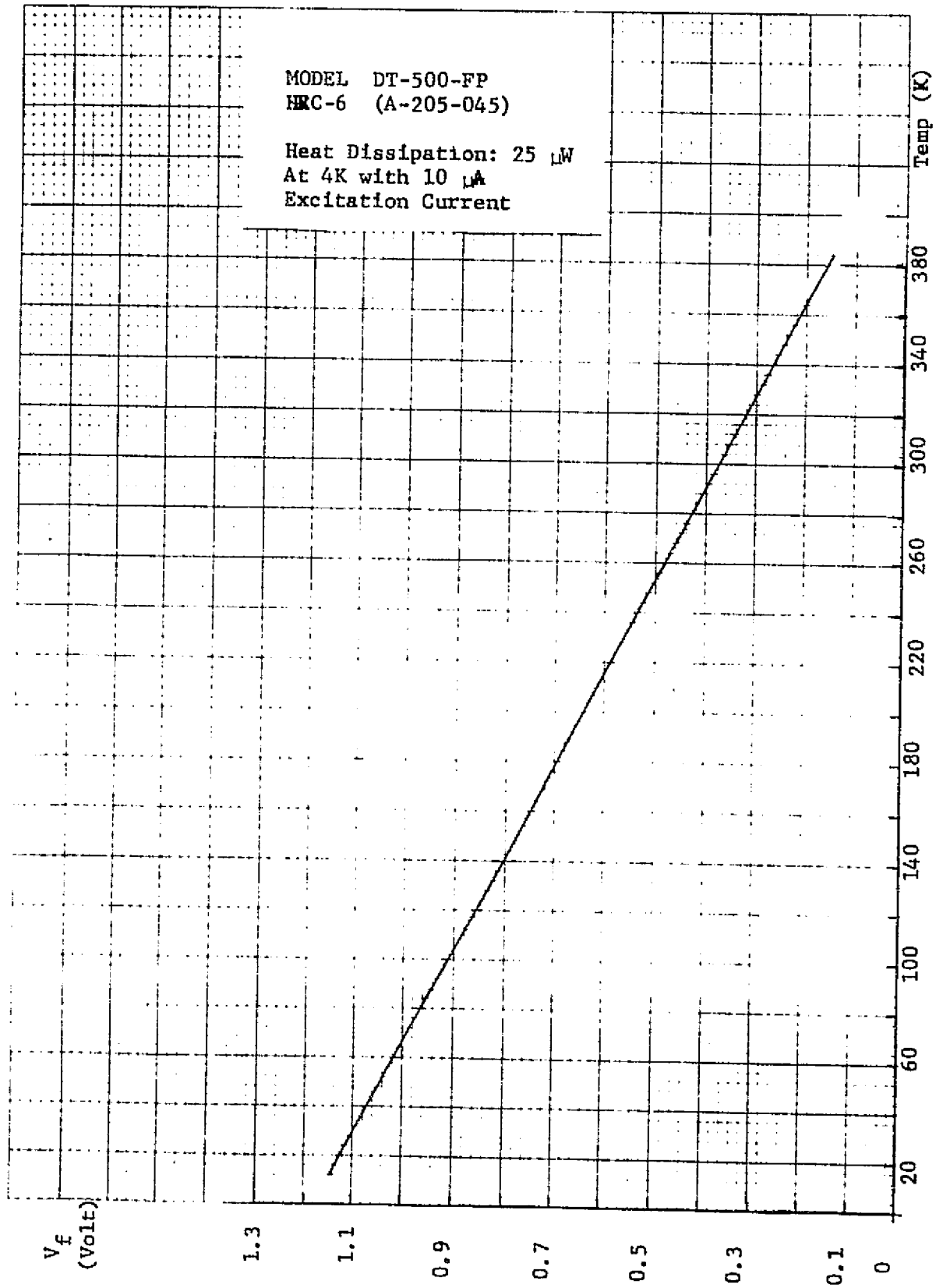

Figure 21 TEMPERATURE SENSOR DIODE

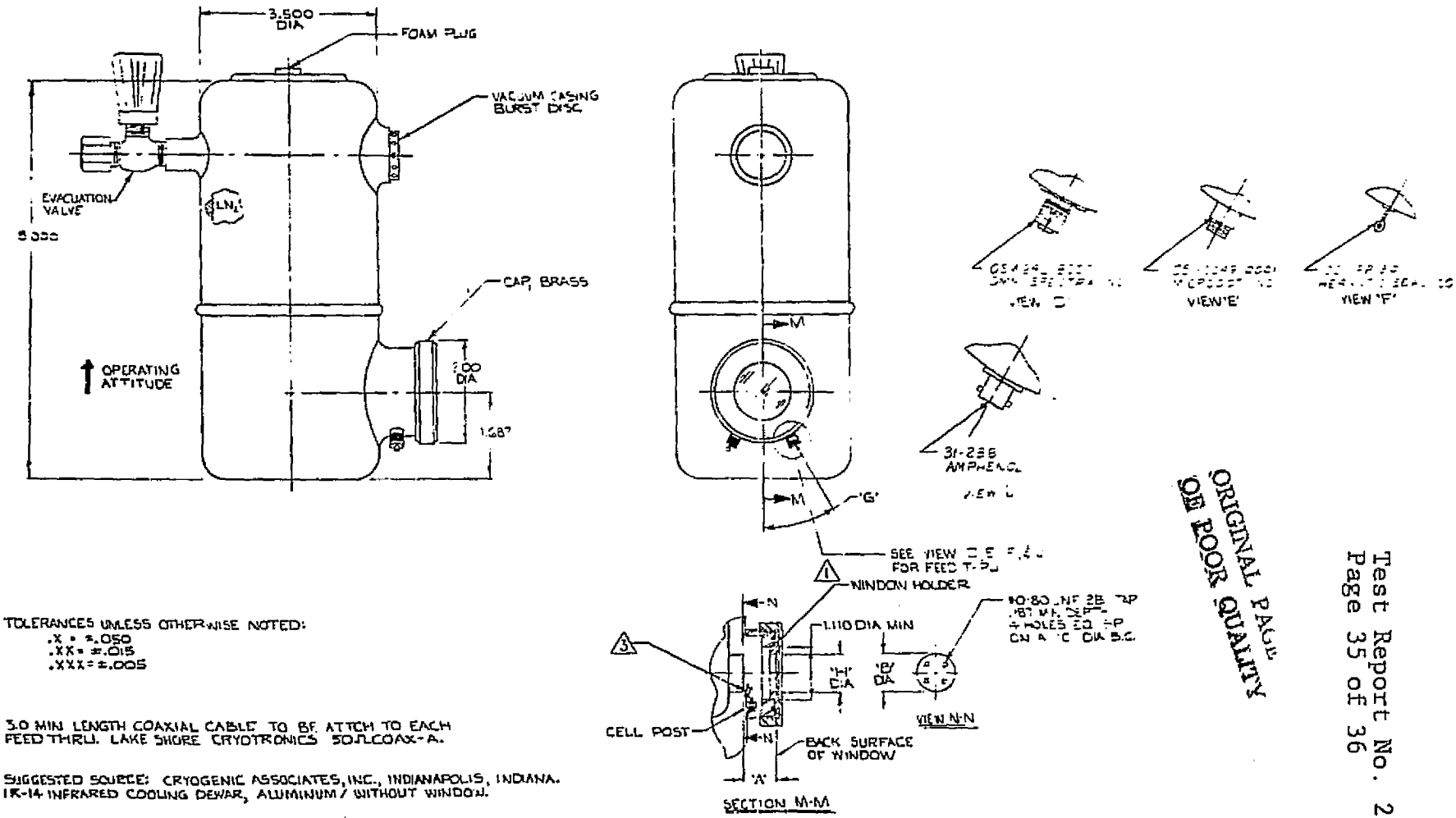

4. TOLERANCES UNLESS OTHERWISE NOTED:
.X = ±.050
.XX = ±.015
.XXX = ±.005

3 3.0 MIN LENGTH COAXIAL CABLE TO BE ATTCH TO EACH FEED THRU. LAKE SHORE CRYOTRONICS 50-1.COAX-A.

2 SUGGESTED SOURCE: CRYOGENIC ASSOCIATES, INC., INDIANAPOLIS, INDIANA. IR-14 INFRARED COOLING DEWAR, ALUMINUM / WITHOUT WINDOW.

1 WINDOW HOLDER. (SEE TABLE) TO BE VENDOR SUPPLIED.

DISTANCE FROM FRONT SURFACE OF WINDOW TO FRONT OF DETECTOR = 1.3 cm

Figure 22 DETECTOR DEWAR SPECIFICATIONS

B37

6.0 HANDLING PRECAUTIONS

Under no circumstances should the detector temperature be allowed to exceed 100°C.

Care should be taken to insure a good dewar vacuum (~1 x 10^{-6} Torr) before using cryogens to cool the detectors. This will prevent moisture condensation on the detector surfaces and the dewar window. Since the dewar holding time for LN_2 is 24 hours, it is essential that measures are taken to allow the detectors to reach room temperature before releasing the vacuum in the dewar.